High Resolution Wave Propagation Schemes for Two-Fluid Plasma Simulations

Ammar H. Hakim

A dissertation submitted in partial fulfillment of
the requirements for the degree of

Doctor of Philosophy

University of Washington

2006

Program Authorized to Offer Degree: your program here

University of Washington
Graduate School

This is to certify that I have examined this copy of a doctoral dissertation by

Ammar H. Hakim

and have found that it is complete and satisfactory in all respects,
and that any and all revisions required by the final
examining committee have been made.

Chair of the Supervisory Committee:

_____

Uri Shumlak

Reading Committee:

_____

James Riley

_____

Randal LeVeque

Date: _____

In presenting this dissertation in partial fulfillment of the requirements for the doctoral degree at the University of Washington, I agree that the Library shall make its copies freely available for inspection. I further agree that extensive copying of this dissertation is allowable only for scholarly purposes, consistent with "fair use" as prescribed in the U.S. Copyright Law. Requests for copying or reproduction of this dissertation may be referred to Proquest Information and Learning, 300 North Zeeb Road, Ann Arbor, MI 48106-1346, 1-800-521-0600, to whom the author has granted "the right to reproduce and sell (a) copies of the manuscript in microform and/or (b) printed copies of the manuscript made from microform."

Signature_____

Date_____

University of Washington

Abstract

High Resolution Wave Propagation Schemes for Two-Fluid Plasma Simulations

Ammar H. Hakim

Chair of the Supervisory Committee:
Professor Uri Shumlak
Mechanical Engineering

Algorithms for the solution of the five-moment ideal Two-Fluid equations are presented. The ideal Two-Fluid model is more general than the often used magneto-hydrodynamic (MHD) model. The model takes into account electron inertia effects, charge separation and the full electromagnetic field equations and allows for separate electron and ion motion. The algorithm presented is the high resolution wave propagation method.

The wave propagation method is based on solutions to the Riemann problem at cell interfaces. Operator splitting is used to incorporate the Lorentz and electromagnetic source terms. To preserve the divergence constraints on the electric and magnetic fields two different approaches are used. In the first approach Maxwell equations are rewritten in their mixed-potential form. In the second approach the so called perfectly-hyperbolic form of Maxwell equations are used which explicitly incorporate the divergence equations into the time stepping scheme.

The algorithms are implemented as the `WarpX` library for the solution of general hyperbolic balance laws in three-dimensions. `WarpX` is written in C++ and is scripted using Python. Parallel processing using the Message Passing Library (MPI)

is also supported. The software is tested on a one dimensional Riemann problem, ion-acoustic soliton propagation, a Weibel Instability and magnetic reconnection.

A detailed study of Lower-Hybrid Instability (LHDI) in Field-Reversed Configurations (FRCs) is performed. The strong azimuthal electron flow in the FRC causes LHDI, which can be captured if the ion-gyroradius is well resolved. The LHDI is known to be a possible source of anomalous resistivity in many plasma configurations. The study is concluded with a analysis of the LHDI in the simpler Harris current sheet configuration. It is seen that the short wavelength LHDI sets in late but then grows very rapidly, soon destroying the confinement of the plasma.

TABLE OF CONTENTS

LIST OF FIGURES

ACKNOWLEDGMENTS

I would like to thank Uri Shumlak and John Loverich for many helpful ideas and long discussion on plasma physics and related topics. My graduate school experience has been greatly enriched by working so closely with Uri and John. I like to acknowledge computer time on the Ladon Supercomputer belonging to the Mechanical Engineering (ME) Department of the University of Washington. Without this facility none of the long running simulations presented here would have been possible. Thus I am grateful to the ME department, and specially Dr. Mark Ganter for providing such a wonderful resource.

Chapter 1
TWO-FLUID MODELS

1.1 Introduction

A plasma is a gas that is significantly ionized, through heating or photo-ionization, and thus is composed of electrons, ions and neutrals. Plasmas are usually permeated by electromagnetic (EM) fields. In addition to long range smoothed or averaged EM fields there are localized short range micro-fields on individual particles. The long range fields act like body forces while the short range fields like collisions. The micro-fields are responsible for the transmission of pressure and viscous forces, for the conduction of particle energy, and for diffusion between components of the plasma[41].

The dynamical behavior of a plasma is more complex than that of a neutral fluid. This dynamical complexity has two main origins:

1. The dominant form of inter particle interaction in a plasma, electrostatic Coulomb scattering, is so weak that the mean free paths of the electrons and ions are often on the same order or even larger than the plasma's macroscopic length scales. This allows the particle's distribution function to deviate significantly from the equilibrium Maxwellian forms, and in some cases become highly anisotropic.

2. The electromagnetic fields in a plasma are of long range. This allow particles to couple to each other electromagnetically and act in concert and lead to complex collective dynamics. Much of kinetic theory of plasmas consists of study of these collective modes of interaction.

The dynamical behavior of plasmas is also strongly dependent on frequency. At the lowest frequency the motion of the electrons and ions are locked together by electrostatic forces and the plasma behaves like an electrically conducting fluid. This is the regime of magnetohydrodynamics (MHD). At somewhat higher frequencies the electrons and ions can move relative to each other, behaving like two separate, interpenetrating fluids. At still higher frequencies the distribution function of the plasma species is driven by anisotropies in the velocity space. This regime is best described by the collisionless Boltzmann equation or Vlasov equation of kinetic theory.

In this thesis numerical schemes are developed to simulate two-fluid plasma dynamics, i.e physics in the intermediate frequency regime between MHD and full kinetic theory. In the *Two-Fluid* models each plasma species is described by a set of fluid equations with electromagnetic body forces. The electromagnetic fields are modeled using Maxwell equations of electromagnetism. The fluids and EM fields are coupled through source terms: Lorentz forces acting on the fluid couple the fluid to fields and currents and charges appearing in Maxwell equations couple the fields to the fluid.

1.2 Examples of plasmas and their density-temperatures regimes

The density-temperature regime in which matter behaves as a non-relativistic plasma is shown in Fig. 1.1. In this figure the density-temperature ranges of various plasma applications are also indicated. For example, the interstellar medium and the solar wind filling up the solar system are examples of low density plasmas. In these regimes the two-fluid and kinetic effects are particularly important. Fusion devices are examples of high density-temperature plasmas. Most fusion experiments are modeled using low-frequency MHD models, although high-frequency two-fluid and kinetic effects are important to understand effects of turbulence. The dissipation provided by turbulence is commonly termed “anomalous resistivity” and is a poorly understood aspect of plasma physics. The density of the plasma in the Sun’s core is much higher and in such regimes the MHD approximation is appropriate. The “Degenerate” la-

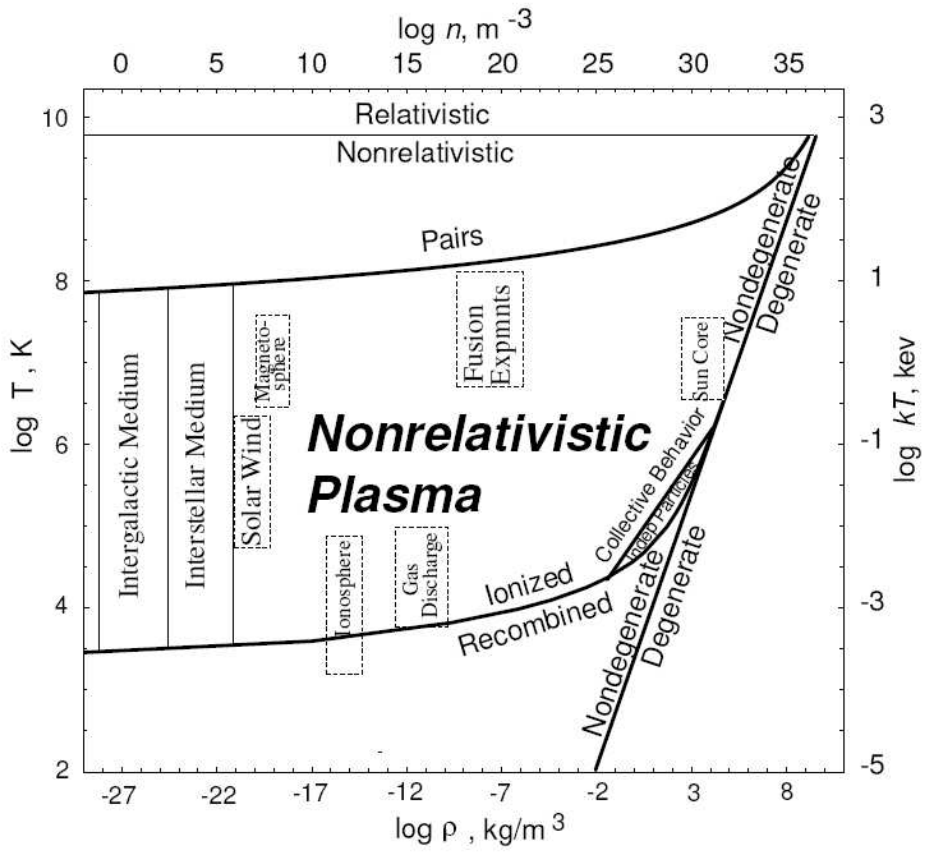

Figure 1.1: The density-temperature regime in which matter, made largely of hydrogen, behaves like a non-relativistic plasma. The boundaries of the the plasma regime are marked by thick lines. The number density of electrons, n, is plotted horizontally at the top, and the corresponding mass density ρ is plotted at the bottom. The temperature T is plotted at the left in units of degree Kelvin and at the right edge k_BT is plotted in units of electron volts, where k_B is Boltzmann's constant.

Plasma	ne (m^{-3})	T (K)	B (T)	λ_D (m)	N_D	ω_p (s^{-1})	ω_c (s^{-1})	r_L m
Gas Discharge	10^{16}	10^4	–	10^{-4}	10^4	10^{10}	–	–
Tokamak	10^{20}	10^8	10	10^{-4}	10^8	10^{12}	10^{12}	10^{-5}
Ionosphere	10^{12}	10^3	10^{-5}	10^{-3}	10^5	10^8	10^6	10^{-1}
Magnetosphere	10^7	10^7	10^{-8}	10^2	10^{10}	10^5	10^3	10^4
Solar Core	10^{32}	10^7	–	10^{-11}	1	10^{18}	–	–
Solar Wind	10^6	10^5	10^{-9}	10	10^{11}	10^5	10^2	10^4

Table 1.1: Typical density, temperature and magnetic field strength of plasmas in various environments. The various plasma parameters and their meanings are defined in the text.

bel marks the boundary at which the electrons are so tightly packed together that quantum effects become important.

Table 1.2 lists order of magnitude values of density, temperature and magnetic field strength for various plasma environments. Using these the values of some basics plasma parameters are also listed. These parameters determine the length and time scales at which physical processes occur. Some of these parameters appear naturally in the two-fluid equations as is shown in a later section. Below, some plasma parameters are listed and their importance to two-fluid physics is briefly described.

- **Plasma frequency.** The plasma frequency, ω_p, is defined by

$$\omega_p^2 = \frac{nq^2}{\epsilon_0 m} = \frac{\rho}{\epsilon_0}\left(\frac{q}{m}\right)^2. \tag{1.1}$$

  where ρ is the mass density.

- **Cyclotron Frequency.** The cyclotron frequency, ω_c, is defined by

$$\omega_c = \frac{qB}{m}. \tag{1.2}$$

- **Thermal Velocity.** The thermal velocity, v_T, is defined by

$$v_T^2 = \frac{2T}{m} = \frac{2p}{\rho}. \tag{1.3}$$

  Often the factor 2 is replaced by γ or 1.

- **Deby Length.** The Deby length, λ_D, is defined by

$$\lambda_D = \sqrt{\frac{\epsilon_0 T}{nq^2}} = \frac{v_T}{\omega_p}. \tag{1.4}$$

- **Lamor Radius.** The Lamor radius, r_L, is defined by

$$r_L = \frac{v_T}{\omega_c}. \tag{1.5}$$

- **Plasma Beta.** The plasma beta, β, is defined by

$$\beta = \frac{p}{B^2/(2\mu_0)}. \tag{1.6}$$

- **Skin Depth.** The skin-depth (inertial length), l_c, is defined by

$$l_c = c/\omega_p \tag{1.7}$$

- **Alfven Velocity.** The Alfven velocity, v_A, is defined by

$$v_A = \frac{B}{\sqrt{\mu_0 mn}}. \tag{1.8}$$

From the figure and the table it is evident that plasmas densities, temperature and magnetic fields differ by several orders of magnitudes between environments. Thus, various plasma models have been proposed to study the physics occurring in each

environment. The Two-Fluid model is applicable to those environments in which the plasma is magnetized and has skin-depths and Lamor radii comparable to the macroscopic length scales. For example, Two-Fluid effects are important in the solar wind, the Magnetosphere and certain fusion devices like the Field Reversed Configurations (FRCs). Even in regimes in which the skin depth is small Two-Fluid effects can lead to micro-instabilities which in turn cause turbulence and anomalous resistivity. Anomalous resistivity, although poorly understood, is an important factor in the design of modern fusion devices like FRCs and Spheromaks. In a later chapter micro-instabilities, like the Lower Hybrid Drift instability, a common cause of anomalous resistivity, are studied in detail. It is shown that using a low-frequency model like MHD is not appropriate for such instabilities, as these instabilities never show up in MHD models.

1.3 Vlasov-Maxwell equations and the derivation of fluid approximations

In this thesis numerical methods for low-collisional plasmas are developed. Discrete particle interactions, i.e. collisions, are neglected and collective interactions are assumed to dominate the plasma dynamics. In this case the dynamics is described using the Vlasov-Maxwell equations. These describe the temporal evolution of a particle distribution function in a six dimensional spatial and velocity space. The distribution function evolves under the influence of electromagnetic forces which are in turn determined by moments of the distribution function taken over velocity space. Each species in the plasma is described by a distribution function $f(\mathbf{x}, \mathbf{v}, t)$ defined such that $f(\mathbf{x}, \mathbf{v}, t)d\mathbf{x}d\mathbf{v}$ is the number of particles located in a phase-space volume element $d\mathbf{x}d\mathbf{v}$. As long as discrete particle interactions are negligible the distribution function evolves according to the Vlasov equation[13] which, in the non-relativistic case, may

be written as

$$\frac{\partial f}{\partial t} + v_j \frac{\partial f}{\partial x_j} + \frac{q}{m}(E_j + \epsilon_{kmj} v_k B_m)\frac{\partial f}{\partial v_j} = 0. \tag{1.9}$$

Here $\mathbf{E}$ is the electric field, $\mathbf{B}$ is the magnetic flux density, q and m are the charge and mass of the plasma species and ϵ_{kmj} is the completely anti-symmetric Cevi-Levita pseudo-tensor which is defined to be ± 1 for even/odd permutations of $(1, 2, 3)$ and zero otherwise. Summation over repeated indices is assumed. A number of auxiliary quantities are defined by taking moments of the distribution in velocity space. For use in Maxwell equations the number density $n(\mathbf{x}, t)$ and mean velocity $\mathbf{u}(\mathbf{x}, t)$ are required, and are defined by

$$n \equiv \int f d\mathbf{v} \tag{1.10}$$

$$u_j \equiv \frac{1}{n} \int v_j f d\mathbf{v}, \tag{1.11}$$

where $d\mathbf{v} = dv_1 dv_2 dv_3$ represents a volume element in velocity space. The electromagnetic fields in Eq. (1.9) are determined using Maxwell equations[17]

$$\nabla \times \mathbf{E} = -\frac{\partial \mathbf{B}}{\partial t} \tag{1.12}$$

$$\nabla \times \mathbf{B} = \mu_0 \mathbf{J} + \frac{1}{c^2}\frac{\partial \mathbf{E}}{\partial t} \tag{1.13}$$

$$\nabla \cdot \mathbf{E} = \frac{\varrho_c}{\varepsilon_0} \tag{1.14}$$

$$\nabla \cdot \mathbf{B} = 0. \tag{1.15}$$

Here μ_0 and ε_0 are the permeability and permittivity of free space, $c = (\mu_0 \varepsilon_0)^{-1/2}$ is the speed of light and, ϱ_c and $\mathbf{J}$ are the charge density and the current density defined by

$$\varrho_c \equiv \sum qn \tag{1.16}$$

$$\mathbf{J} \equiv \sum qn\mathbf{u}. \tag{1.17}$$

The summations in Eqs. (1.16) and (1.17) are over all species present in the plasma. Eqs. (1.9) to (1.17), referred to as the Vlasov-Maxwell equations, completely determine the evolution of the distribution function for each plasma species and provide a complete description of plasma dynamics.

In the high-frequency regime of kinetic theory the full Vlasov-Maxwell equation must be solved to capture the complete physics, specially collective phenomena like collisionless damping, wave-wave, wave-particle interactions and micro-turbulence. Jean's theorem, first developed in the context of stellar dynamics, shows that following individual particle orbits in a self-consistent manner is equivalent to solving the Vlasov-Maxwell equations. This is the approach taken in Particle-in-Cell (PIC) algorithms, in which particle positions and velocities are advanced using Newton's laws of motion and the electromagnetic fields are evolved self-consistently from Maxwell equations. Presently, efficient PIC codes are limited to simple geometries and small space-time scales due to the heavy demand they place on computation resources. Direct discretization of the Vlasov-Maxwell equations has also been attempted. The basic idea is to descretize the velocity space by carefully selecting a few velocity space "points", i.e. directions of particle propagation. The resulting system of equations depends only spatial coordinates and is hyperbolic and the algorithms described in the next chapter can be directly applied. This method is similar in spirit to the *discrete-ordinates* method used for neutron transport and radiative transfer applications.

For many applications, however, the full physics described by the Vlasov-Maxwell equations is not needed. Further, as the distribution function evolves in a seven dimensional space numerical solutions of the Vlasov-Maxwell equations for realistic length and time scales are not computationally feasible. To reduce the number of independent variables fluid approximations are derived by taking moments of the Vlasov equation over velocity space. Although the infinite-set of moment equations is formally equivalent to the full Vlasov equation, in practice the moment series is

terminated after just a few terms. This set of finite moment equation needs to be supplemented by *closure relations* which then completely determine the evolution of the retained moments. The selection of closure relations is difficult and usually determines what physics, specially the kinetic effects, that are captured by the reduced model. In a certain sense the closure relations are equivalent to assuming that the distribution function has certain symmetries resulting from weakly collisional effects. For example, the Two-Fluid model presented below assumes the distribution function is Maxwellian, while the *Ten-Moment* model assumes the distribution function is a Gaussian. It is also possible to use the moment-equations to develop a complete model for the Vlasov-Maxwell equation. The idea here is to write the distribution function as $f = f_0 + \delta f$, where f_0 is a symmetric equilibrium function like a Maxwellian or a Gaussian. The moment equations (Two-Fluid or Ten-Moment) can then be used to determine f_0 and a PIC code can be used to determine δf. This method, called the *Quiet-PIC* method, was first proposed by Barnes, and is more efficient (and less noisy) than the full PIC, specially if the solution is not far from equilibrium at most spatial locations.

As in classical theory of the Boltzmann equation there are a number of ways in which moments are taken of the Vlasov equation. The simplest is to multiply the Vlasov equation in turn by tensors defined by products of the velocities and integrate over the velocity space. For example, in addition to the number density and mean velocities defined by Eqs. (1.10) and (1.11) the following higher order moments are defined.

$$\mathcal{P}_{ij} \equiv m \int v_i v_j f d\mathbf{v} \tag{1.18}$$

$$\mathcal{Q}_{ijk} \equiv m \int v_i v_j v_k f d\mathbf{v} \tag{1.19}$$

$$\mathcal{K}_{ijkl} \equiv m \int v_i v_j v_k v_l f d\mathbf{v}. \tag{1.20}$$

These definition are most convenient to derive the moment equations although they

do not have a convenient physical interpretation. In classical fluid mechanics the following related, and physically more relevant, definition are used.[12].

$$P_{ij} \equiv m \int (v_i - u_i)(v_j - u_j) f d\mathbf{v} \tag{1.21}$$

$$Q_{ijk} \equiv m \int (v_i - u_i)(v_j - u_j)(v_k - u_k) f d\mathbf{v} \tag{1.22}$$

$$K_{ijkl} \equiv m \int (v_i - u_i)(v_j - u_j)(v_k - u_k)(v_l - u_l) f d\mathbf{v}. \tag{1.23}$$

The fluid equations displayed below suggest, for example, interpreting P_{ij} as a fluid stress tensor and Q_{ijk} as a heat flow tensor. As is easily shown, the moment set Eqs. (1.18)–(1.20) and Eqs. (1.21)–(1.23) are related by

$$\mathcal{P}_{ij} = P_{ij} + nmu_iu_j \tag{1.24}$$

$$\mathcal{Q}_{ijk} = Q_{ijk} + u_{[i}\mathcal{P}_{jk]} - 2nmu_iu_ju_k \tag{1.25}$$

$$\mathcal{K}_{ijkl} = K_{ijkl} + u_{[i}\mathcal{Q}_{jkl]} - u_{[i}u_j\mathcal{P}_{kl]} + 3nmu_iu_ju_ku_l. \tag{1.26}$$

In these equations square brackets around indices represent the minimal sum over permutations of free indices needed to yield completely symmetric tensors. For example $u_{[j}\mathcal{P}_{ik]} = u_j\mathcal{P}_{ik} + u_i\mathcal{P}_{kj} + u_k\mathcal{P}_{ji}$.

Multiplying the Vlasov equation in turn with 1, v_i, v_iv_j, $v_iv_jv_k$, and integrating over velocity space leads to the set of *exact* moment equations listed below

$$\frac{\partial n}{\partial t} + \frac{\partial}{\partial x_j}(nu_j) = 0 \tag{1.27}$$

$$m\frac{\partial}{\partial t}(nu_i) + \frac{\partial \mathcal{P}_{ij}}{\partial x_j} = nq(E_i + \epsilon_{ijk}u_jB_k) \tag{1.28}$$

$$\frac{\partial \mathcal{P}_{ij}}{\partial t} + \frac{\partial \mathcal{Q}_{ijk}}{\partial x_k} = nqu_{[i}E_{j]} + \frac{q}{m}\epsilon_{[ikl}\mathcal{P}_{kj]}B_l \tag{1.29}$$

$$\frac{\partial \mathcal{Q}_{ijk}}{\partial t} + \frac{\partial \mathcal{K}_{ijkl}}{\partial x_l} = \frac{q}{m}(E_{[i}\mathcal{P}_{jk]} + \epsilon_{[ilm}\mathcal{Q}_{ljk]}B_m) \tag{1.30}$$

Equations (1.41)–(1.30) are 20 equations (1+3+6+10) for 35 unknowns ($\mathcal{K}_{ijkl}$ has 15 independent components). In general any finite set of exact moment equations will always contain more unknowns than equations. To reduce the number of unknowns

and make the system determinate *closure relations* must be employed. These relations express some of the unknowns in terms of others. With appropriate closure relations the set of moment equations is termed as a *hydrodynamic* or *fluid* approximation. The accuracy of hydrodynamic approximations is limited by the accuracy of the closure relations used.

Developing closure relations is difficult. In general the closures developed are specific to certain classes of problems and hence are not applicable in all situations. For example, Chew Goldberg and Low (CGL) have developed a set of closures relations for magnetized plasmas by expanding the distribution function using the inverse magnetic field as a small parameter. This is analogous to the Chapman-Enskog expansion for neutral fluids in which the mean free path is used as a small parameter. Obviously, this approach only works when the magnetic field is large and a power-series in $1/B$ converges rapidly.

Examining the moment equations listed above it is clear that in order to make the system determinate K_{ijkl} must be expressed in terms of the other lower-order moments. One approach would be to use the CGL scheme and develop closures specific to magnetized plasmas. In this case the plasma generalization of Grad's 13-moment equations are obtained. A simpler approach is to simply set $K_{ijkl,l} = 0$, where comma represents partial derivatives. With this Eqs. (1.41)–(1.30) with Maxwell equations Eqs. (1.12) and (1.13) form a closed set of balance laws. This model is called an *ideal Two-Fluid twenty-moment model* or a *Twenty-moment* model for short. For a two species plasma (say an electron and one ion species) it has $2 \times 20 + 6 = 46$ equations.

The system of equations are simplified further if we retain only the first 10 moments and use a closure relation for Q_{ijk}. This reduced set of equations is called a *Two-Fluid ten-moment model* or a *Ten-moment* model for short. For a two species plasma it has $2 \times 10 + 6 = 26$ equations. The Ten-Moment model can properly account for the anisotropic pressure tensor effects which are important in several plasma applications. For example, it is thought that anisotropic pressure tensor effect (also

called Finite-Lamor Radius (FLR) effects in the plasma science community) can damp certain instabilities. This is particularly relevant to fusion devices like FRCs in which fluid theories that ignore the FLR effects predict the FRC to be unstable while they are found to be stable in experiments. In Appendix[I] explicit forms of the flux and sources for the Ten-Moment model are listed. Some results of solutions to Riemann problems for the Ten-Moment model are also presented.

Although the Twenty- or Ten-moment models capture more physics which may be important in certain plasma regimes, in this thesis a further simplification is made to make the computational problem more tractable. These simplification, described in the following section, reduce the number of fluid equations for each species to 5 and thus for a two species plasma form a $2 \times 5 + 6 = 16$ equation model. Throughout the rest of the thesis this reduces model is called the *ideal Two-Fluid model* or the Two-Fluid model for short.

1.4 The ideal Two-fluid model

As indicated in the previous section a closed set of Twenty- or Ten-moment equations are obtained obtained by using appropriate closure relations. Although the numerical methods developed in the next chapter can be directly applied to the Twenty- or Ten-moment model the large number of equations makes severe demands on computational resources. In this section a simpler *ideal Two-Fluid five-moment model* (or simply *ideal Two-Fluid model*) is derived in which the pressure tensor is replaced by a scalar pressure and heat conduction is neglected. For many physical systems of interest, specially in space and fusion plasma physics, this is an adequate description.

With a scalar pressure defined by $p \equiv P_{ii}/3$ the pressure tensor is written as

$$P_{ij} = p\delta_{ij} + \Pi_{ij}, \tag{1.31}$$

where Π_{ij} is a trace free stress tensor. The stress tensor Π_{ij} represents anisotropic effects (FLR effects) and in the presence of weak collisions, which have an isotropizing

effect, are very small. Setting $\Pi_{ij} = 0$ the momentum equation Eq. (1.28) reduces to

$$m\frac{\partial}{\partial t}(nu_k) + \frac{\partial}{\partial x_j}(p\delta_{jk} + mnu_k u_j) = nq(E_k + \epsilon_{ijk}u_i B_j) \tag{1.32}$$

The continuity equation Eq. (1.41) and moment equation Eq. (1.42) are 4 equations for the 5 unknowns n, u_i, p. To get an equation for the scalar pressure the pressure equation Eq. (1.29) is contracted, and the approximation $\Pi_{ij} = 0$ and $Q_{ijk,k} = 0$ are used to get

$$\frac{\partial p}{\partial t} + u_i\frac{\partial p}{\partial x_i} = \frac{5}{3}p_i\frac{\partial u_i}{\partial x_i}. \tag{1.33}$$

Another form of the equation is obtained by multiplying the Vlasov equation by $v_i v_i$ and integrating over velocity space to get

$$\frac{\partial \mathcal{E}}{\partial t} + \frac{\partial}{\partial x_j}\left(\frac{1}{2}Q_{kkj} + u_k P_{kj} + u_j\mathcal{E}\right) = qnu_j E_j. \tag{1.34}$$

where

$$\mathcal{E} \equiv \frac{1}{2}m\int v_i v_i f d\mathbf{v}. \tag{1.35}$$

Equation (1.34) indicates that $\mathcal{E}$ is has an interpretation as total energy. Using Eq. (1.35) it is easily shown that the scalar pressure and total energies are related by

$$\mathcal{E} = \frac{3}{2}p + \frac{1}{2}mnu_i u_i. \tag{1.36}$$

This equation (and Eq. (1.33)) also shows that in the Two-Fluid model each plasma species is an ideal fluid with gas-constant $\gamma = 5/3$. Assuming a scalar pressure and that heat fluxes vanish, the energy equation reduces to

$$\frac{\partial \mathcal{E}}{\partial t} + \frac{\partial}{\partial x_j}(u_j p + u_j\mathcal{E}) = qnu_j E_j. \tag{1.37}$$

The set of equations Eq. (1.41), Eq. (1.42) and Eq. (1.33) or Eq. (1.37) is the ideal Two-Fluid model and for a plasma with s species contains $5s + 6$ balance laws.

In summary, the two-fluid equations are a set of Euler equations for each species s in the plasma which, in non-conservative form, are written as

$$\frac{\partial n_s}{\partial t} + \nabla \cdot (n_s \mathbf{u}_s) = 0 \tag{1.38}$$

$$m_s n_s \left(\frac{\partial \mathbf{u}_s}{\partial t} + \mathbf{u}_s \cdot \nabla \mathbf{u}_s \right) = -\nabla p_s + q_s n_s (\mathbf{E} + \mathbf{u}_s \times \mathbf{B}) \tag{1.39}$$

$$\frac{\partial p_s}{\partial t} + \mathbf{u}_s \cdot \nabla p_s = -\gamma p_s \nabla \cdot \mathbf{u}_s. \tag{1.40}$$

The electromagnetic fields are governed by Maxwell equations of electromagnetism Equations (1.12)–(1.15). Here n_s is the number density, $\mathbf{u}_s$ is the fluid velocity, p_s is the fluid pressure, m_s is the particle mass, q_s is the particle charge, $\mathbf{E}$ is the electric field, $\mathbf{B}$ is the magnetic flux density, μ_0 and ε_0 are the permeability and permittivity of free space, $c = (\mu_0 \varepsilon_0)^{-1/2}$ is the speed of light and, ϱ_c and $\mathbf{J}$ are the charge density and the current density defined by Eqs. (1.16) and (1.17). The fluid equations can also be written in conservative form as follows

$$\frac{\partial n}{\partial t} + \frac{\partial}{\partial x_j}(n u_j) = 0 \tag{1.41}$$

$$m \frac{\partial}{\partial t}(n u_k) + \frac{\partial}{\partial x_j}(p \delta_{jk} + m n u_k u_j) = nq(E_k + \epsilon_{kij} u_i B_j) \tag{1.42}$$

$$\frac{\partial \mathcal{E}}{\partial t} + \frac{\partial}{\partial x_j}(u_j p + u_j \mathcal{E}) = q n u_j E_j. \tag{1.43}$$

In these equations the subscript s has been dropped. The total fluid energy $\mathcal{E}$ is defined by Eq. (1.36).

Numerical methods are developed for the ideal Two-Fluid model in the following chapter. These same numerical methods can also be applied to the Twenty- and Ten-moment models and further important physics captured.

1.5 Two-Fluid effects

As mentioned in the introduction the usual approach in plasma physics, specially for analytical stability studies of fusion devices, is to use single fluid theory as it is

analytically more tractable than the more accurate Two-Fluid theory. In this section plasma parameters are derived at which Two-Fluid effect as studied in this thesis become important and single-fluid theory is no longer adequate.

The momentum equation, Eq. (1.42), is written in the non-conservative form as

$$m\left(\frac{\partial \mathbf{u}}{\partial t}+\mathbf{u}\cdot\boldsymbol{\nabla}\mathbf{u}\right)=-\frac{\boldsymbol{\nabla}p}{n}+q(\mathbf{E}+\mathbf{u}\times\mathbf{B}), \tag{1.44}$$

where a scalar pressure is assumed. Introducing scalar and vector potentials, ϕ, $\mathbf{A}$, in terms of which the electric and magnetic fields are expressed as

$$\mathbf{E}=-\boldsymbol{\nabla}\phi+\partial\mathbf{A}/\partial t, \tag{1.45}$$

$$\mathbf{B}=\boldsymbol{\nabla}\times\mathbf{A}, \tag{1.46}$$

the divergence equations, Eqs. (1.14) and (1.15), are identically satisfied. Defining a *generalized momentum*, $\mathbf{P}\equiv m\mathbf{u}+q\mathbf{A}$ and a *generalized vorticity*, $\boldsymbol{\Omega}\equiv\boldsymbol{\nabla}\times\mathbf{P}=m\boldsymbol{\omega}+q\mathbf{B}$, where $\boldsymbol{\omega}=\boldsymbol{\nabla}\times\mathbf{u}$ is the fluid vorticity, Eq. (1.44) is written as

$$\frac{\partial\mathbf{P}}{\partial t}-\mathbf{u}\times\boldsymbol{\Omega}=-\frac{\boldsymbol{\nabla}p}{n}+\boldsymbol{\nabla}(mu^2/2+\phi), \tag{1.47}$$

which is a balance law for the generalized momentum[37]. The vector identity

$$\boldsymbol{\nabla}(u^2/2)=\mathbf{u}\cdot\boldsymbol{\nabla}\mathbf{u}+\mathbf{u}\times\boldsymbol{\nabla}\mathbf{u} \tag{1.48}$$

is used to derive Eq. (1.47). Taking the curl of Eq. (1.47) gives

$$\frac{\partial\boldsymbol{\Omega}}{\partial t}-\boldsymbol{\nabla}\times(\mathbf{u}\times\boldsymbol{\Omega})=-\boldsymbol{\nabla}\times(\boldsymbol{\nabla}p/n). \tag{1.49}$$

This equation applies to each species in the plasma and, for example, for a hydrogen plasma there are two such equations. Equation (1.49) can be compared to the ideal MHD result

$$\frac{\partial\mathbf{B}}{\partial t}-\boldsymbol{\nabla}\times(\mathbf{v}\times\mathbf{B})=0, \tag{1.50}$$

where $\mathbf{v}$ is the "bulk" or MHD single-fluid velocity, the Hall-MHD result[7]

$$\frac{\partial \mathbf{B}}{\partial t} - \boldsymbol{\nabla} \times (\mathbf{u}_e \times \mathbf{B}) = -\boldsymbol{\nabla} \times (\boldsymbol{\nabla} p_e / en), \tag{1.51}$$

where e is electron charge, and the Euler (neutral) fluid result

$$\frac{\partial \boldsymbol{\omega}}{\partial t} - \boldsymbol{\nabla} \times (\mathbf{v} \times \boldsymbol{\omega}) = -\boldsymbol{\nabla} \times (\boldsymbol{\nabla} p / \rho), \tag{1.52}$$

where ρ is the mass density. From these equations it is clear that the Two-Fluid theory spans the complete range from neutral fluids, to MHD to Hall-MHD: $\mathbf{B} \to \mathbf{0}$ corresponds to neutral fluid limit, $\boldsymbol{\omega} \to \mathbf{0}$ corresponds to MHD limit, while $m_e/m_i \to 0$ corresponds to Hall-MHD limit.

Examining the generalized vorticity $\boldsymbol{\Omega} = m(\boldsymbol{\omega} + q\mathbf{B}/m)$ it is clear that for Two-Fluid effects to be important

$$\omega/\omega_c \geq O(1), \tag{1.53}$$

where ω_c is the cyclotron frequency defined by Eq. (2.12). Using the fluid thermal velocity $u_T \equiv \sqrt{2p/(mn)}$ as a reference speed and some reference length L, $\omega \approx u_T/L$ and hence the condition

$$u_T/(L\omega_c) = r_L/L \geq O(1), \tag{1.54}$$

where $r_L \equiv u_T/\omega_c$ is defined as the Lamor radius, is obtained. Instead of the fluid thermal velocity if the typical speed is assumed to be the Alfven speed[1], $u_A \equiv B/\sqrt{\mu_0 mn}$, then the condition

$$u_A/(L\omega_c) = (c/\omega_p)/L \geq O(1), \tag{1.55}$$

where where ω_p is the plasma frequency defined by Eq. (2.11), is obtained.

We can thus conclude that Two-Fluid effects are important when $r_L/L \geq O(1)$ and/or when $l/L \geq O(1)$, where $l \equiv c/\omega_p$ is the skin-depth, i.e., when the Lamor

[1]This can happen when there is an equipartition between the kinetic, $mnu^2/2$, and electromagnetic energy $B^2/(2\mu_0) + \epsilon_0 E^2/2 \approx B^2/(2\mu_0)$.

radius and/or the skin depth becomes comparable to the macroscopic length scales of the plasma. In the limit $l/L \to 0$ a single-fluid MHD description is adequate and in the limit $l_e/L \to 0$, where l_e is the electron skin depth, a Hall-MHD description is adequate.

1.6 Divergence constraints in Maxwell equations

At first sight Maxwell equations, Eqs. (1.12)-(1.15), seem to be overdetermined: there are eight equations for the six field components $\mathbf{E}$ and $\mathbf{B}$. It is commonly believed that the divergence equations, Eqs. (1.14) and (1.15), are simply constraints and if initially satisfied only the curl equations are sufficient to evolve the EM fields correctly. Thus, often the divergence equations are simply ignored in numerical electromagnetics. However this is strictly true only for initial value problems, i.e. for problems on an infinite domain. As Jiang, Wu and Povinelli[18] have shown for initial-boundary value problems Maxwell equation are in fact not overdetermined and the divergence equations need to be explicitly included in the solution. Even for numerical solution to initial value problems, the evolving numerical fields may not satisfy the divergence equations and hence spurious solutions may be obtained. In this thesis two different approaches, described below, are used to take the divergence equations into account.

The first approach is to introduce a scalar potential, ϕ, and a vector potential, $\mathbf{A}$, in terms of which the EM fields are calculated as

$$\mathbf{E} = -\boldsymbol{\nabla}\phi + \partial\mathbf{A}/\partial t, \tag{1.56}$$

$$\mathbf{B} = \boldsymbol{\nabla} \times \mathbf{A}. \tag{1.57}$$

Introducing these expressions in Maxwell equations it can be shown that the potentials satisfy inhomogeneous wave equations

$$\nabla^2\phi - \frac{1}{c^2}\frac{\partial^2\phi}{\partial t^2} = \frac{\varrho_c}{\epsilon_0}, \tag{1.58}$$

$$\nabla^2\mathbf{A} - \frac{1}{c^2}\frac{\partial^2\mathbf{A}}{\partial t^2} = -\mu_0\mathbf{J}. \tag{1.59}$$

In deriving these equation the *Lorentz gauge condition*

$$\nabla \cdot \mathbf{A} = -\frac{1}{c^2}\frac{\partial \phi}{\partial t} \tag{1.60}$$

is used. Another gauge that can be used is the *Coulomb gauge*, $\nabla \cdot \mathbf{A} = 0$. With this the equation for the scalar potential reduces to a Poisson equation. The main disadvantage of the Coulomb gauge over the Lorentz gauge is that now an elliptic equation needs to be solved in addition to the hyperbolic fluid equations which is not convenient for numerical solution. The mixed potential equations are now used instead of Maxwell equations to advance the EM fields. The inhomogeneous wave equations can be rewritten as a system of first order equations. In this way a solver for second order equations is avoided. However, the disadvantage of this approach is that in three dimensions the two second order equations give 16 first order equations, thus increasing computation time. Further, the Lorentz gauge condition needs to be enforced. However, a peculiar feature of the gauge condition is that the derivatives appearing in it do not appear in the computation of the EM fields. Thus it might be simpler to apply a "gauge cleaning" procedure at each step. The simulations performed with this model show that the gauge condition usually is satisfied to within numerical precision and no such cleaning is needed.

The second approach is to modify Maxwell equations by adding two more field variables to take into account the two divergence equations. In fact, by introducing two extra variables Jiang, Wu and Povinelli[18] were able to prove that Maxwell equations are not overdetermined. However, these authors then went on to derive second order, so called "curl-curl", equations in which these extra variables do not appear. An attractive feature of adding more variables is that modified equations of hyperbolic type can be obtained, in contrast to the mixed hyperbolic/elliptic type of the original equations. These *perfectly hyperbolic Maxwell equations* (PHM) read[28,

27, 29]

$$\frac{\partial \mathbf{B}}{\partial t} + \nabla \times \mathbf{E} + \gamma \nabla \psi = 0 \tag{1.61}$$

$$\epsilon_0 \mu_0 \frac{\partial \mathbf{E}}{\partial t} - \nabla \times \mathbf{B} + \chi \nabla \phi = -\mu_0 \mathbf{J} \tag{1.62}$$

$$\frac{1}{\chi} \frac{\partial \phi}{\partial t} + \nabla \cdot \mathbf{E} = \frac{\varrho_c}{\epsilon_0} \tag{1.63}$$

$$\frac{\epsilon_0 \mu_0}{\gamma} \frac{\partial \psi}{\partial t} + \nabla \cdot \mathbf{B} = 0. \tag{1.64}$$

Here ψ and ϕ are "correction potentials" and γ and χ are error propagation speeds. As $\gamma, \chi \to \infty$ the divergence constraints are satisfied exactly. Thus more accurate solutions can be obtained with large values of these speeds, however at the expense of larger computational time. Usually $\gamma, \chi = c$ or $2c$ gives a good compromise between accuracy and speed. Thus, unlike the mixed-potential formulation the PHM formulation preserve the divergence constraints only approximately.

A number of simulations were performed to compare the mixed potential and PHM equations approaches. It was observed that both mixed-potential and PHM approaches could satisfy the divergence equations to second-order accuracy as needed by the Wave-Propagation scheme described in the next chapter. In the results presented the PHM model is used for all simulations.

Chapter 2

HIGH RESOLUTION WAVE PROPAGATION SCHEME AND IT GENERALIZATIONS

2.1 Introduction

Inhomogeneous partial differential equations with hyperbolic homogeneous parts are called *balance laws* and arise in a large number of physical applications. Balance laws are put in the generic conservation-law form

$$\frac{\partial \mathbf{q}}{\partial t} + \nabla \cdot \mathbf{f} = \mathbf{s}, \tag{2.1}$$

where $\mathbf{q}$ represents the conserved variables, $\mathbf{f}$ the fluxes and $\mathbf{s}$ the source terms. For m balance laws in d spatial dimensions $\mathbf{q}, \mathbf{s} \in \mathbb{R}^m$ and $\mathbf{f} \in \mathbb{R}^{m \times d}$. A conservation law is said to have a hyperbolic homogeneous part if for all unit vectors $\boldsymbol{\omega} \in \mathbb{R}^d$ the *flux Jacobian*, $\mathbf{A} \in \mathbb{R}^{m \times m}$, defined by

$$\mathbf{A} \equiv \frac{\partial (\mathbf{f} \cdot \boldsymbol{\omega})}{\partial \mathbf{q}} \tag{2.2}$$

has real eigenvalues and a complete set of right eigenvectors[19, 22]. If, further, the eigenvalues are all distinct the homogeneous part is called *strictly hyperbolic*. It can be shown that the Twenty- and Ten-moment models as well as the Two-Fluid models have hyperbolic homogeneous parts.

A distinctive property of hyperbolic equations is that the admit discontinuous solutions even if the initial conditions are smooth. Special methods have been developed to accurately capture such discontinuities. In this thesis the High Resolution Wave Propagation Scheme[21, 22] is used to solve the ideal Two-Fluid model.

The Wave Propagation scheme belongs to the class of *Godunov methods* which rely on the solution of Riemann problems to construct the basic numerical method.

The essential idea is as follows. The domain is discretized into cells and the solution in each cell is assumed to be represented by a polynomial. For the base scheme the polynomials are piece-wise constant in each cell. At each cell interface the solution in either cell attached to the interface will not be continuous. This discontinuity is used as an initial condition for a Riemann problem. The solution of the Riemann problem gives the conserved variables at the interface which are then used to compute interface fluxes. Once the fluxes are known the solution in each cell is updated by tallying how much flux flows into the cell. This process is described in detail in the following sections.

2.2 A class of balance laws

The plasma models discussed in the previous chapter can be all put into the balance law form Eq. (2.1). In one dimension, for example, the balance law is written as

$$\frac{\partial \mathbf{q}}{\partial t} + \frac{\partial \mathbf{f}(\mathbf{q})}{\partial x} = \mathbf{s}(\mathbf{q}). \tag{2.3}$$

In this section a particular class of such balance laws is studied and it is shown that the plasma fluid models all belong to this class.

The Two-Fluid model has a hyperbolic homogeneous part, which crudely means that disturbances propagate as waves with finite speed in the medium. Thus wave-propagation plays an important role in the physics described by hyperbolic equations. The presence of source terms, however, significantly affects the dynamics. In plasmas the source terms for the momentum equations are the Lorentz forces which act like body forces on the fluid. Further, as the sources themselves are evolving due to the changing electromagnetic (EM) field complex dynamics can occur. To classify the mathematical behavior of the balance law, the ordinary differential equation (ODE),

$$\frac{\partial \mathbf{q}}{\partial t} = \mathbf{s}(\mathbf{q}), \tag{2.4}$$

obtained by setting to zero all spatial derivative in Eq. (2.3), is considered. From the theory of ODEs the nature of the solutions to Eq. (2.4) can be determined from the

mathematical structure of the source Jacobian defined by

$$\mathbf{M} \equiv \frac{\partial \mathbf{s}(\mathbf{q})}{\partial \mathbf{q}}. \tag{2.5}$$

If the ODE is linear then the complete solution type (and the solution itself) can be determined by examining the eigensystem of $\mathbf{M}$ which is now a constant matrix. If all eigenvalues are real, the system admits decaying (growing) solutions if the eigenvalues are positive (negative). If the eigenvalues are all imaginary, the solution is a superposition of harmonics with frequencies given by the magnitude of the eigenvalues. For complex eigenvalues, the solution is a combination of decaying/growing oscillations.

The case when the eigenvalues are all real has been widely studied under the class of "relaxation systems". In such systems the decay rate can be much faster than the fastest wave speed of the homogeneous hyperbolic equation and thus the time step in any algorithm needs to be much smaller to capture the effect of the source terms properly. Examples of relaxation systems are reacting flows and large Knudsen number fluid flows in micro-mechanical machine (MEMs) devices.

The case when the eigenvalues are all imaginary has not been not widely studied, at least to the knowledge of the author. Such systems, in contrast to relaxation systems, do not have any dissipation and, on the contrary, admit dispersive solutions. This dispersion can be difficult to capture correctly in a numerical scheme as refining the grid excites waves of smaller and smaller wavelengths (i.e. of higher and higher frequencies). Further, the dispersion combined with nonlinear waves from the hyperbolic part can result in interesting nonlinear phenomena like like solitons. Examples of soliton propagation in the Two-Fluid model is shown in the next chapter.

The eigenvalues of the source Jacobian have units of inverse time. Let a typical eigenvalue be $i\omega$, where $i = \sqrt{-1}$. This eigenvalue provides a typical time scale, $T_c = 2\pi/\omega$, which represents the time period at which the solution can oscillate. Let c be a typical wave propagation speed of the homogeneous system (i.e an eigenvalue of the flux Jacobian $\partial \mathbf{f}/\partial \mathbf{q}$). If T_s is smaller than $\Delta x/c$, where Δx is the grid spacing,

the time steps needs to be much smaller than that determined from the wave speed c alone. Further, if the oscillation is to be properly resolved the time step needs to be a fraction of T_s. Thus, as in relaxation systems, the source terms can severely restrict the time-step. Unlike the relaxation system, however, where methods have been developed to overcome this restriction, smaller time steps must be used if the oscillations are not to be damped out. Further, the source term now also provides a typical length scale $L_s = c/\omega$ which must be resolved to capture the complete physics correctly.

The following model equations, Euler equation with a source, is a simple example of a nonlinear balance law with dispersive source terms.

$$\frac{\partial}{\partial t}\begin{pmatrix}\rho\\ \rho u\\ \rho v\\ \rho w\\ \mathcal{E}\end{pmatrix} + \frac{\partial}{\partial x}\begin{pmatrix}\rho u\\ \rho u^2+p\\ \rho uv\\ \rho uw\\ (\mathcal{E}+p)u\end{pmatrix} = \begin{pmatrix}0\\ \lambda\rho(vb_z - wb_y)\\ \lambda\rho(wb_x - ub_z)\\ \lambda\rho(ub_y - vb_x)\\ 0\end{pmatrix} \tag{2.6}$$

where

$$\mathcal{E} = \frac{p}{\gamma-1} + \frac{1}{2}\rho(u^2+v^2+w^2) \tag{2.7}$$

and $\mathbf{b} = \mathbf{b}(x)$ is a spatially dependent vector and λ is a constant. The source Jacobian of this system is

$$\mathbf{M} = \begin{pmatrix}0 & 0 & 0 & 0 & 0\\ 0 & 0 & \lambda b_z & -\lambda b_y & 0\\ 0 & -\lambda b_z & 0 & \lambda b_x & 0\\ 0 & \lambda b_y & -\lambda b_x & 0 & 0\\ 0 & 0 & 0 & 0 & 0\end{pmatrix} \tag{2.8}$$

and has eigenvalues $0, 0, 0, \pm i\lambda b$, where b is the magnitude of $\mathbf{b}$. This equation is a good model of the full Two-Fluid equations and shows some of the same qualitative

properties. The numerical methods developed in this chapter are applied to this equation and some results presented. Later in this chapter this model is referred to as the *dispersive Euler equations*.

2.2.1 The Two-Fluid source terms

Collecting the terms that have sources in the full Two-Fluid equation and assuming that the advection terms vanish (i.e. all spatial derivatives vanish) the following ordinary differential equation

$$\frac{d\mathbf{Q}}{dt} = \mathbf{S} \tag{2.9}$$

is obtained, where $\mathbf{Q} = [u_e, v_e, w_e, u_i, v_i, w_i, E_x, E_y, E_z]$ and

$$\mathbf{S} = \begin{bmatrix} r_e(E_x + v_e B_z - w_e B_y) \\ r_e(E_y + w_e B_x - u_e B_z) \\ r_e(E_z + u_e B_y - v_e B_x) \\ r_i(E_x + v_i B_z - w_i B_y) \\ r_i(E_y + w_i B_x - u_i B_z) \\ r_i(E_z + u_i B_y - v_i B_x) \\ -(r_e \rho_e u_e + r_i \rho_i u_i)/\epsilon_0 \\ -(r_e \rho_e v_e + r_i \rho_i v_i)/\epsilon_0 \\ -(r_e \rho_e w_e + r_i \rho_i w_i)/\epsilon_0 \end{bmatrix} \tag{2.10}$$

Here the subscripts $\alpha = \{e, i\}$ stand for electron and ion variables, $r_\alpha \equiv q_\alpha/m_\alpha$ and $u_\alpha, v_\alpha, w_\alpha$ represent the components of the velocity vector. The energy equations are not included in the analysis as energy does not appear in the source terms explicitly. Further, for the Ten-moment model the pressure equation, Eq. (1.29), is decoupled from the other equations for vanishing advection terms and can be treated separately.

From Eq. (2.9) it is clear that $\mathbf{S}$ is linear in $\mathbf{Q}$ (as there are no source terms for the density and magnetic field) and hence the solutions of Eq. (2.9) are classified by

examining the eigenvalues of the source Jacobian **J**. Using a computer algebra system like `Maple` it can be proved that the non-zero eigenvalues of **J** are all purely imaginary. Defining the plasma frequency, $\omega_{p\alpha}$, and cyclotron frequency, $\omega_{c\alpha}$, by

$$\omega_{p\alpha} = \sqrt{n_\alpha q_\alpha^2/\epsilon_0 m_\alpha}, \tag{2.11}$$

$$\omega_{c\alpha} = q_\alpha B/m_\alpha, \tag{2.12}$$

the first three eigenvalues of **J** are $0, \pm i\omega_p$, where $\omega_p^2 = \omega_{pe}^2 + \omega_{pi}^2$ and $i = \sqrt{-1}$. The other six eigenvalues are the roots of a sixth order polynomial with imaginary roots.

The above analysis shows that the source terms of the Two-Fluid model are not dissipative but describe undamped oscillations. This has some important implications for the numerical methods that can be used for the solution of the full (with advection term) system. First, low order explicit time stepping schemes cannot be used as these are unstable to the oscillation equations. Second, if the physics is to be resolved then several time steps must be taken per oscillation. Finally, in the f-wave approach of LeVeque described further on the source terms cannot be directly incorporated in the Riemann solver as the resulting scheme is unstable. As shown later the quality of the numerical solution strongly depends on the numerical scheme used to solve the ODE Eq. (2.9). In summary the Two-Fluid equations do not have any dissipative terms and can hence model only ideal effects.

2.3 High Resolution Wave Propagation Scheme

Inhomogeneous partial differential equations with hyperbolic homogeneous parts are called *balance laws* and arise in a large number of physical applications. Balance laws are put in the generic divergence form

$$\frac{\partial \mathbf{q}}{\partial t} + \nabla \cdot \mathbf{f} = \mathbf{s}, \tag{2.13}$$

where $\mathbf{q}$ represents the conserved variables, $\mathbf{f}$ the fluxes and $\mathbf{s}$ the source terms. For m balance laws in d spatial dimensions $\mathbf{q}, \mathbf{s} \in \mathbb{R}^m$ and $\mathbf{f} \in \mathbb{R}^{m \times d}$. A conservation law

is said to have a hyperbolic homogeneous part if for all unit vectors $\boldsymbol{\omega} \in \mathbb{R}^d$ the *flux Jacobian*, $\mathbf{A} \in \mathbb{R}^{m\times m}$, defined by

$$\mathbf{A} \equiv \frac{\partial(\mathbf{f}\cdot\boldsymbol{\omega})}{\partial \mathbf{q}} \tag{2.14}$$

has real eigenvalues and a complete set of right eigenvectors[22, 19]. If, further, the eigenvalues are all distinct the homogeneous part is called *strictly hyperbolic*. It can be shown that the five-moment ideal Two-Fluid equations have hyperbolic homogeneous parts. It can also be shown that higher-moment approximations to the Vlasov equations are also hyperbolic. Hence the high resolution wave-propagation method, briefly described below, can be directly applied to such equations. For a complete description of this method see LeVeque[2, 21, 22].

2.3.1 First order scheme

In two dimensions a homogeneous hyperbolic equation is written as

$$\frac{\partial \mathbf{q}}{\partial t} + \frac{\partial \mathbf{f}_1}{\partial x} + \frac{\partial \mathbf{f}_2}{\partial y} = 0, \tag{2.15}$$

where $\mathbf{f}_1$ and $\mathbf{f}_2$ are the fluxes in the X and Y direction respectively. This equation is discretized on a rectangular domain $\Omega \in [x_a, x_b]\times[y_a, y_b]$ by introducing cells $I_{ij} = [x_{i-1/2}, x_{i+1/2}]\times[y_{j-1/2}, y_{j+1/2}]$, where $x_{i-1/2}$ and $y_{j-1/2}$ are coordinates along cell edges and (x_i, y_i), where $x_i \equiv (x_{i-1/2} + x_{i+1/2})/2$ and $y_j \equiv (y_{j-1/2} + y_{j+1/2})/2$, are the coordinates of the cell center. Integrating the conservation law Eq. (2.15) over cell I_{ij} and from time t_n to t_{n+1} the update formula

$$\begin{aligned} Q_{ij}^{n+1} = Q_{ij}^n &- \frac{\Delta t}{\Delta x}\left([\mathcal{F}_1]_{i+1/2,j}^{n+1/2} - [\mathcal{F}_1]_{i-1/2,j}^{n+1/2}\right) \\ &- \frac{\Delta t}{\Delta y}\left([\mathcal{F}_2]_{i,j+1/2}^{n+1/2} - [\mathcal{F}_2]_{i,j-1/2}^{n+1/2}\right) \end{aligned} \tag{2.16}$$

is obtained. In this expression Q_{ij}^n represents the cell average

$$Q_{ij}^n \approx \frac{1}{\Delta x \Delta y}\int_{y_{j-1/2}}^{y_{j+1/2}}\int_{x_{i-1/2}}^{x_{i+1/2}} \mathbf{q}(x, y, t)\,dx\,dy, \tag{2.17}$$

$\Delta x \equiv x_{i+1/2} - x_{i-1/2}$, $\Delta y \equiv y_{j+1/2} - y_{j-1/2}$, $\Delta t \equiv t_{n+1} - t_n$ and $[\mathcal{F}_{1,2}]$ are *numerical fluxes* at the cell interfaces defined as

$$[\mathcal{F}_1]^{n+1/2}_{i-1/2,j} \approx \frac{1}{\Delta t}\int_{t_n}^{t_{n+1}} \mathbf{f}_1\big(q(x_{i-1/2}, y_j, t), x_{i-1/2}, y_j\big)dt, \tag{2.18}$$

$$[\mathcal{F}_2]^{n+1/2}_{i,j-1/2} \approx \frac{1}{\Delta t}\int_{t_n}^{t_{n+1}} \mathbf{f}_2\big(q(x_i, y_{j-1/2}, t), x_i, y_{j-1/2}\big)dt. \tag{2.19}$$

Equation (2.16) is a general update formula for finite volume schemes and several different methods can be constructed by selecting various approximations for the numerical fluxes. In this paper a specific finite volume method, the *high-resolution wave propagation method*, introduced by LeVeque is used. To introduce this method it should be first noted that at a given cell interface the value of the cell averages in the cells sharing that edge will be, in general, discontinuous. This suggest that the numerical flux at the cell edge be determined by solving a Riemann problem at that edge.

The Riemann problem is an initial value problem

$$\frac{\partial \mathbf{q}}{\partial t} + \frac{\partial \mathbf{f}_1}{\partial x} = 0, \quad x \in \mathbb{R} \tag{2.20}$$

with initial conditions $\mathbf{q}(x < 0, 0) = \mathbf{q}_l$ and $\mathbf{q}(x > 0, 0) = \mathbf{q}_r$, where $\mathbf{q}_{l,r}$ are constant vectors. For linear hyperbolic systems the Riemann problem has exact solutions. For nonlinear problems a linearization is introduced to obtain solutions valid around $x = 0$ for short times interval. Assuming that Eq. (2.20) is a linear hyperbolic equation it is written as

$$\frac{\partial \mathbf{q}}{\partial t} + \mathbf{A}_1 \frac{\partial \mathbf{q}}{\partial x} = 0, \tag{2.21}$$

where $\mathbf{A}_1$ is the flux Jacobian and is constant for the assumed linear system. Let l^p, r^p and s^p be the left eigenvectors, right eigenvectors and eigenvalues of $\mathbf{A}_1$. As the system is hyperbolic the eigenvalues must be all real and the eigenvectors are assumed to be orthonormal. Multiplying by the left eigenvector l^p a system of uncoupled wave

equations

$$\frac{\partial w^p}{\partial t} + s^p \frac{\partial w^p}{\partial x} = 0, \tag{2.22}$$

is obtained, where $w^p \equiv l^p \cdot \mathbf{q}$. This has solutions $w^p(x,t) = w_0^p(x - s^p t)$, where $w_0(x) = l^p \cdot \mathbf{q}(x,0)$. Once $w^p(x,t)$ is determined $\mathbf{q}(x,t) = \sum_p w^p r^p$ and hence the Riemann problem for linear systems (or linearized systems) is solved exactly.

In the wave propagation method the solution to the Riemann problem at each cell interface is used to derive the following approximation to the numerical fluxes

$$[\mathcal{F}_1]_{i-1/2,j} = \frac{1}{2}\big([\mathbf{f}_1]_{i,j} + [\mathbf{f}_1]_{i-1,j}\big) + \frac{1}{2}\big(\mathcal{A}_1^+ \Delta Q_{i-1/2,j} - \mathcal{A}_1^- \Delta Q_{i-1/2,j}\big). \tag{2.23}$$

Introducing this expression in the update formula along with a analogous expression for the Y direction numerical flux gives

$$\begin{aligned} Q_{ij}^{n+1} = Q_{ij}^n &- \frac{\Delta t}{\Delta x}\left[\mathcal{A}_1^+ \Delta Q_{i-1/2,j} + \mathcal{A}_1^- \Delta Q_{i+1/2,j}\right] \\ &- \frac{\Delta t}{\Delta y}\left[\mathcal{A}_2^+ \Delta Q_{i,j-1/2} + \mathcal{A}_2^- \Delta Q_{i,j+1/2}\right]. \end{aligned} \tag{2.24}$$

In these expressions the *fluctuations* $\mathcal{A}_1^{\pm}\Delta Q_{i-1/2}$ (dropping the j subscript) stand for

$$\mathcal{A}_1^- \Delta Q_{i-1/2} = \sum_{p:s_{i-1/2}^p<0} \mathcal{Z}_{i-1/2}^p + \frac{1}{2}\mathbb{Z}_{i-1/2} \tag{2.25}$$

$$\mathcal{A}_1^+ \Delta Q_{i-1/2} = \sum_{p:s_{i-1/2}^p>0} \mathcal{Z}_{i-1/2}^p + \frac{1}{2}\mathbb{Z}_{i-1/2} \tag{2.26}$$

where

$$\mathcal{Z}_{i-1/2}^p = l_{i-1/2}^p \cdot \big([\mathbf{f}_1]_i - [\mathbf{f}_1]_{i-1}\big) r_{i-1/2}^p \tag{2.27}$$

and

$$\mathbb{Z}_{i-1/2} = \sum_{p:s_{i-1/2}^p=0} \mathcal{Z}_{i-1/2}^p. \tag{2.28}$$

In deriving Eq. (2.24) the identity

$$\mathcal{A}_1^- \Delta Q_{i-1/2} + \mathcal{A}_1^+ \Delta Q_{i-1/2} = \sum_p \mathcal{Z}_{i-1/2}^p = [\mathbf{f}_1]_i - [\mathbf{f}_1]_{i-1} \tag{2.29}$$

which follows from the definition of $\mathcal{Z}_{i-1/2}^p$ (see Eq. (2.27)) is used. The eigenvectors $r_{i-1/2}^p$, $l_{i-1/2}^p$ and the eigenvalues $s_{i-1/2}^p$ needed in these expressions are computed using the flux Jacobian at the cell interfaces. For linear system this eigensystem is constant and does not depend on the solution. For nonlinear systems an appropriate averaging must be used before determining the eigensystem. In the simulations presented here *Roe averages*[34] are used for the Euler equations. Unlike conventional Godunov schemes the wave propagation method presented above can also be applied directly to situations in which the fluxes explicitly depend on spatial coordinates. Further, it is not necessary that Roe averages be used (or even exist) for the hyperbolic system being solved: simple arithmetic averages are usually sufficient. It can be shown that even when Roe averages are not available the scheme continues to be conservative[2]. Further, if Roe averages are used (or the system is linear) it can be shown that the zero wave, $\mathbb{Z}_{i-1/2}$, vanishes.

2.3.2 High resolution corrections

The scheme Eq. (2.24) is only first order accurate. To achieve second order accuracy high resolution corrections are added. These corrections are derived by taking into account second order terms in a Taylor series expansion of the conserved variables. The scheme Eq. (2.24) is modified to read

$$\begin{aligned} Q_{ij}^{n+1} = Q_{ij}^n &- \frac{\Delta t}{\Delta x}\left[\mathcal{A}_1^+ \Delta Q_{i-1/2,j} + \mathcal{A}_1^- \Delta Q_{i+1/2,j}\right] \\ &- \frac{\Delta t}{\Delta y}\left[\mathcal{A}_2^+ \Delta Q_{i,j-1/2} + \mathcal{A}_2^- \Delta Q_{i,j+1/2}\right] \\ &- \frac{\Delta t}{\Delta x}\left([\tilde{\mathcal{F}}_1]_{i+1/2,j} - [\tilde{\mathcal{F}}_1]_{i-1/2,j}\right) \\ &- \frac{\Delta t}{\Delta y}\left([\tilde{\mathcal{F}}_2]_{i,j+1/2} - [\tilde{\mathcal{F}}_2]_{i,j-1/2}\right), \end{aligned} \tag{2.30}$$

where $[\tilde{\mathcal{F}}_1]_{i-1/2}$ (dropping the j subscript) is a *correction flux* given by

$$[\tilde{\mathcal{F}}_1]_{i-1/2} = \frac{1}{2}\sum_p \text{sign}(s^p_{i-1/2})\left(1 - \frac{\Delta t}{\Delta x}|s^p_{i-1/2}|\right)\mathcal{Z}^p_{i-1/2}. \tag{2.31}$$

With this correction the high resolution wave propagation method is equivalent to the standard Lax-Wendroff method. Although the scheme Eq. (2.30) is second order accurate spurious oscillations can occur at or near discontinuities. The scheme can be limited to reduce the formal accuracy to first order at discontinuities by replacing $\mathcal{Z}^p_{i-1/2}$ Eq. (2.31) by a *limited* wave $\tilde{\mathcal{Z}}^p_{i-1/2} = \mathcal{Z}^p_{i-1/2}\phi(\theta^p_{i-1/2})$, where $\phi(\theta)$ is a suitable limiter function and

$$\theta^p_{i-1/2} \equiv \frac{\mathcal{Z}^p_{I-1/2}\cdot\mathcal{Z}^p_{i-1/2}}{\mathcal{Z}^p_{i-1/2}\cdot\mathcal{Z}^p_{i-1/2}} \tag{2.32}$$

with $I = i-1$ if $s^p_{i-1/2} > 0$ and $I = i+1$ if $s^p_{i-1/2} < 0$. For the results presented here the Monotonized Centered limiter, defined by,

$$\phi(\theta) = \max(0, \min((1+\theta)/2, 2, 2\theta)) \tag{2.33}$$

is used. With the limiters the scheme is second order accurate in smooth regions when the flow is nearly aligned along one coordinate direction. At or near discontinuities the limiters reduce the scheme to first order accuracy. To make the scheme formally second order even when the flow is not aligned along a coordinate direction *transverse corrections*, discussed below, must be added.

2.3.3 Transverse corrections

In the first order and high resolution correction schemes waves are assumed to propagate normal to the cell interface. However, in multiple dimensions, due to the additional degrees of freedom, waves may also propagate in transverse directions. To take this into account *transverse corrections* are added to the update formula. The solution of the Riemann problem at cell edge $(i-1/2, j)$ produces fluctuations traveling into cells (i, j) and $(i-1, j)$. For two dimensional problems, however, these fluctuations

should also affect the cells $(i-1, j-1)$, $(i-1, j+1)$, $(i, j+1)$ and $(i, j-1)$. To compute how these cells are affected first define left and right going fluctuations to which high resolution corrections have been added as

$$\mathcal{A}_1^{\pm}\Delta Q^*_{i-1/2} \equiv \mathcal{A}_1^{\pm}\Delta Q_{i-1/2} \mp \sum_p \text{sign}(s^p_{i-1/2}) \left(1 - \frac{\Delta t}{\Delta x}|s^p_{i-1/2}|\right) \tilde{\mathcal{Z}}^p_{i-1/2}. \tag{2.34}$$

Next, to determine how much of each fluctuation travels in the transverse direction the fluctuations are decomposed using the flux Jacobian in the other coordinate direction. For example, the left and right going ($\pm X$-direction) fluctuations are decomposed using the Y direction flux Jacobian and vice–versa, i.e.

$$\mathcal{A}_1^{\pm}\Delta Q^*_{i-1/2,j} = \mathcal{A}_2^{+}\mathcal{A}_1^{\pm}\Delta Q^*_{i-1/2,j} + \mathcal{A}_2^{-}\mathcal{A}_1^{\pm}\Delta Q^*_{i-1/2,j}. \tag{2.35}$$

Thus, for example, $\mathcal{A}_2^{+}\mathcal{A}_1^{+}\Delta Q^*_{i-1/2,j}$ indicates how much of the right going fluctuation is up going, while $\mathcal{A}_2^{-}\mathcal{A}_1^{+}\Delta Q^*_{i-1/2,j}$ indicates how much of it is down going. Note that Eq. (2.35) is analogous to Eq. (2.29) which describes the splitting of the flux jump across an interface into fluctuations. As decomposition Eq. (2.35) again requires the eigenvalues, eigenvectors and, fluctuations it can be called a transverse Riemann solution. For three-dimensional problems further Riemann problems need to be solved to determine how much of the transverse waves travel in the third direction[21].

Once the transverse Riemann problem is solved the high resolution correction flux in Eq. (2.30) is replaced by

$$[\tilde{\mathcal{F}}_2]_{i,j+1/2} = [\tilde{\mathcal{F}}_2]_{i,j+1/2} - \frac{\Delta t}{2\Delta x}\mathcal{A}_2^{+}\mathcal{A}_1^{+}\Delta Q^*_{i-1/2,j} \tag{2.36}$$

$$[\tilde{\mathcal{F}}_2]_{i,j-1/2} = [\tilde{\mathcal{F}}_2]_{i,j-1/2} - \frac{\Delta t}{2\Delta x}\mathcal{A}_2^{-}\mathcal{A}_1^{+}\Delta Q^*_{i-1/2,j} \tag{2.37}$$

$$[\tilde{\mathcal{F}}_2]_{i-1,j+1/2} = [\tilde{\mathcal{F}}_2]_{i-1,j+1/2} - \frac{\Delta t}{2\Delta x}\mathcal{A}_2^{+}\mathcal{A}_1^{-}\Delta Q^*_{i-1/2,j} \tag{2.38}$$

$$[\tilde{\mathcal{F}}_2]_{i-1,j-1/2} = [\tilde{\mathcal{F}}_2]_{i-1,j-1/2} - \frac{\Delta t}{2\Delta x}\mathcal{A}_2^{-}\mathcal{A}_1^{-}\Delta Q^*_{i-1/2,j}. \tag{2.39}$$

A similar method can be used to decompose the up and down going fluctuations into the right and left directions. The correction flux $[\tilde{\mathcal{F}}_1]_{i-1/2,j}$, for example, can then be modified in a analogous fashion as $[\tilde{\mathcal{F}}_2]_{i,j+1}$ shown above.

With the transverse terms included into the update formula the high resolution wave propagation method is formally second order in space and time for general smooth two–dimensional flow problems. It should be mentioned that even if the transverse terms are not used the scheme still gives second order accuracy. However, with the transverse terms the scheme is stable with Courant numbers up to one. Further the solution with and without the transverse terms can be significantly different in some situations. For example, in the reconnection simulation discussed in Section 3.5 if the transverse terms are not included "magnetic islands", a numerical artifact, are observed. With the transverse terms such spurious solutions do not occur.

2.4 Handling source terms

In the high resolution wave propagation method the source terms are handled in two different ways. The first is to modify Eq. (2.27) to[2]

$$\mathcal{Z}_{i-1/2} = l^p_{i-1/2} \cdot \big([\mathbf{f}_1]_i - [\mathbf{f}_1]_{i-1} - \Delta x[\mathbf{s}]_{i-1/2}\big) r^p_{i-1/2}, \tag{2.40}$$

where $[\mathbf{s}]_{i-1/2}$ is some average value of the source term calculated at the cell interface. Usually simple arithmetic averaging is sufficient. In this approach the source is directly taken into account while solving the Riemann problem. For solutions near or at equilibrium this is specially advantageous. However this method suffers from two disadvantages. The first is that for two dimensional balance laws the source must be split into two parts $\mathbf{s} = \mathbf{s}_1 + \mathbf{s}_2$ such that at equilibrium they satisfy

$$\frac{\partial \mathbf{f}_1}{\partial x} \approx \mathbf{s}_1 \tag{2.41}$$

$$\frac{\partial \mathbf{f}_2}{\partial y} \approx \mathbf{s}_2. \tag{2.42}$$

This may not be possible for all balance laws. However, for the Two–Fluid system with Maxwell equations replaced by mixed potentials such a splitting can be achieved although no such splitting exists with the PHM equations. The second disadvantage is specific to the source terms in the Two–Fluid equations. As the Two–Fluid source

terms represent undamped oscillations explicit time stepping schemes are unstable. As the wave propagation method is an explicit single step method the scheme resulting from using Eq. (2.40) is observed to be unstable.

The other approach is to use operator splitting and solve the homogeneous system separately and incorporate the source term by solving the ordinary differential equation (ODE)

$$\frac{\partial \mathbf{q}}{\partial t} = \mathbf{s}. \tag{2.43}$$

To achieve second order accuracy, and advance the complete solution by Δt, the ODE is first solved with time step $\Delta t/2$. Then the homogeneous equation is solved with time step Δt. Finally the ODE is again solved with time step $\Delta t/2$. Obviously, at each stage the results from the previous stage are used as initial conditions. This particular operator splitting scheme is known as *Strang splitting*. To solve the ODE Eq. (2.43) any standard ODE solution scheme (second order or higher) can be used. In this paper a fourth order Runge-Kutta scheme is used. Another approach is to use the trapezoidal method

$$\mathbf{q}(t+\Delta t) = \mathbf{q}(t) + \frac{1}{2}\left(\mathbf{s}(\mathbf{q}(t)) + \mathbf{s}(\mathbf{q}(t+\Delta t))\right). \tag{2.44}$$

Using a Taylor series expansion for $\mathbf{s}(\mathbf{q}(t+\Delta t))$, after some rearrangements, a semi-implicit update formula for $\mathbf{q}$ is written as

$$\mathbf{q}(t+\Delta t) = \mathbf{q}(t) + \Delta t \left(\mathbf{I} - \frac{\Delta t}{2}\frac{\partial \mathbf{s}}{\partial \mathbf{q}}\right)^{-1} \mathbf{s}(\mathbf{q}(t)). \tag{2.45}$$

Here $\partial \mathbf{s}/\partial \mathbf{q}$ is the source Jacobian and $\mathbf{I}$ is the unit matrix. Both these ODE solution methods give equally good results and all the simulations presented below use the fourth order Runge-Kutta method. This method makes it simple to add additional source terms without having to compute the source Jacobian.

2.5 The Discontinuous Galerkin Scheme

The High Resolution Wave Propagation Scheme presented in the previous section is second order in space and time. Although it is shock-capturing and can be implemented efficiently, for certain problems, like turbulent flows, it is advantageous to have a scheme which has higher spatial and/or temporal order. In this section, one such scheme the Discontinuous Galerkin (DG) Scheme, is presented which is a generalization of the Wave Propagation scheme presented above. The scheme is developed only in one-dimensions, the higher-order generalization being straightforward extension of the one-dimensional case.

2.5.1 The base scheme

In one dimension a balance law is written as

$$\frac{\partial \mathbf{q}}{\partial t} + \frac{\partial \mathbf{f}}{\partial x} = \mathbf{s}, \tag{2.46}$$

where $\mathbf{f}$ is the flux in the X direction and $\mathbf{s}$ is the source term. This equation is discretized on a domain $\Omega \in [x_a, x_b]$ by introducing cells $I_i = [x_{i-1/2}, x_{i+1/2}]$, where $x_{i-1/2}$ are coordinates along cell edge and x_i, where $x_i \equiv (x_{i-1/2} + x_{i+1/2})/2$, are the coordinates of the cell center. In the Wave-Propagation scheme the solution in each cell is assumed to be piece-wise constant. The DG scheme generalizes this concept by assuming that the solution in each cell is a piecewise-polynomial.

Let $v_r(x)$, $r = 0, 1, \ldots$ for $x \in \Omega_i = [x_{i-1/2}, x_{i+1/2}]$ be a set of polynomial "basis-functions". The basis functions are local, i.e they vanish outside the cell I_i. The set of basis functions is complete, i.e., any function $q(x)$ can be expressed as

$$q(x) = \sum_{r=0}^{\infty} q_r v_r(x), \quad x \in I_i \tag{2.47}$$

where q_r are expansion coefficients. In practice only a few terms (say 2 or 3) are

retained in the expansion. The basis functions are orthogonal, i.e.,

$$\int_{I_i} v_r(x) v_m(x) dx = \Delta x C_r \delta_{rm}, \tag{2.48}$$

where $\Delta x \equiv (x_{i+1/2} - x_{i-1/2})$ is the grid spacing, C_r are normalization constants and δ_{rm} is the Kronecker-delta symbol. Multiplying Eq. (2.47) by $v_m(x)$, integrating over I_i gives, after using the orthogonality relation Eq. (2.48),

$$q_r = \frac{1}{C_r \Delta x} \int_{I_i} q(x) v_r(x) dx, \tag{2.49}$$

using which any function can be "projected" onto the basis function.

To derive the basic DG scheme, multiply Eq. (2.46) by $v_r(x)$ and integrate over I_i to get

$$\frac{\partial}{\partial t} \int_{I_i} v_r(x) \mathbf{q} dx + \int_{I_i} v_r(x) \frac{\partial \mathbf{f}}{\partial x} dx = \int_{I_i} v_r(x) \mathbf{s}. \tag{2.50}$$

Integrate the second term by parts and expand the conserved variables in the basis functions using

$$\mathbf{q}(x,t) = \sum_{r=0}^{\infty} \mathbf{q}_r(t) v_r(x) \tag{2.51}$$

to get

$$C_r \frac{d\mathbf{q}_r}{dt} + \frac{\mathbf{f}_{i+1/2} v_r(x_{i+1/2}) - \mathbf{f}_{i-1/2} v_r(x_{i-1/2})}{\Delta x} - \frac{1}{\Delta x} \int_{I_i} \frac{dv_r(x)}{dx} \mathbf{f} dx = \frac{1}{\Delta x} \int_{I_i} v_r(x) \mathbf{s}. \tag{2.52}$$

for $r = 0, 1, \ldots$, where

$$\mathbf{f}_{i\pm1/2} \equiv \mathbf{f}(\mathbf{q}(x_{i\pm1/2}, t)) \tag{2.53}$$

are the interface fluxes at cell interface $x_{i\pm1/2}$. Equation (2.52) is the basic equation used in the DG scheme. Moving all time-independent terms to the right-hand side Eq. (2.52) is written as

$$\frac{d\mathbf{q}_r}{dt} = \mathcal{L}_r(\mathbf{q}) \tag{2.54}$$

for $r = 0, 1, \ldots$, where $\mathcal{L}_r(\mathbf{q})$ is

$$\mathcal{L}_r(\mathbf{q}) = -\frac{\mathbf{f}_{i+1/2} v_r(x_{i+1/2}) - \mathbf{f}_{i-1/2} v_r(x_{i-1/2})}{\Delta x} + \frac{1}{\Delta x}\int_{I_i} \frac{dv_r(x)}{dx}\mathbf{f}dx + \frac{1}{\Delta x}\int_{I_i} v_r(x)\mathbf{s}. \tag{2.55}$$

Once $\mathcal{L}_r(\mathbf{q})$ is computed Eq. (2.54) is a ODE for the expansion coefficients which can be solved using any standard ODE solver like a third– or fourth–order Runge-Kutta method. With Runge-Kutta time stepping the DG method is called a *Runge-Kutta Discontinuous Galerkin* (RKDG) scheme.

To compute the interface flux the same method (see Eq. (2.23), and Eqs. (2.25)–(2.26)) as used in the Wave-Propagation method is used.

2.5.2 Selection of basis functions. Numerical quadrature

A convenient choice of basis functions is provided by the Legendre polynomials $P_n(x)$, in terms of which

$$v_r(x) = P_r(\eta(x)), \tag{2.56}$$

where

$$\eta(x) \equiv \frac{x - x_i}{\Delta x/2} \tag{2.57}$$

maps the interval I_i to the interval $[-1, 1]$ over which the Legendre polynomials are defined. Using the orthogonality property of the Legendre polynomials

$$\int_{-1}^{1} P_n(x) P_m(x) dx = \frac{2}{2m+1}, \tag{2.58}$$

the coefficients C_r are found to be simply $C_r = 1/(2r+1)$. Further, the value of the basis functions at cell interfaces is

$$v_r(x_{i\pm1/2}) = P_r(\pm 1) = (\pm 1)^r. \tag{2.59}$$

To numerically evaluate the integrals appearing in Eq. (2.55) Gaussian quadrature is used. Thus, any function $q(x)$ integrated over I_i is evaluated using

$$\int_{I_i} q(x)dx = \frac{1}{2}\int_{-1}^{1} q(x(\eta))d\eta = \frac{1}{2}\sum_j w_j \bar{q}(\eta_j), \tag{2.60}$$

where $x(\eta) = \eta\Delta x/2 + x_i$, $\bar{q}(\eta) \equiv q(x(\eta))$ and w_j and η_j are weights and abscissa of a suitably selected Gaussian quadrature scheme. In general, if the expansion Eq. (2.51) is truncated after R terms, a Gaussian quadrature of order R needs to be used.

Introducing the Legendre polynomial basis functions in Eq. (2.55) $\mathcal{L}_r$ is written as

$$\mathcal{L}_r(\mathbf{q}) = -\frac{\mathbf{f}_{i+1/2} - (-1)^r \mathbf{f}_{i-1/2}}{\Delta x} + \frac{1}{\Delta x}\int_{-1}^{1} \frac{dP_r(\eta)}{d\eta}\bar{\mathbf{f}}d\eta + \frac{1}{2}\int_{-1}^{1} P_r \bar{\mathbf{s}}d\eta, \tag{2.61}$$

where $\bar{\mathbf{f}}(\eta) \equiv \mathbf{f}(q(x(\eta),t))$ and $\bar{\mathbf{s}}(\eta) \equiv \mathbf{s}(q(x(\eta),t))$. With interface fluxes computed using the Wave-Propagation scheme and the integrals computed using Gaussian quadrature, the DG is completely specified.

2.5.3 Limiters for the Discontinuous Galerkin Scheme

Just as in the Wave Propagation scheme limiters need to be applied to the DG scheme to avoid spurious oscillations near discontinuities and for stabilization of non-linear systems. Unlike the Wave Propagation scheme limiters for the DG scheme typically are applied directly to the conserved variables rather than the waves computed from the solution to the Riemann problem. The conserved variables can be limited in terms of characteristics. Let $\mathbf{q}_r^i$ be the expansion coefficients of the conserved variables in cell i. Let $a^p \equiv l^p \mathbf{q}_1^i$, $a_+^p \equiv l^p(\mathbf{q}_0^{i+1} - \mathbf{q}_0^i)$ and $a_-^p \equiv l^p(\mathbf{q}_0^i - \mathbf{q}_0^{i-1})$. Then the limiter modifies the coefficient of the linear term as follows

$$\mathbf{q}_1^i = \sum_p r^p \,\mathrm{mm}(a^p, a_+^p, a_-^p). \tag{2.62}$$

In these equations r^p, l^p are the right and left eigenvectors of the flux Jacobian computed from cell averages and $\mathrm{mm}(a,b,c)$ is a modified min-mod function defined

as

$$\mathrm{mm}(a,b,c) = a \quad \text{if } |a| < M(\Delta x)^2 \tag{2.63}$$

$$= \mathrm{m}(a,b,c), \tag{2.64}$$

where M is some constant and $\mathrm{m}(a,b,c)$ is defined by

$$\mathrm{m}(a,b,c) = \max(a,b,c) \quad \text{if} sgn(a) = sgn(b) = sgn(c) = + \tag{2.65}$$

$$= \min(a,b,c) \quad \text{if} sgn(a) = sgn(b) = sgn(c) = - \tag{2.66}$$

$$= 0 \quad \text{otherwise.} \tag{2.67}$$

The higher-order coefficient ($r > 2$) are set to zero if the $r = 1$ coefficient is modified by the limiting process.

Another simpler method is to apply the limiters component-wise without doing any eigen-decomposition of the flux Jacobian. This is equivalent to using unit vectors for the right and left eigenvectors (for example $r^2 = [0, 1, 0, \ldots]^T$) in the above equations. The constant M is problem specific and for all simulations shown below is set to 0.

2.5.4 Time stepping scheme

To advance the solution in time, i.e., solve the ODE Eq. (2.54), Runge-Kutta time stepping is used. For 3rd order temporal accuracy the following scheme is used.

$$\mathbf{q}^1 = \mathbf{q}^n + \Delta t \mathcal{L}(\mathbf{q}^n) \tag{2.68}$$

$$\mathbf{q}^2 = \frac{3}{4}\mathbf{q}^n + \frac{1}{4}\left(\mathbf{q}^1 + \Delta t \mathcal{L}(\mathbf{q}^1)\right) \tag{2.69}$$

$$\mathbf{q}^{n+1} = \frac{1}{3}\mathbf{q}^n + \frac{2}{3}\left(\mathbf{q}^2 + \Delta t \mathcal{L}(\mathbf{q}^2)\right) \tag{2.70}$$

In these equations $\mathbf{q}^n$ is the solution at time t and $\mathbf{q}^{n+1}$ at time $t + \Delta t$. Other higher order schemes like the standard fourth-order Runge-Kutta scheme can be used. In general, for a kth order spatial scheme the time-scheme should be at least of order k. The CFL number for a spatial scheme of order k is $1/(2k-1)$.

2.6 Benchmarking applications

In this section the Wave Propagation scheme and the DG scheme are applied to the dispersive Euler equations, Eq. (2.6). This system shows some of the same qualitative behavior as the full Two-Fluid equations and thus is a good model problem. Two problems are studied below. The first is a linear acoustics problem which shows strong dispersion due to the source terms. For this linear problem an exact solution can be computed and shows very small scale features. The higher-order accuracy of the DG scheme is advantageous to capture these features. The second problem is the standard Sod shock-tube problem now applied to the dispersive Euler equation. Again, the source term modifies the solution, but in this case, due to the presence of the discontinuities, both the schemes give similar accuracy for the same grid resolution. However, the Wave Propagation scheme runs about 5 times faster, making it a better choice for problems with discontinuities or strong non-linearities.

2.6.1 Propagation of an acoustic pulse

In the linear regime the dispersive Euler equations support sound waves, however the dispersion relation of these wave is modified due to the presence of the source terms. To derive the modified dispersion relation Eq. (2.6) is written in non-conservative form as

$$\frac{\partial \rho}{\partial t} + \rho \frac{\partial u}{\partial x} + u \frac{\partial \rho}{\partial x} = 0 \tag{2.71}$$

$$\rho \left(\frac{\partial u}{\partial t} + u \frac{\partial u}{\partial x} \right) = -\frac{\partial p}{\partial x} + \rho \lambda v b_z \tag{2.72}$$

$$\rho \left(\frac{\partial v}{\partial t} + u \frac{\partial v}{\partial x} \right) = -\rho \lambda u b_z \tag{2.73}$$

$$\frac{\partial p}{\partial t} + u \frac{\partial p}{\partial x} = -\gamma p \frac{\partial u}{\partial x}, \tag{2.74}$$

where, for simplicity, $b_x = b_y = 0$. Linearizing these equations about a constant state $\rho = \rho_0$, $p = p_0$, $u = v = 0$[1] the following linear system is obtained.

$$\frac{\partial \rho_1}{\partial t} = -\rho_0 \frac{\partial u_1}{\partial x} \tag{2.75}$$

$$\rho_0 \frac{\partial u_1}{\partial t} = -\frac{\partial p_1}{\partial x} + \rho_0 \lambda v_1 b_z \tag{2.76}$$

$$\rho_0 \frac{\partial v_1}{\partial t} = -\rho_0 \lambda u_1 b_z \tag{2.77}$$

$$\frac{\partial p_1}{\partial t} = -\gamma p_0 \frac{\partial u_1}{\partial x}, \tag{2.78}$$

where the variables with subscript 1 are perturbations of the constant initial state, and all products of perturbations are neglected. As the equations are linear a solution of the form

$$f(x,t) = \sum_{n=0}^{\infty} f_n e^{i(k_n x + w_n t)} \tag{2.79}$$

for $f \in \{\rho_1, u_1, v_1, p_1\}$, and where k_n is the wave number and ω_n is frequency, is assumed. Substituting in Eqs. (2.75)–(2.78) the following algebraic equations for each Fourier component of the variables are obtained.

$$i\omega_n \rho_1 = -ik_n u_1 \rho_0 \tag{2.80}$$

$$i\omega_n u_1 \rho_0 = -ik_n p_1 + \lambda v_1 b_z \tag{2.81}$$

$$i\omega_n v_1 \rho_0 = -\rho_0 \lambda u_1 b_z \tag{2.82}$$

$$i\omega_n p_1 = i\gamma p_0 k_n u_1. \tag{2.83}$$

For this the dispersion relation

$$\omega_n = \pm \left(k_n^2 c_{s0}^2 + \omega_c^2\right)^{1/2} \tag{2.84}$$

is obtained. Here $c_{s0} \equiv \sqrt{\gamma p_0/\rho_o}$ is the speed of sound and $\omega_c \equiv \lambda b_z$ is the eigenvalue of the source Jacobian. Equation (2.84) shows that the source Jacobian eigenvalue

[1]For the equation system of the type Eq. (2.3) the initial conditions must lie in the null space of the source Jacobian if solid body motion is to be avoided. Thus, examining Eq. (2.8) it is clear that u and v must identically vanish.

modifies the linear dispersion relation of the Euler equations ($\omega_p = \pm k_n c_{s0}$) to a quadratic one. For small ω_c the dispersion is still linear, but for large ω_c the propagating sound wave can undergo significant dispersion as shown below.

To test the numerical algorithms simulations were initialized with uniform ρ_0 and p_0 and a velocity perturbation given by $u_1(x,0)$ where

$$u_1(x,t) = U_0 \sum_{n=0}^{N} \frac{i}{2n+1} e^{ik_n x} e^{i\omega_n t} \tag{2.85}$$

with $k_n = 2\pi(2n+1)$. For $N \to \infty$ this represents a the propagation of a step function perturbation. Letting $u_i^{(n)} \equiv iU_0/(2n+1)e^{i(k_n x+\omega_n t)}$ the Fourier components of the other flow variable perturbations are given by (see Eqs. (2.80)–(2.83))

$$\rho_1^{(n)} = -\frac{k_n \rho_0}{\omega_n} u_1^{(n)} \tag{2.86}$$

$$v_1^{(n)} = -i\frac{\lambda b_z}{\omega_n} u_1^{(n)} \tag{2.87}$$

$$p_1^{(n)} = -\frac{\gamma k_n p_0}{\omega_n} u_1^{(n)}, \tag{2.88}$$

summing which over $n = 0, \ldots, N$ gives the exact solution to the linear problem.

Figure (2.1) shows the exact solution at $t = 1000$ on $x \in [0,1]$ and for $N = 5000$, $c_s = \sqrt{2}$ and $\omega_c = 10$. It is clear that the exact solution has many fine scale features due to the strong dispersion from the source terms. It is also evident that unless very fine grid are used these features can not be resolved as all waves less than the grid spacing get diffused away due to numerical dissipation. This figure also shows a feature peculiar to the dispersive system Eq. (2.3), i.e., what appears as dispersion due to the numerical scheme used is actually due to the mathematical nature of the equation system itself.

To test the numerical methods and to not have to resolve all the frequencies in the exact solution of a square pulse, only $N = 9$ Fourier modes were retained. Further, $\rho_0 = p_0 = 1$, $\gamma = 2$, $\lambda = 10$ and $b_z = 1$ were selected. With this choice $c_s = \sqrt{2}$ and $\omega_c = 10$. The Wave Propagation scheme and the 2nd and 3rd order

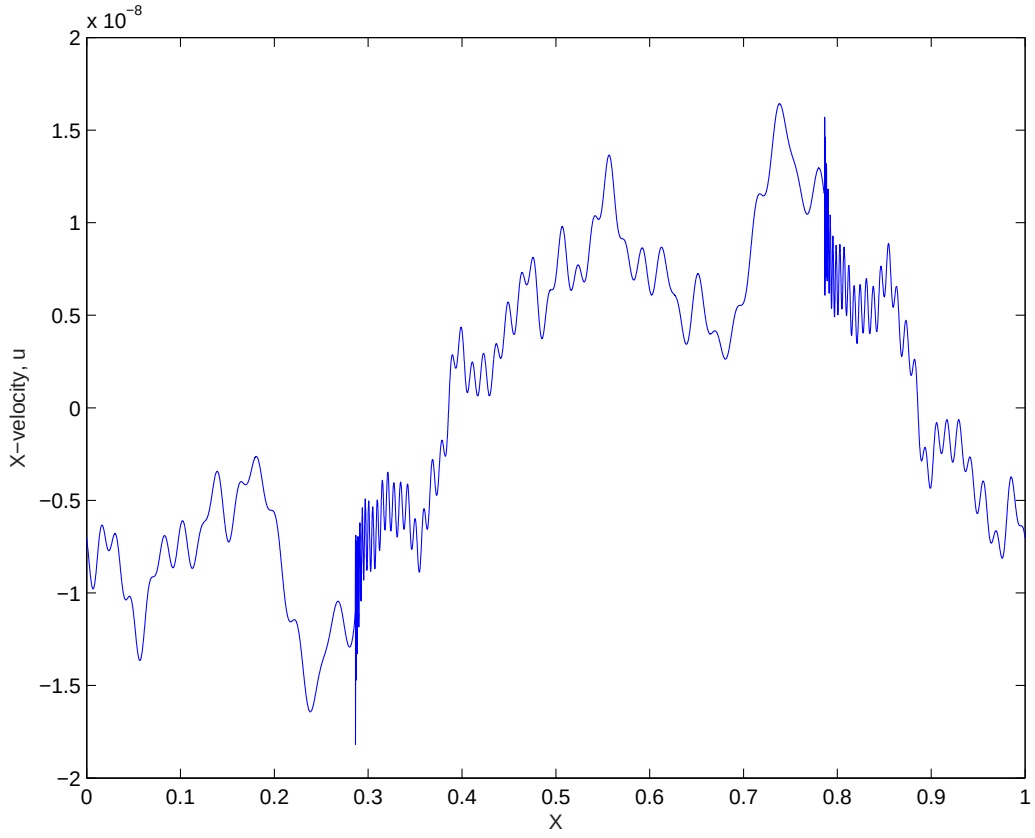

Figure 2.1: Exact solution of the linear dispersive Euler equation at $t = 1000$ with $c_s = \sqrt{2}$, $\omega_c = 10$ and $N = 5000$. Fine scale features due to the dispersive source terms are observed. These features can be difficult to capture using a numerical scheme and may be mistaken for numerical "noise" or numerical dispersion.

spatial and 3rd order temporal RKDG schemes were used to solve the dispersive Euler system. The 2nd and 3rd RKDG order schemes were run at CFL number of 1/3 and 1/5 respectively and the Wave-Propagation scheme was run at a CFL of 1. To ensure that the simulation remained in the linear regime in Eq. (2.85) U_0 was set to 10^{-8}. All other variable were initialized by the exact solutions at $t = 0$ given by the sum of their constant background values and their perturbed values computed from Eqs. (2.86)–(2.86). The simulations were run to $t = 3$ and the results compared.

Figure (2.2) show the solutions computed using the DG 2nd and 3rd order schemes on 40 cells. From this figure it is evident that the 2nd order scheme has difficulty resolving the smaller wavelength features, but the 3rd order scheme captures these features better. Figure (2.3) shows the results on 40 cells with the Wave Propagation scheme. From this figure it appears that the Wave Propagation scheme resolves the features as well as the 3rd order RKDG does. This is not surprising as for CFL of 1 the Wave Propagation scheme shows very little numerical dissipation and dispersion and hence is able to capture the solution better.

Figure (2.4) shows the solution computed using the DG method on 80 cells. It is clear that the 3rd order method has captured the solution very well while the 2nd order solution still under-resolves the small wavelengths. Figure (2.5) shows the results on 80 cells with the Wave Propagation scheme. As expected the Wave Propagation scheme also captures all the flow features as well as the 3rd order DG scheme for this particular problem.

Figure (2.6) shows the solution computed using the DG method on 160 cells. For this grid resolution the 2nd order solution matches the exact solution very well while the 3rd order solution is indistinguishable from the exact solution.

From this set of simulations it would seem that the Wave Propagation method is superior to the DG 2nd and 3rd order method. However, although these results are correct for this simulation this conclusion is not always true. When the above simulations are run with $\omega_c = 100$ the Wave Propagation scheme performs poorly when

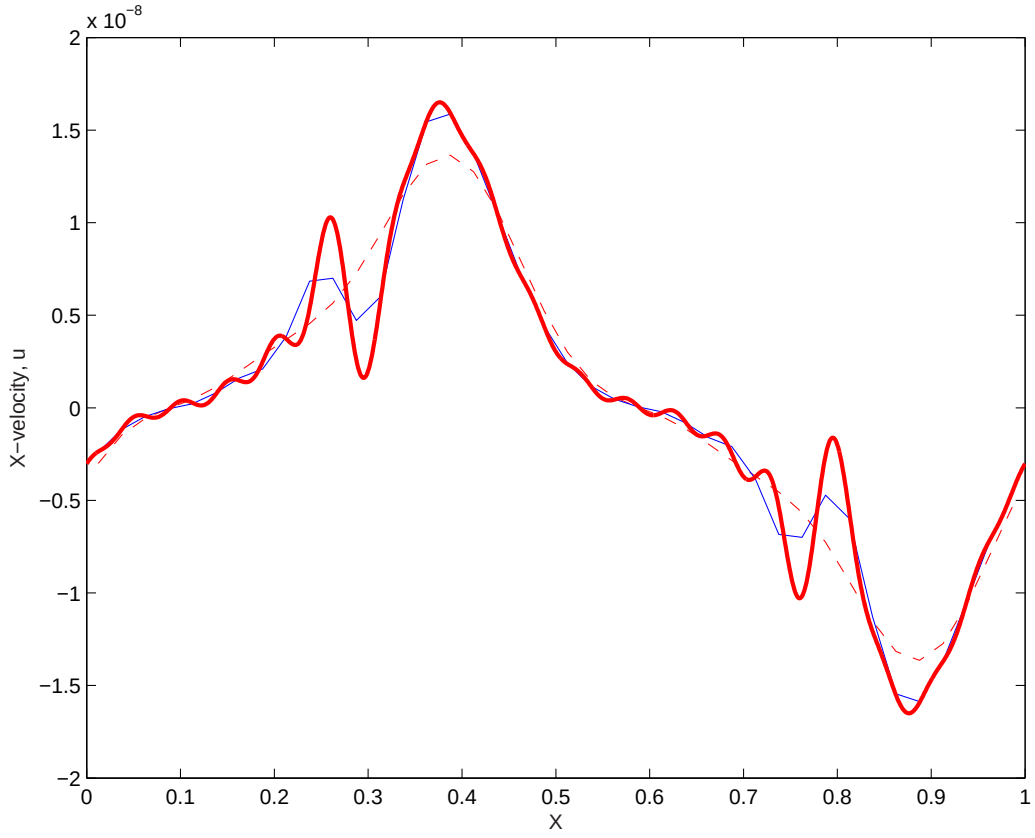

Figure 2.2: Solutions computed using the Discontinuous Galerkin 2nd (dashed line) and 3rd order (thin line) schemes on 40 cells. The thick line is the exact solution at $t = 3$. The 2nd order scheme has difficulty resolving the smaller wavelength features, but the 3rd order scheme captures these features better.

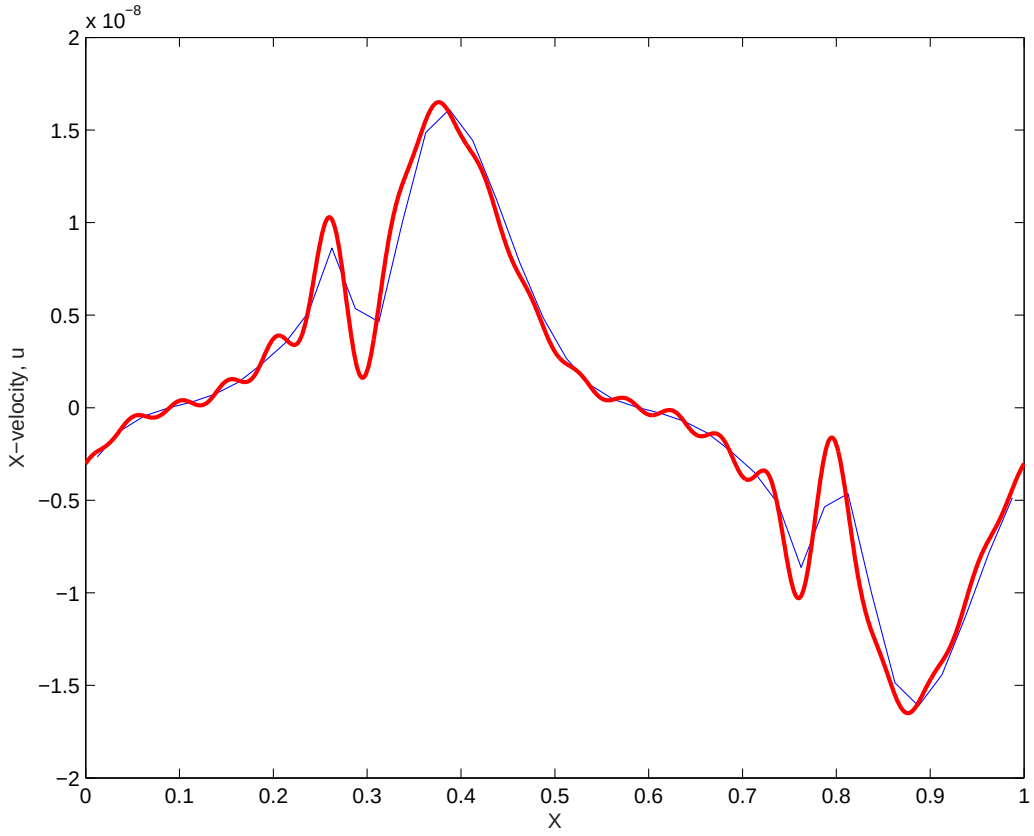

Figure 2.3: Solutions computed using the Wave Propagation (thin line) schemes on 40 cells. The thick line is the exact solution at $t = 3$. The solution is captured well as the Wave Propagation scheme has very little dissipation when run at CFL of 1.

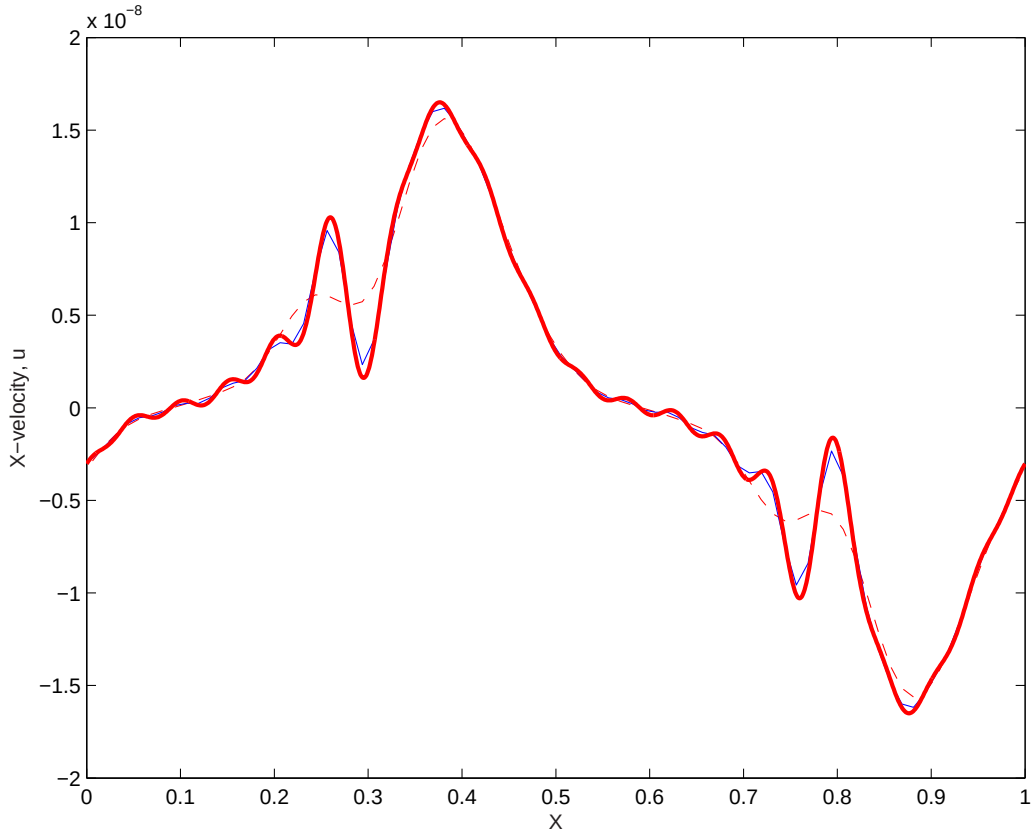

Figure 2.4: Solutions computed using the Discontinuous Galerkin 2nd (dashed line) and 3rd order (thin line) schemes on 80 cells. The 2nd order scheme has difficulty resolving the smaller wavelength features, but the 3rd order scheme matches the exact solution very well.

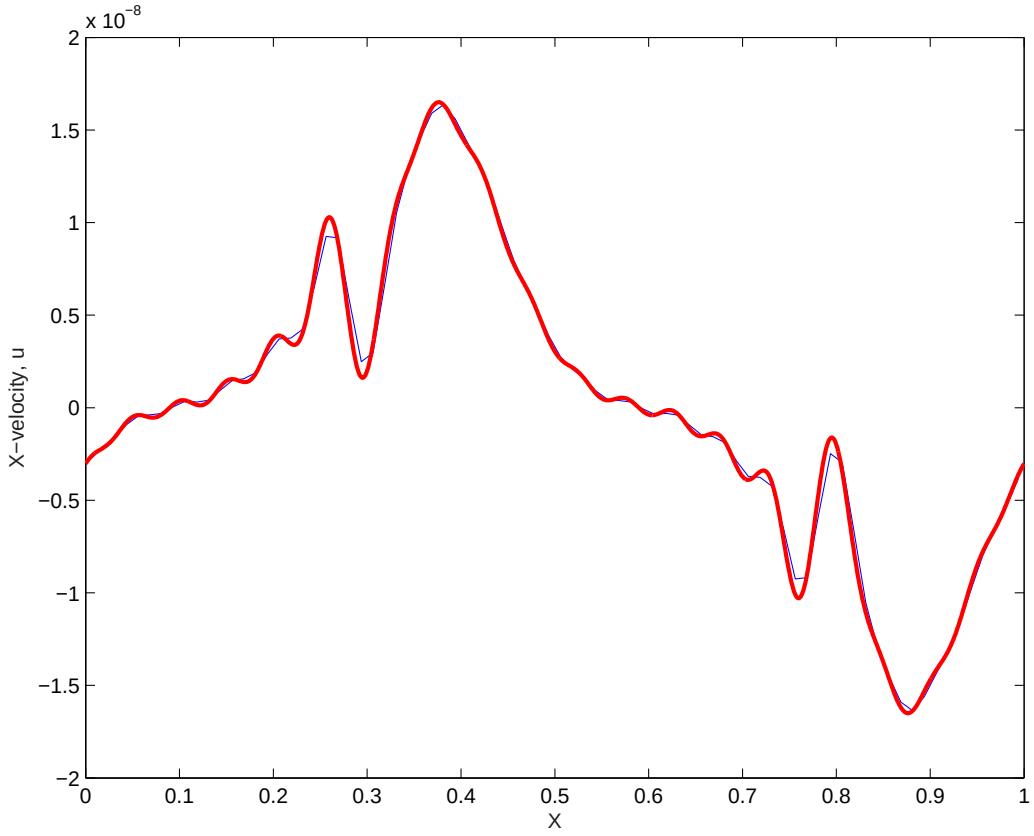

Figure 2.5: Solutions computed using the Wave Propagation (thin line) schemes on 80 cells. The thick line is the exact solution at $t = 3$. The solution is captured well as the Wave Propagation scheme has very little dissipation when run at CFL of 1.

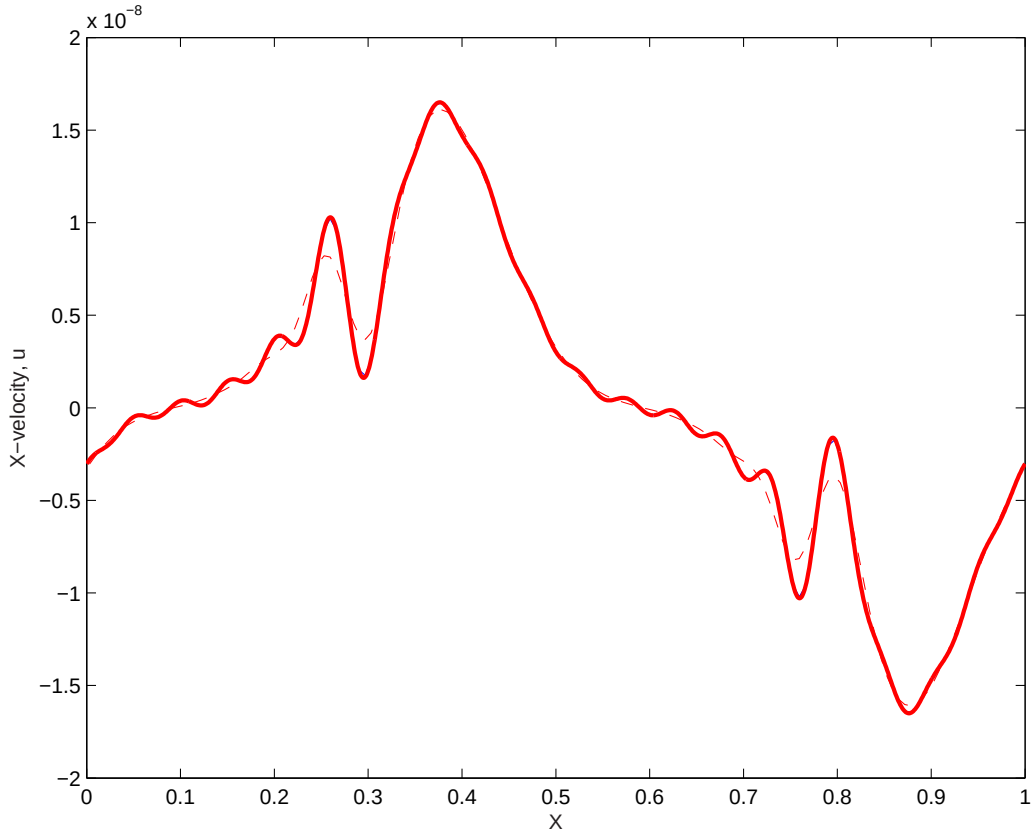

Figure 2.6: Solutions computed using the Discontinuous Galerkin 2nd (dashed line) and 3rd order (thin line) schemes on 160 cells. For this grid resolution the 2nd order solution matches the exact solution very well while the 3rd order solution is indistinguishable from the exact solution.

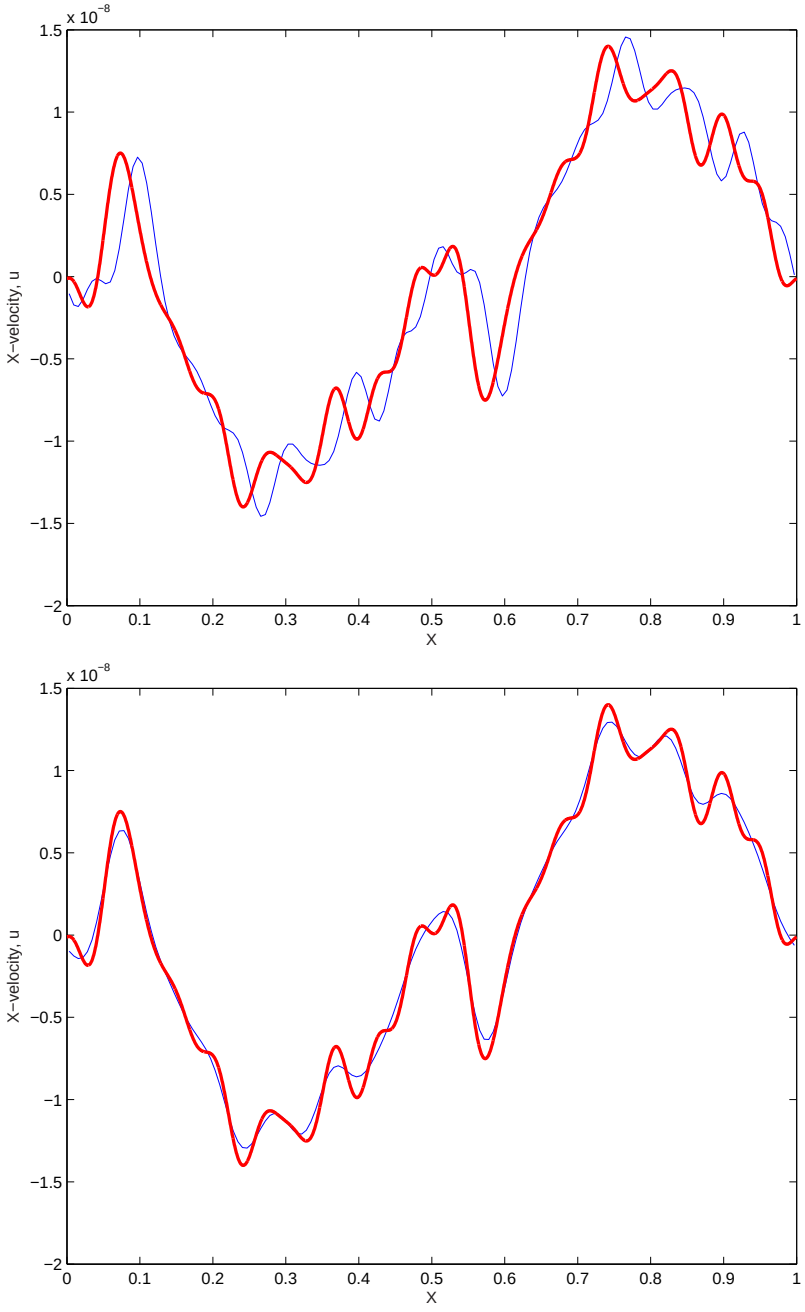

Figure 2.7: Solutions computed using Wave Propagation scheme (upper panel) and the Discontinuous Galerkin (DG) 2nd order schemes (lower panel) on 160 cells for $\omega_c = 100$. The Wave Propagation scheme has significant phase error while the DG scheme resolves the exact solution (thick line) without any phase error.

compared to the DG scheme. This is as ω_c increases the contribution of the source term as compared to the advection terms increases and the source-term splitting used in the Wave Propagation scheme introduces a phase error in the solution as is seen in Fig. (2.7). Taking smaller time steps (i.e., CFL number less than 1) helps reduce this phase error but now significant diffusion is introduced in the solution and small wavelength features are not captured well. In this case of $\omega_c = 100$ the DG shows much superior performance for the same grid resolution. However, it must be kept in mind that the Wave Propagation scheme runs about 5-9 times faster than the DG method and hence the advantages of the DG scheme can be offset by simply refining the grid, reducing the phase error, but still using the same computational resources.

Another caveat on comparing the two schemes is that the DG will perform better if the eigenvalues of the flux Jacobian are are significantly different. This is because the CFL number is computed using the fastest speed and when CFL of 1 is used this fastest wave has very little dissipation in the Wave Propagation scheme. However, the slower waves will be dissipated and hence the physics at slow time scales will not be captured as accurately. The DG scheme, on the other hand, is not very sensitive to the CFL number used as long as it is less than that required by stability. Thus all waves, even the slow wave physics will be captured about as well as the fast wave physics. Thus in those systems of equations in which there is a significant spread in the flux eigenvalues the DG method may perform better.

2.6.2 A shock-tube problem

In the previous section it was shown that the DG scheme is beneficial for linear problems when ω_c is large or when the eigenvalues of the flux Jacobian have a significant spread. In this section a non-linear test problem, the Sod shock-tube problem of Euler equations, is solved for the dispersive Euler equations. In the absence of dispersion ($\omega_c = 0$) the solution is shown in Fig. (2.8).

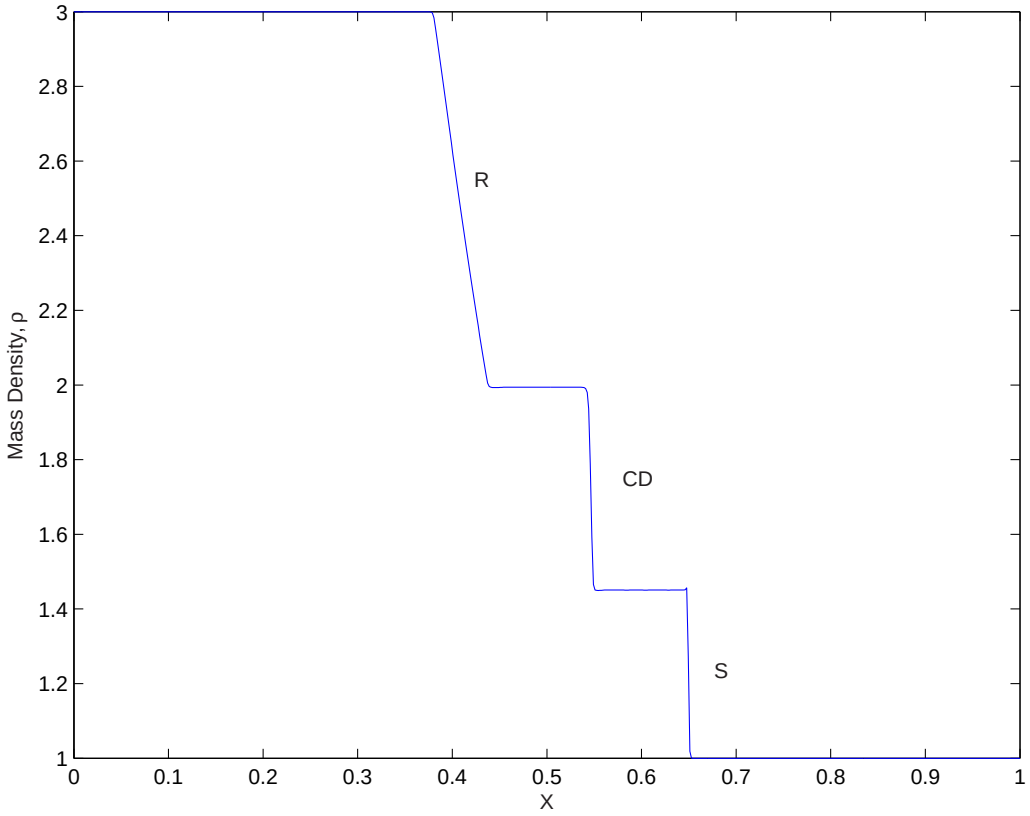

Figure 2.8: Solution to Sod shock-tube problem without dispersion ($\omega_c = 0$). The various parts of the solution are labeled as follows: contact discontinuity: CD, rarefaction wave: R, shock: S.

Simulations were performed for $\omega_c = 100$, and with initial conditions given by

$$\begin{pmatrix} \rho \\ p \end{pmatrix} = \begin{pmatrix} 3.0 \\ 3.0 \end{pmatrix} \quad x < 0.5 \tag{2.89}$$

and

$$\begin{pmatrix} \rho \\ p \end{pmatrix} = \begin{pmatrix} 1.0 \\ 1.0 \end{pmatrix} \quad x \geq 0.5 \tag{2.90}$$

on a domain $x \in [0, 1]$ with 400 cells and $\gamma = 1.4$. Figure (2.9) shows the solution computed using the Wave Propagation scheme. It is clear that most flow features, except the small wavelength waves, are captured well. Figure (2.10) show a detail view of the solution near the "compound wave". It is seen that in this region the numerical method is unable to capture the small oscillations that occur in the fluid density. Figure (2.11) shows the solution computed using the DG 3rd order spatial scheme. Comparing these results with those in Fig. (2.9) shows that both methods give almost identical results for this problem.

This simulation illustrates a number of interesting things. First, the presence of dispersive source terms significantly changes the global solution of the equation. Second, in the presence of discontinuities or strong non-linearities the Wave Propagation scheme and the DG scheme give equally accurate solutions. This is because the limiters in the DG scheme, required for stability in presence of shocks, reduce its accuracy. Developing limiters that do not affect the accuracy of the DG scheme away from discontinuities is a active research area.

The simulations presented in this section show that the higher order accuracy of the Discontinuous Galerkin scheme is useful for linear problems when (a) the dispersive source term dominates (b) the flux Jacobian eigenvalues show a large spread. For non-linear problems, specially in the presence of discontinuities, the DG and Wave Propagation schemes give equally accurate results. For those non-linear problems in which the solution varies rapidly but is still smooth and limiters do not need to be

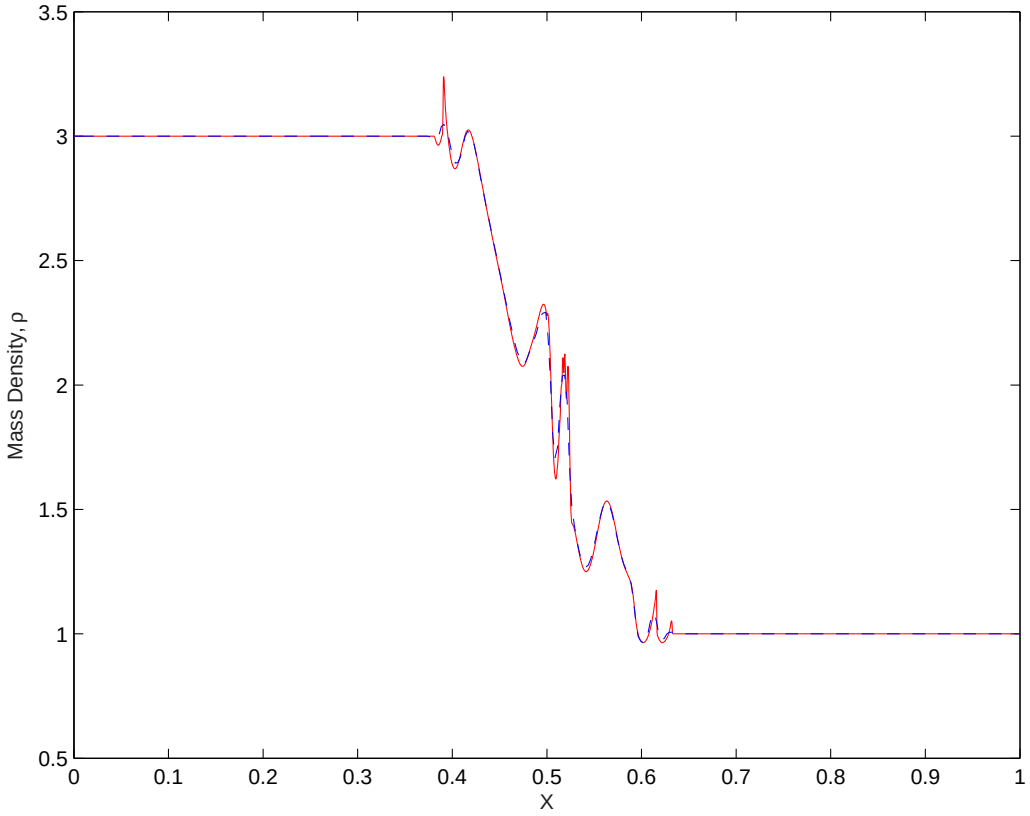

Figure 2.9: Solution to Sod shock-tube problem on 400 cells using the Wave Propagation scheme (dashed line) compared to "exact" solution (solid line). Except for small scale features the numerical solution compares well with the exact solution.

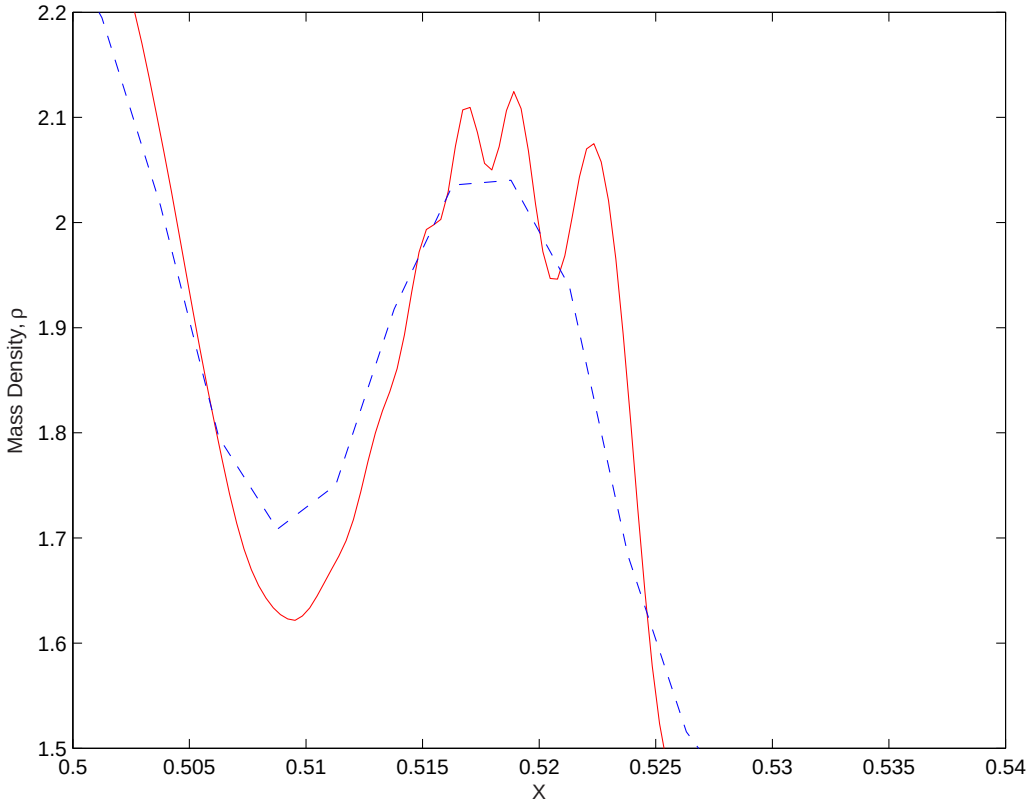

Figure 2.10: Details of Sod shock-tube problem on 400 cells using the Wave Propagation scheme (dashed line) compared to "exact" solution (solid line). The scheme is unable to follow the small wavelength features near the "compound" wave.

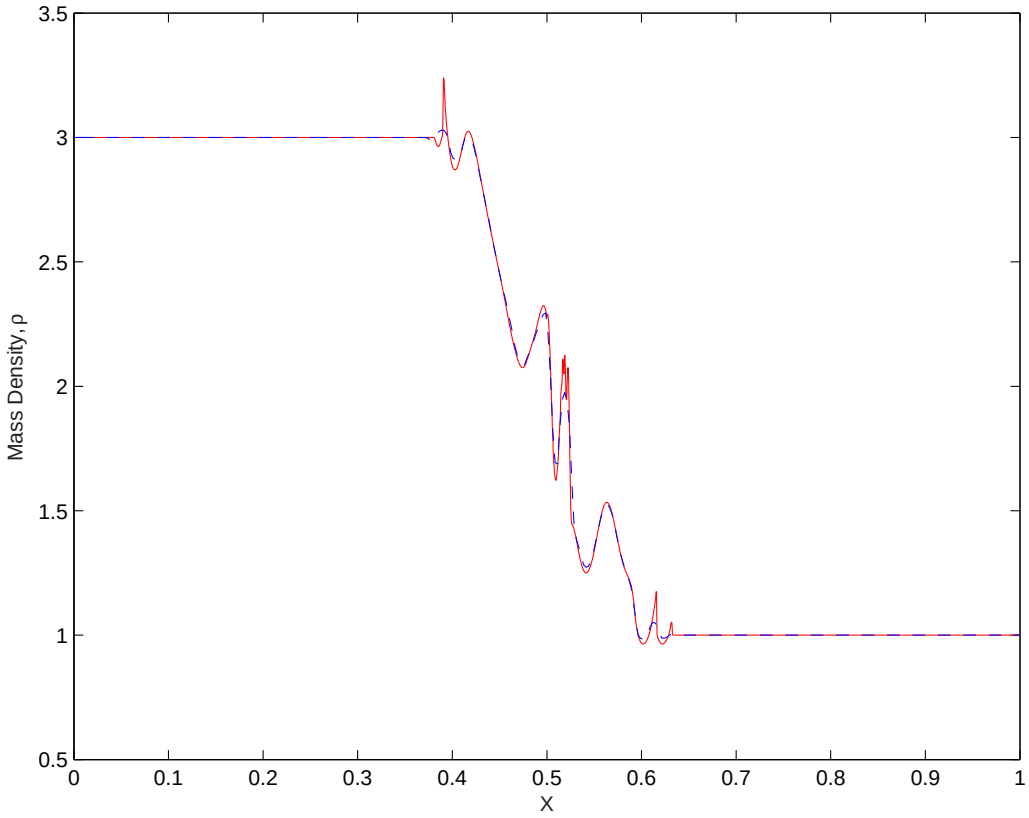

Figure 2.11: Solution to Sod shock-tube problem on 400 cells using the Discontinuous Galerkin 3rd order scheme (dashed line) compared to "exact" solution (solid line). Except for small scale features the numerical solution compares well with the exact solution. The DG solution is almost exactly the same as the the Wave Propagation solution.

applied the DG scheme should be superior, at least for the same grid resolution as for the Wave Propagation scheme.

The aspects of the two schemes mentioned in this section are not well studied and need to be investigated further. In this thesis all results are computed using the Wave Propagation scheme. Results with the DG scheme have been published by Loverich, Hakim and Shumlak[23] and show that both the schemes work equally well for most problems to capture Two-Fluid physics studied in this thesis.

Chapter 3
APPLICATIONS OF THE TWO-FLUID MODEL

3.1 Introduction

In the following sections several example applications of the Two-Fluid algorithms developed in this thesis are presented. The applications studied are a one-dimensional Riemann problem, propagation and interaction of solitons in a homogeneous plasma, a two-electron fluid instability and collisionless reconnection. Results for these problems obtained with reduced fluid models exist in the literature and hence are used to benchmark the Two-Fluid results. For all simulations the speed of light is set to $c = 1$. Distances and times are measured, unless otherwise noted, in units of light transit time across the domain.

3.2 Two-Fluid Riemann Problem

In many ways the one dimensional *Riemann problem* defined by

$$\frac{\partial \mathbf{q}}{\partial t} + \frac{\partial \mathbf{f}}{\partial x} = \mathbf{s}, \quad x \in \mathbb{R}, \tag{3.1}$$

with initial conditions $\mathbf{q}(x < 0, 0) = \mathbf{q}_l$ and $\mathbf{q}(x > 0, 0) = \mathbf{q}_r$, where $\mathbf{q}_{l,r}$ are constant vectors, is fundamental to the solution of hyperbolic balance laws. Solutions to the Riemann problem for the Two-Fluid equations are presented in this section. The Riemann problem selected is a generalization of the Brio-Wu shock-tube problem[6]

commonly used to benchmark MHD codes. The initial conditions are

$$\begin{bmatrix} \rho_e \\ u_e \\ v_e \\ w_e \\ p_e \\ \rho_i \\ u_i \\ v_i \\ w_i \\ p_i \\ B_x, \\ B_y, \\ B_z, \\ E_x, \\ E_y, \\ E_z \end{bmatrix}_l = \begin{bmatrix} 1.0\frac{m_e}{m_i} \\ 0 \\ 0 \\ 0 \\ 5\times10^{-5} \\ 1.0 \\ 0 \\ 0 \\ 0 \\ 5\times10^{-5} \\ 0.75 \\ 1.0 \\ 0 \\ 0 \\ 0 \\ 0 \end{bmatrix} \qquad \begin{bmatrix} \rho_e \\ u_e \\ v_e \\ w_e \\ p_e \\ \rho_i \\ u_i \\ v_i \\ w_i \\ p_i \\ B_x, \\ B_y, \\ B_z, \\ E_x, \\ E_y, \\ E_z \end{bmatrix}_r = \begin{bmatrix} 0.125\frac{m_e}{m_i} \\ 0 \\ 0 \\ 0 \\ 5\times10^{-6} \\ 0.125 \\ 0 \\ 0 \\ 0 \\ 5\times10^{-6} \\ 0.75 \\ -1.0 \\ 0 \\ 0 \\ 0 \\ 0 \end{bmatrix} \tag{3.2}$$

where $m_e/m_i = 1/1832.6$. The only remaining unspecified quantity is the ion charge to mass ratio, $r_i \equiv q_i/m_i$. In terms of this ratio the ion Larmor radius is $r_{Li} \propto 1/r_i$ and the ion skin depth is $l_i \propto 1/r_i$. Thus it is clear from the discussion of Two-Fluid effects (Eqs. (1.54) and (1.55)) that as r_i increases the Larmor radius and skin depth become smaller and the solutions obtained with the Two-Fluid model should approach the solutions obtained with MHD model. Simulations with $q_i/m_i = 1, 10, 100, 1000$ were carried out. These charge to mass ratios correspond to ion skin depth of $1, 1/10, 1/100, 1/1000$, calculated with a reference magnetic field of 1. Thus, for example, for the $q_i/m_i = 1$ simulation the domain length is the same as the ion-skin depth and for the $q_i/m_i = 1000$ the domain length is 1000 times the ion-skin depth. With decreasing ion-skin depth the plasma regime tends toward the ideal

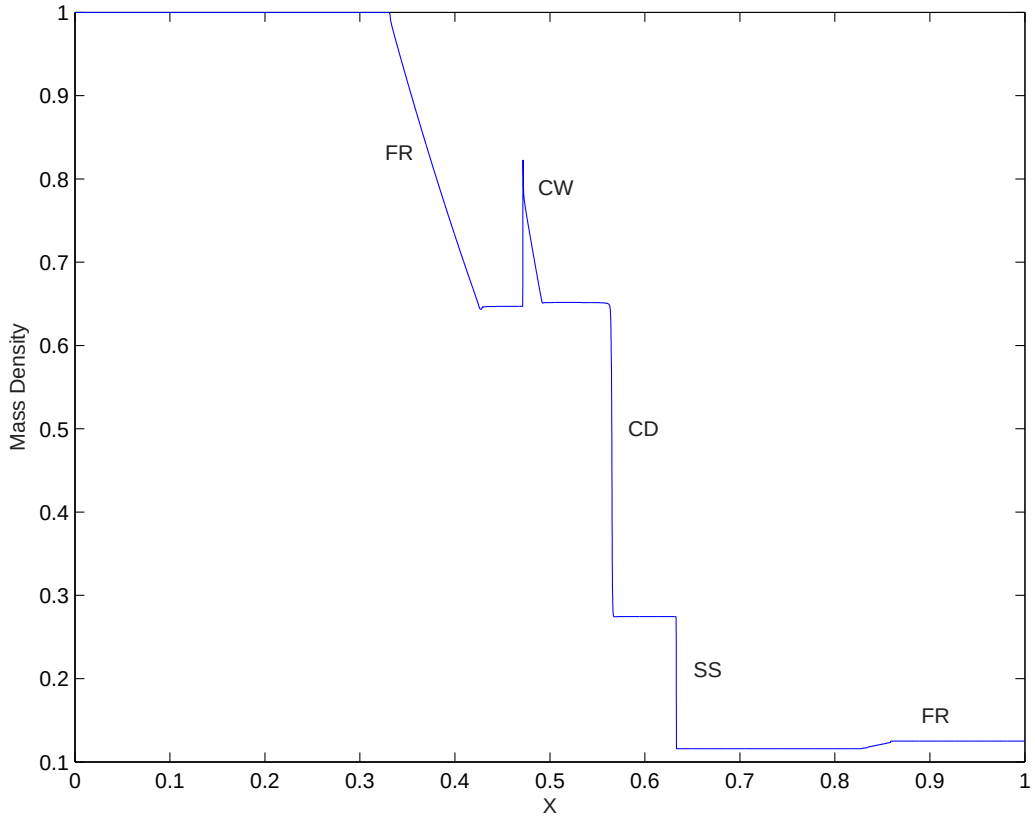

Figure 3.1: Fluid mass density at t=10 from a ideal MHD simulation. The various parts of the shock are labeled as follows: contact discontinuity: CD, compound wave: CW, fast rarefaction wave: FR, slow shock: SS.

MHD limit, as our simulations below confirm. The results are presented for a grid of 50000 cells. Although the number of grid cells may seem excessive the complex flow physics shown below cannot be resolved on coarser grids, specially with the correct value of the electron-ion mass ratios used.

Figure 3.1 shows the mass density computed at $t = 10$ with the ideal MHD model. The solution was computed using an existing shock-capturing non-ideal MHD code[**?**] by turning off all non-ideal effects. The initial conditions used for the ideal MHD simulation are the same as the standard Brio-Wu shock problem described above. The

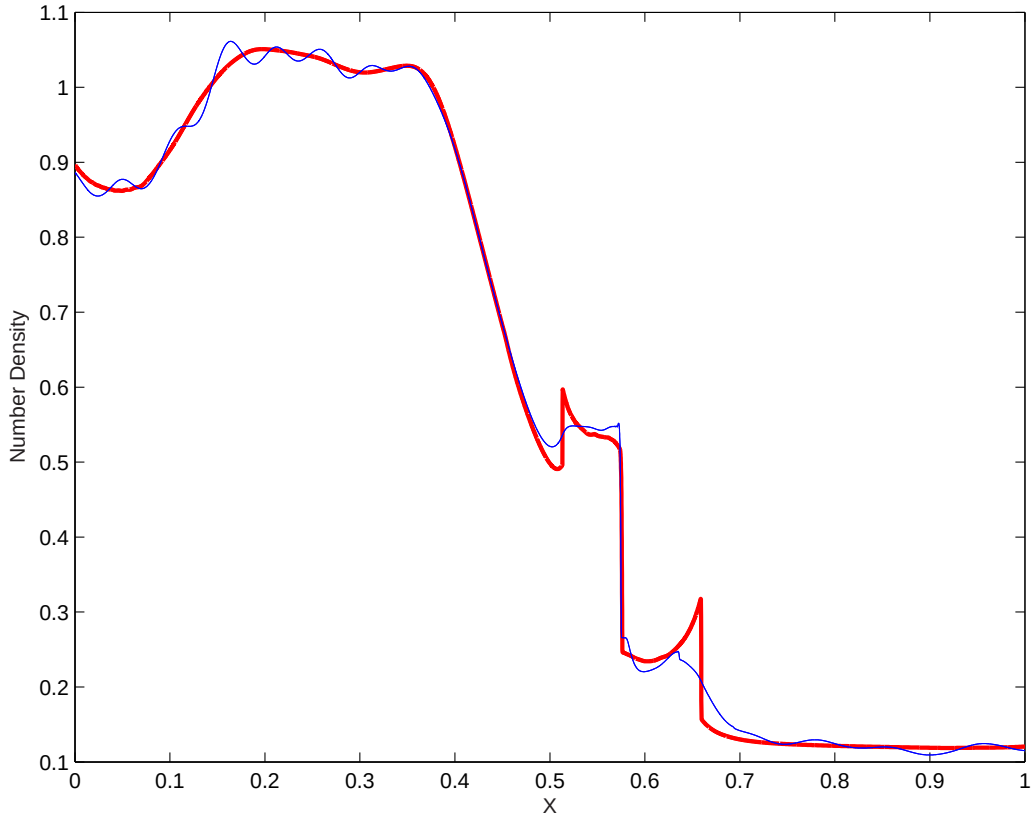

Figure 3.2: Electron (light line) and ion (heavy line) number density at t=10 with $q_i/m_i = 1$.

MHD fluid density was initialized using the ion density and fluid-pressure using total electron and ion pressure. The MHD result serves to compare the solutions obtained with the Two-Fluid model. Comparing the computational time for the ideal-MHD and the full Two-Fluid simulations we found that the Two-Fluid simulations took about 100 times longer. This is not surprising as in the full Two-Fluid system the fastest wave speed is the speed of light which is much larger than the fastest wave speed of the ideal-MHD system (the fast magnetosonic speed).

In Fig. 3.2 the number densities of electrons and ions are plotted for $q_i/m_i = 1$. This figure shows that for low q/m ratio as the Lorentz force is smaller the fluids can

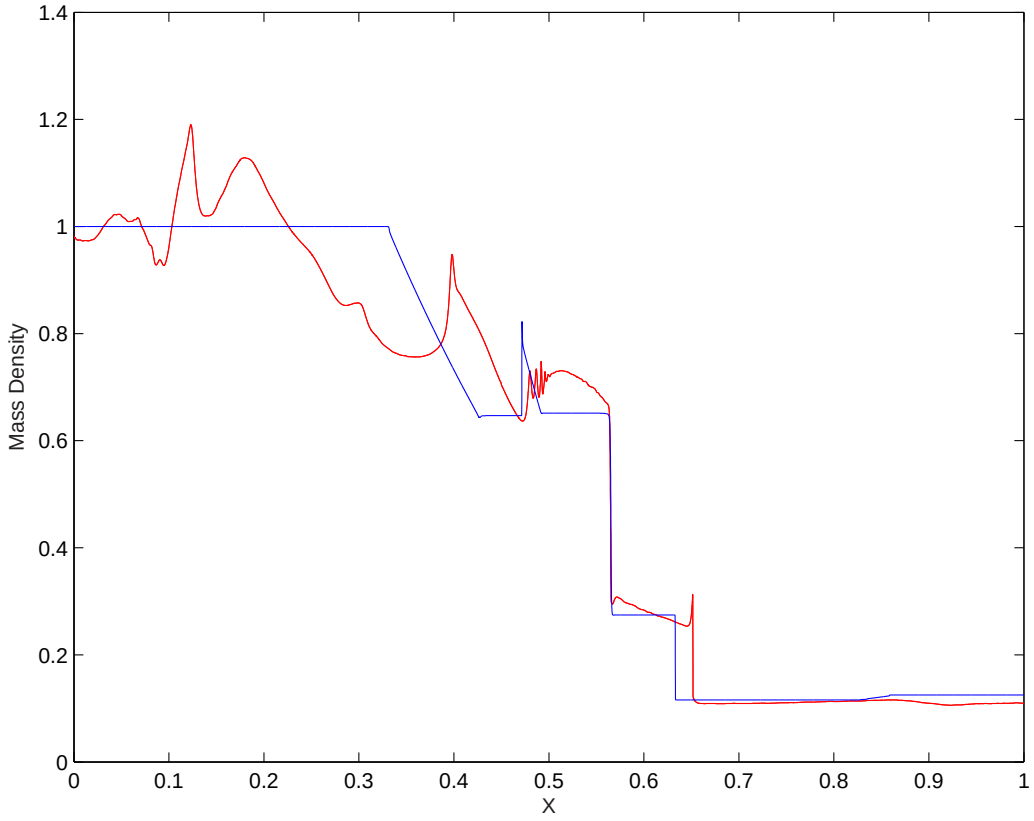

Figure 3.3: Ion mass density (red line) at t=10 with $q_i/m_i = 10$. Also plotted is the ideal MHD mass density (blue line). The Two-Fluid solution shows the compound wave and slow shock developing while the contact discontinuity is at the correct location.

have significant charge separation. In MHD and Hall MHD it is assumed that the electron and ion fluids have the same number densities, i.e. $n_e = n_i$.

Figure 3.3 shows the mass density of the ion fluid for $q_i/m_i = 10$. For comparison ideal MHD results are superimposed. Even though the Two–Fluid solution is significantly different from the MHD results the contact discontinuity is in the correct location and the compound wave has started to form. A close-up view of the number densities of the electrons and ions around the compound wave is shown in Fig. 3.4.

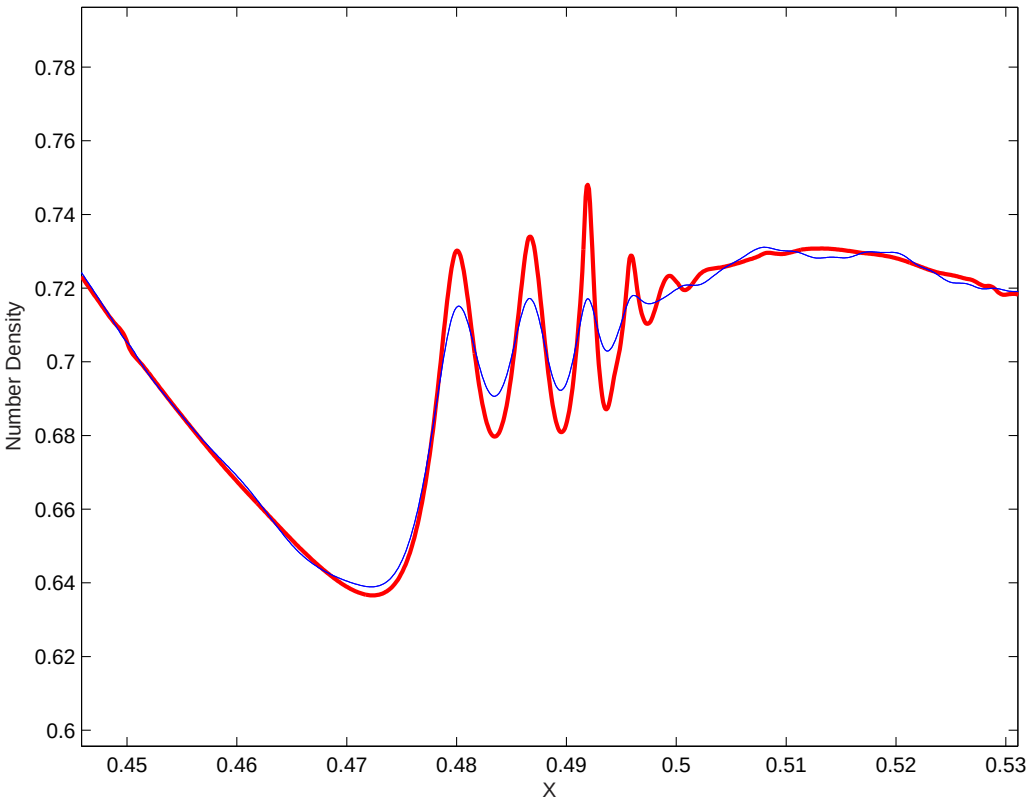

Figure 3.4: Ion (heavy line) and electron (light line) number densities at t=10 with $q_i/m_i = 10$ around the compound wave. The dispersive waves are formed due to charge separation effects.

It is seen that there is significant charge separation around the forming compound wave. In general charge separation leads to dispersive waves as is clearly visible in this plot. Dispersive effects due to charge separation play an important role in the formation of ion-acoustic solitons as discussed in a later section.

Figure 3.5 shows the mass density of the ion fluid for $q_i/m_i = 1000$. The Two–Fluid solutions are now clearly MHD like: the compound wave has now formed and fast rarefaction waves (upstream and downstream) and contact discontinuity are all in the correct locations. The slow shock, however, seems to be moving slower than the MHD result. A close-up of the solutions is shown in Fig. 3.6. Dispersive waves are clearly seen and these are conjectured to be dispersive magnetosonic waves, as evidenced from dispersion relations computed and presented as Fig. (11) in Loverich and Shumlak[36].

In conclusion, the Two–Fluid Riemann problem serves not only as an important benchmark for the algorithms, but also highlights the complex Two–Fluid physics not captured in the simpler MHD model.

3.3 Weibel Instability

The Weibel instability[40] is an efficient mechanism for the generation of magnetic fields in anisotropic (i.e. anisotropic distribution function) plasmas. To illustrate the versatility of the algorithms developed here the Weilbel instability is simulated in which an anisotropic electron distribution is mimicked using two electron fluids streaming in opposite directions. A third ion fluid is added, however, its dynamics is not simulated. The Weibel instability cannot be simulated using any single fluid model like MHD or Hall MHD.

The physical mechanism for the Weibel instability is easy to understand. When the electric currents carried by the electron fluids are displaced, one with respect to the other, the repulsion of the two oppositely directed currents reinforces the initial displacement. As a result larger and larger magnetic field is produced as time

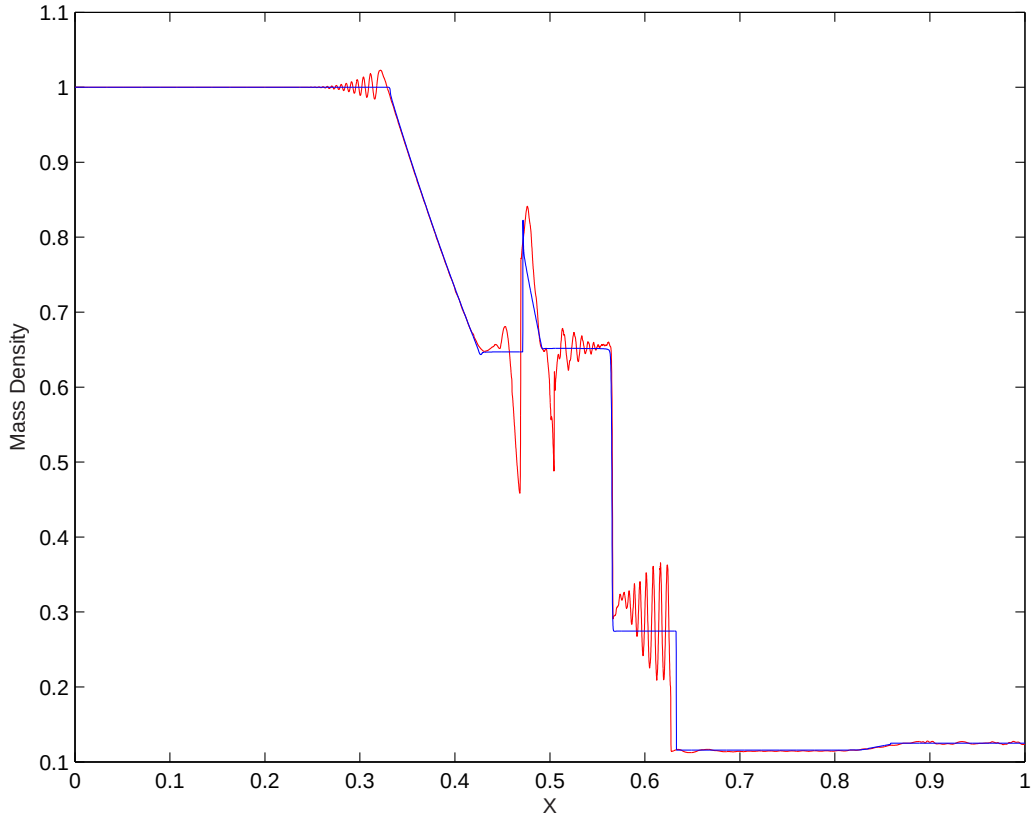

Figure 3.5: Ion mass density (red line) at t=10 with $q_i/m_i = 1000$. Also plotted is the ideal MHD mass density (blue line). The compound wave has now formed in the Two-Fluid solution. The fast rarefaction waves (upstream and downstream) and contact discontinuity are all in the correct locations. The slow shock, however, seems to be moving slower than in the MHD solution.

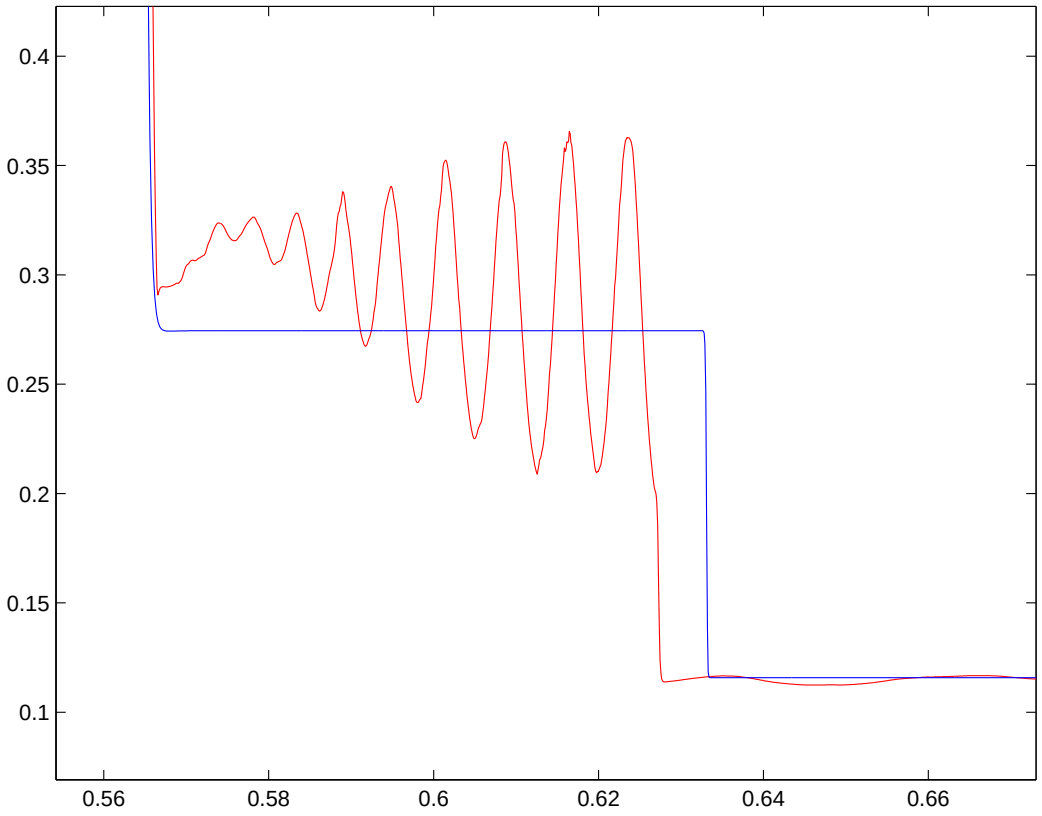

Figure 3.6: Close up of ion mass density (red line) around the slow shock at t=10 with $q_i/m_i = 1000$. Also plotted is the ideal MHD mass density (blue line). The ion density oscillations are due to dispersive magnetosonic waves.

advances. Within the linear regime of the instability it is shown that the magnetic field is localized and eventually becomes singular. For short time periods (on the order of a few electron cyclotron periods $2\pi/\omega_{ce}$) the ions are assumed to be a stationary neutralizing background.

In this section the one-dimensional evolution of the Weibel instability in an inhomogeneous plasma is studied[9, 10, 8]. The electron streams are spatially nonuniform and the plasma density may vary in the direction perpendicular to the streams. This situation arise in the wake of a ultra-short ultra-intense laser propagating in a under dense plasma. In this inhomogeneous case the electron fluid develop a spatial singularity around which the magnetic field generated by the instability becomes more and more concentrated. In the simple case of two symmetric electron beams (equal density, opposite and equal speeds) the location of the singularity can be calculated analytically.

Two electron fluids denoted by the subscripts $1, 2$ are initialized with equal densities and equal and opposite velocities, i.e. $\mathbf{u}_1 = -\mathbf{u}_2 = u(y)\mathbf{e}_x$, where $\mathbf{e}_x$ is a unit vector along X axis. This ensures that there is no net initial current and hence no initial magnetic field. The ion density is initialized to ensure neutrality, i.e $\varrho_c = e(n_i - n_1 - n_2) = 0$ which means there is no initial electric field. The velocity profile is calculated using[9]

$$u(y) = u_\infty + \frac{\delta}{2}[1 + \tanh(y/l)]\mathbf{e}_x. \tag{3.3}$$

The calculations are carried out in the domain $y \in [-L_y, L_y]$ where $L_y = 70l$ and all lengths are measure in units of electron skin depth c/ω_{ce} and time in units of inverse electron cyclotron frequency. Outflow boundary conditions are imposed in the Y direction. For the simulations presented here $l = 1$, $u_\infty = 0.25$, $\delta = 0.25$. This equilibrium is perturbed using very small perturbations in each of the flow variables. The form of the perturbation, $f(y)$, is

$$f(y) = \Delta \exp(-y^2/\sigma) \sin(k_0 y - \pi/2), \tag{3.4}$$

where $\Delta = 10^{-12}$ and $\sigma = 80/l$. To measure growth rated the mean amplitude of a perturbed variable, q, is calculated using the expression

$$\langle q \rangle(t) \equiv \left[\frac{1}{L_y} \int_{-L_y}^{L_y} q(y,t)^2 dy \right]^{1/2} . \tag{3.5}$$

Simulations were performed with wave numbers $k_0 = 0.01, 0.2, 1.0, 2.0, 5.0$. The perturbed out of plane magnetic field $\langle B_z \rangle$ was tracked to calculate the growth rate of the instability.

Figure 3.7 shows the mean amplitude of the out of plane magnetic field, $\langle B_z \rangle$, versus time. It is seen that the growth rates vary between 0.47 and 0.55 are hence almost independent of wave number. This is consistent with the linear analysis of the instability[31]. Figure 3.8 shows the evolution of the magnetic field in time. A strong peak of magnetic field is formed near $y = 0$, where the equilibrium gradients in the electron beams are maximum. This process develops on a characteristic time scale of $t \approx 5$ which depends on the inhomogeneity scale length l, while it is independent of the wave number k_0. After $t = 5$, B_z increases exponentially and eventually becomes singular. A linear analysis[31] shows that the singularity occurs at the point y_0 where $2u(y_0) - \gamma^2 = 0$, where γ is the growth rate. For the results shown in the figure, $k_0 = 0.2$ and $\gamma = 0.5488$. Using Eq. (3.3), gives $y_0 = 1.09$ which is consistent with the location in Fig. 3.8.

3.4 Soliton Propagation

Soliton propagation in fluids and plasmas is an active area of research[1, 25, 26]. Much previous work has been done in plasma physics on soliton propagation in the weakly nonlinear limit. In this limit, using expansion techniques, the Korteweg-de Vries (KdV) equation can be derived and either solved numerically or a particular class of solutions studied analytically. An example of this approach is the study of ion-acoustic solitons[12] in which the electrons are assumed to be a massless isothermal fluid and the ions are assumed cold (i.e. the ion pressure vanishes). With these assumptions

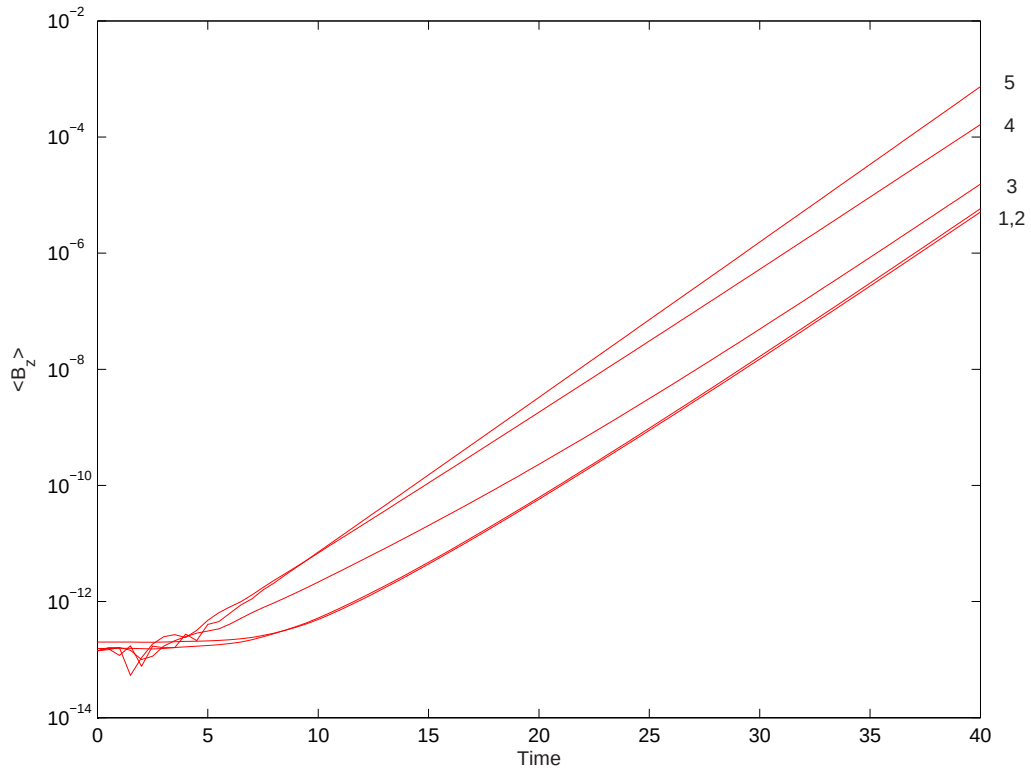

Figure 3.7: Mean amplitude of the magnetic field $\langle B_z \rangle$ versus time for $u_\infty = 0.25$ and $\delta = 0.25$. The curves labeled 1 to 5 correspond to wave numbers $k = 0.01, 0.2, 1.0, 2.0$ and 5.0 respectively.

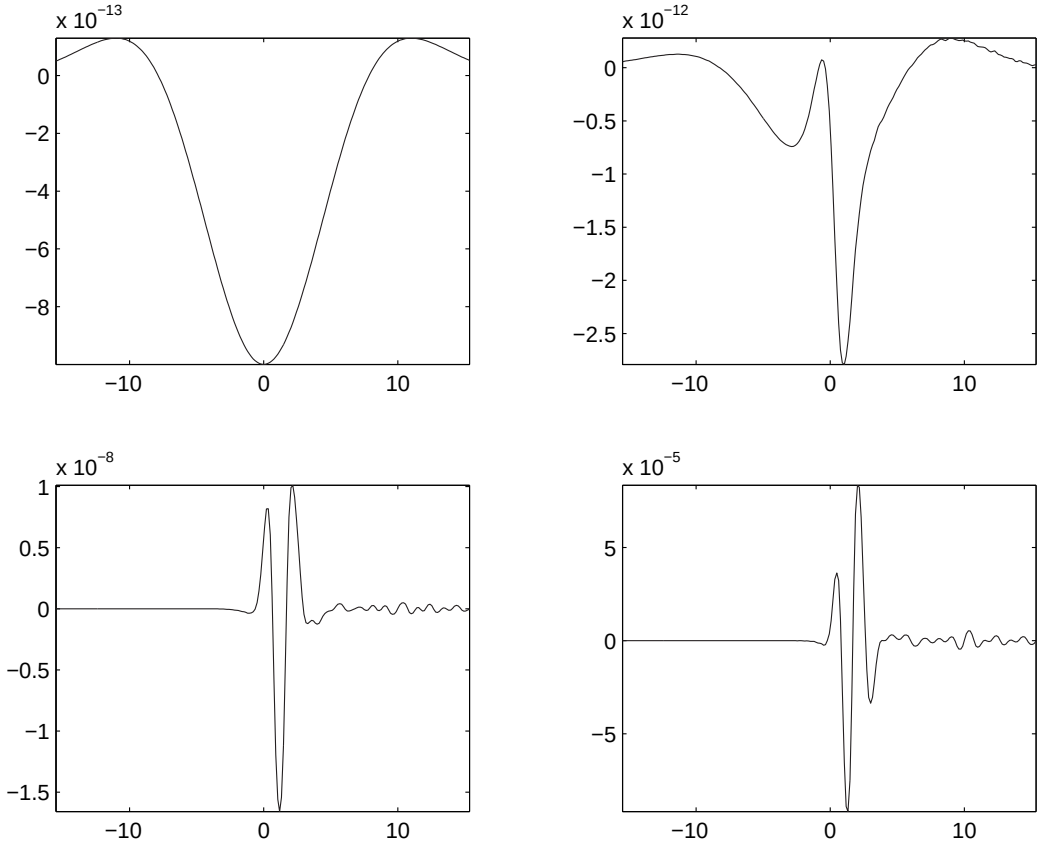

Figure 3.8: Evolution of out of plane magnetic field (B_z) with time. The frames correspond to, from left to right, top to bottom, $t = 0, 7, 25, 40$. The magnetic field is seen to localize and eventually become singular near $y = 0.1$. The simulation parameters are $k_0 = 0.2$, $u_\infty = 0.25$, $\delta = 0.25$.

a KdV equation can be derived which describes the propagation of soliton structures in the ion fluid. An important outcome of this analysis is that the dispersive effects needed to support soliton formation arise from non-neutral (charge-separation) effects. Thus ion-acoustic solitons cannot be simulated using fluid models which assume quasi-neutrality, like the MHD and Hall MHD models.

In this section simulations are carried out to show that ion-acoustic solitons can form from an initial density hump or "slug". These solutions are in the strongly non-linear regime and hence cannot be described with a standard KdV equation. Similar structures have been observed experimentally[11]. Numerical simulations of density slug induced solitons were carried out by Baboolal[1] who assumed an isothermal electron fluid and an adiabatic ion fluid with adiabatic index $\gamma = 3$. With these assumptions there is no need to solve an energy equation as the equation of state $p\rho^{-\gamma} =$ constant is used to calculate the pressure. In the simulation performed here these assumptions are not made. It is shown that a stable stationary structure, not observed in the simulations of Baboolal, arises in addition to the traveling solitons. Such stationary density structures cannot be supported in adiabatic fluids as a density gradient implies a pressure gradient which in turn implies flow.

The plasma is assumed to be stationary, i.e. $\mathbf{u}_e(x, t = 0) = \mathbf{u}_i(x, t = 0) = \mathbf{0}$. The electron and ion number densities are initialized as $n_e = n_i = n(x)$ where

$$n(x) = 1 + \exp(-\frac{1}{2}|x - x_c|), \tag{3.6}$$

where $x \in [0, L_x]$ and $x_c = L_x/4$. The ion-electron temperature ratio (where temperature, T, is computed from the relation $p = nT$) is set to 1/100. The initial pressure profile is set using $p_\alpha(x, t = 0) = n_\alpha T_\alpha$ for $\alpha \in \{e, i\}$. The domain size is $L_x = 12c/\omega_{pi}$ calculate using $n_i = 1$ and $q_i/m_i = 1$, and is discretized using 1500 cells. The electron-ion mass ratio is $m_e/m_i = 1/25$. The boundary conditions are periodic. The value x_c and boundary conditions were selected to ensure that solitons leaving the domain from one side would reappear from the opposite side and soliton

interaction would occur inside the domain and not on the boundaries.

Figures 3.9 and 3.10 show the time evolution of the ion density. It is seen that two solitons emerge from the initial slug and travel in opposite directions. The soliton speed is calculated and is approximately $1.01c_{si}$, where c_{si} is the ion fluid sound speed. This value agrees well with a linear analysis of ion-acoustic solitons. A trail of decaying plasma waves are also seen in the soliton wake. This feature is common to solitons generated in dispersive systems. As the boundary conditions are periodic the solitons reenter the domain and collide at $x = 10$. After collision the solitons reemerge with their shapes unchanged. Later in time the solitons merge with the stationary structure at $x = 4$ approximately recreating the initial conditions. The stationary structure is seen to be stable to interactions. For the grid (1500 cells) used the solitons cross the domain about 40 times before becoming significantly damped out. For a coarser grid the solitons damp out faster due to the grid diffusion.

The results obtained here compare well with those obtained by Baboolal. However in Baboobal's[1] simulations the central stationary structure does not form due to the selected equation of state. In the simulations performed here the pressure is constant across the stationary structure and hence the density there remains constant in time.

3.5 Collisionless Reconnection

Magnetic reconnection[33] is the process by which the topology of the magnetic field lines changes. In ideal MHD or ideal Hall MHD the field line topology cannot change and this is described by saying that field lines are "frozen" into the fluid (frozen into the electron fluid in case of ideal Hall-MHD). The situation is analogous to neutral ideal fluid flow in which vortex tube topology remains constant. However even small resistivity (viscosity in neutral fluids) can make the topology change and the field lines reconnect and this process is adequately described in the framework of resistive MHD or Hall-MHD.

However, in a collisionless plasma magnetic reconnection is also observed to occur

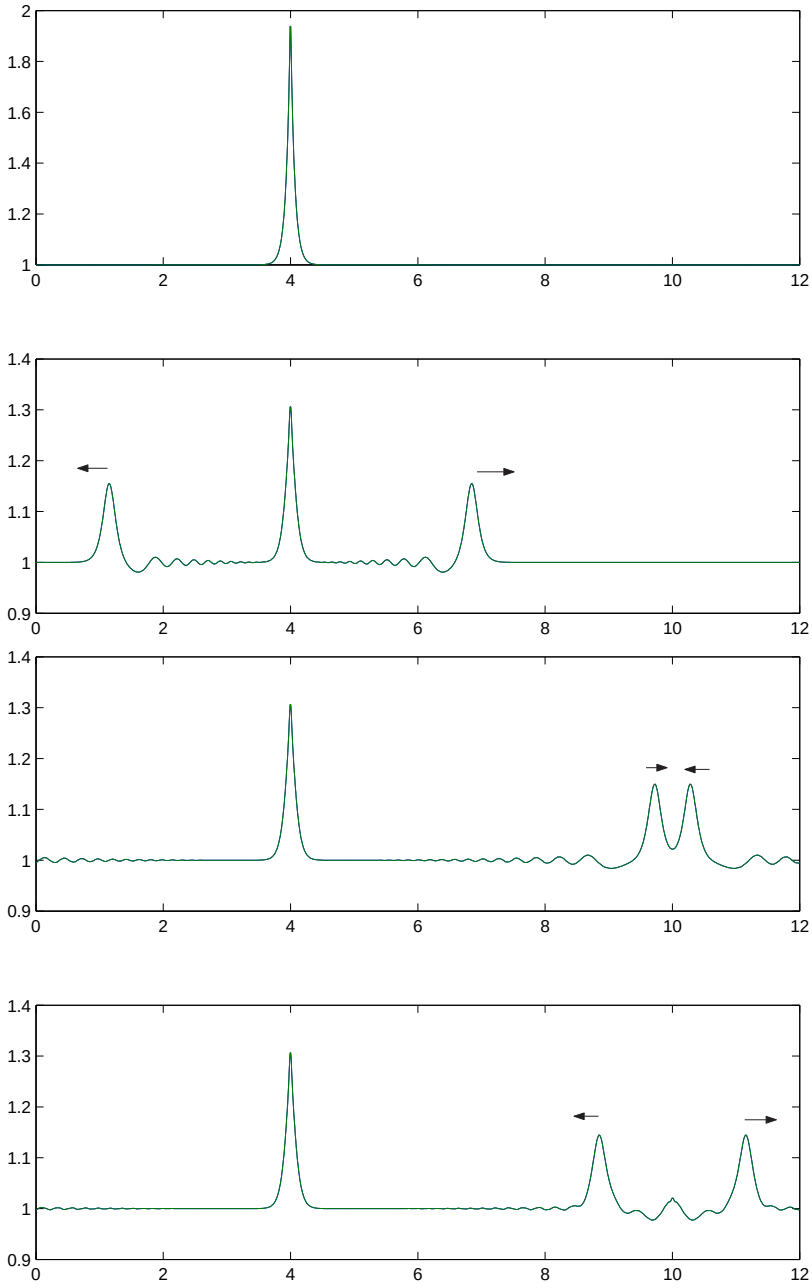

Figure 3.9: Ion mass density for soliton propagation and interaction. The frames correspond to, from top to bottom, $t = 0, 100, 200, 250$, measured in inverse ion-cyclotron frequency. The arrows show direction of propagation of the solitons. Solitons collide and reemerge without charge in shape.

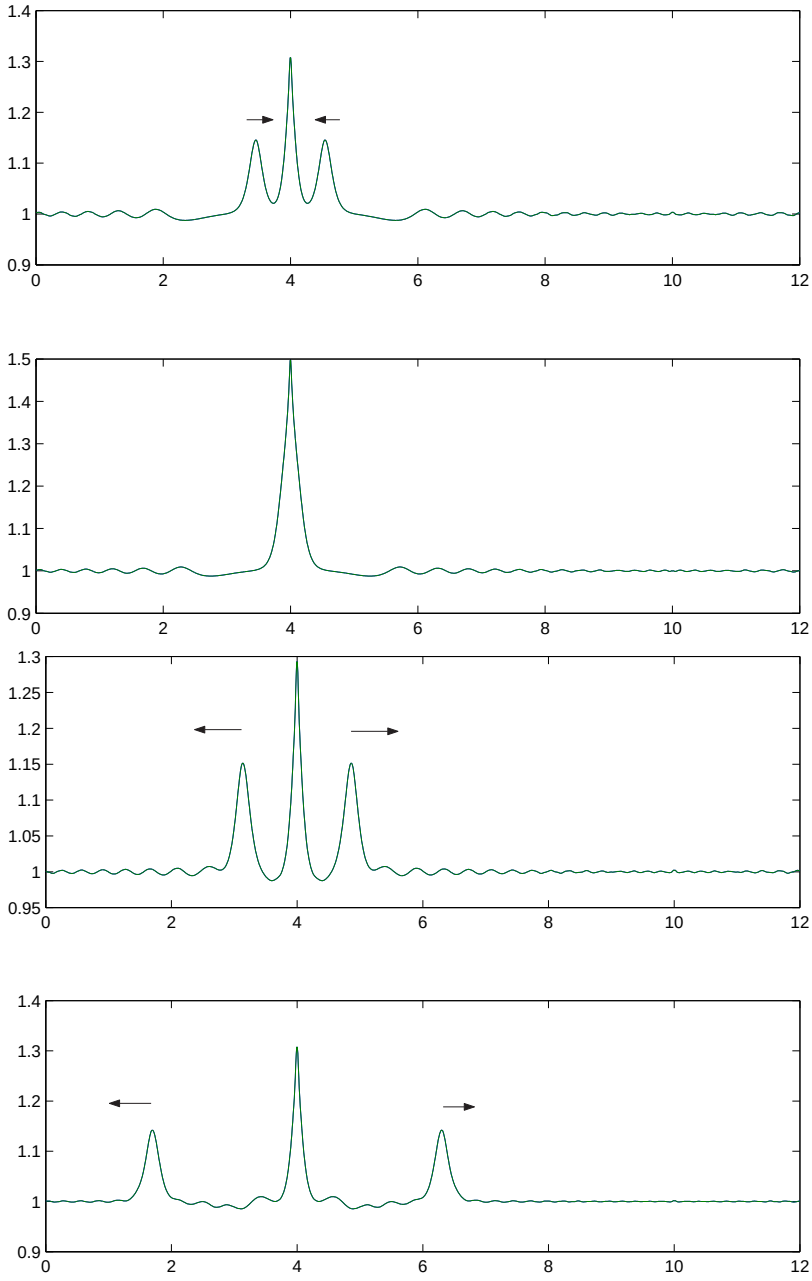

Figure 3.10: Ion mass density for soliton propagation and interaction. The frames correspond to, from top to bottom, $t = 400, 415, 450, 500$, measured in inverse ion-cyclotron frequency. The arrows show direction of propagation of the solitons. The two solitons combine with the central stationary structure to approximately recreate the initial conditions. The central structure is stable to interactions.

and at a much faster rate than in collisional plasmas. This *fast collisionless reconnection* is important in understanding many space plasma phenomena, for example, solar flares and the dynamics of the Earth's magnetotail during a geomagnetic substorm. To understand the mechanism of collisionless reconnection a number of plasma models were used to study collisionless reconnection of oppositely directed magnetic fields separated by a thin current sheet. This effort went under the rubric of Geospace Environmental Modeling (GEM) Reconnection Challenge[14]. The various models used were electron MHD[15], Hall MHD with anisotropic pressure[5], MHD and Hall MHD[30, 35, 24], full particle[32] and hybrid[20] models. It was found that the although reconnection initiates at length scales on the order of the electron skin depth the reconnection rate is governed by ion dynamics. The Two-Fluid model can describe the physics at electron skin depth scales and hence can describe collisionless reconnection correctly. On the electron-skin depth scales the field lines are no longer frozen to the electron fluid and this allows the reconnection to initiate without the need for resistivity. On the other hand in the Hall MHD model[24] the reconnection needs to be initiated by using a small resistivity.

In this section simulations are performed with the same initial conditions and parameters as used in the GEM Challenge problem. The ideal Two-Fluid model used here was not among one of those used in the original studies and hence serves as an important benchmark. The results obtained here also provide additional insight into the structure of the flow, specially after the reconnection has occurred. As is described below, complex flows, not observed in the results reported in the original studies, are obtained.

The simulation is initialized with oppositely directed magnetic fields separated by a thin current sheet. The magnetic field is given by

$$\mathbf{B}(y) = B_0 \tanh(y/\lambda)\mathbf{e}_x. \tag{3.7}$$

The initial current is carried only by the electrons:

$$\mathbf{J}_e = -\frac{B_0}{\lambda}\mathrm{sech}^2(y/\lambda). \tag{3.8}$$

The number densities of the ions and electrons are initialized as $n_e(y) = n_i(y) = n(y)$, where

$$n(y) = n_0\big(1/5 + \mathrm{sech}^2(y/\lambda)\big). \tag{3.9}$$

Finally the electron pressure is set to $p_e(y) = p(y)$ and ion pressure to $p_i(y) = 5p(y)$ where

$$p(y) = \frac{B_0}{12}n(y). \tag{3.10}$$

These initial conditions describe an equilibrium solution of the Two–Fluid equations. To initiate reconnection in a controlled manner the magnetic field is perturbed with $\delta\mathbf{B} = \mathbf{e}_z \times \nabla\psi$, where

$$\psi(x, y) = \psi_0 \cos(2\pi x/L_x)\cos(\pi y/L_y), \tag{3.11}$$

and $[-L_x/2, L_x/2] \times [-L_y/2, L_y/2]$ is the simulation domain. This form of the perturbation assures that $\nabla \cdot \mathbf{B} = 0$ at $t = 0$. Periodic boundaries are applied at $x = \pm L_x/2$ and conducting wall boundaries at $y = \pm L_y/2$. Simulations presented below are for a 512×256 grid, although coarser grids were also used. The other parameters used are $m_e/m_i = 1/25$, $L_x = 8\pi$, $L_y = 4\pi$, $B_0 = 0.1$, $\psi_0 = B_0/10$ and $\lambda = 0.5$. The unit length scale is the ion skin-depth and the unit time scale is in inverse ion cyclotron frequency. For the selected electron-ion mass ratio the electron skin depth is $1/5$ and is resolved by the grid. These parameters are identical with the GEM challenge problem.

To compare results with the models used in the GEM challenge problem the reconnected flux, ϕ, was computed using

$$\phi(t) = \frac{1}{2L_x}\int_{-L_x/2}^{L_x/2} |B_y(x, y = 0, t)|dx. \tag{3.12}$$

As the reconnection proceeds the reconnected flux, which is a measure of the net Y direction magnetic field, increases and indicates the reconnection rate. Figure 3.11 shows the reconnected flux history. It is observed that the reconnection occurs at about $t = 10$ and the reconnected flux increases rapidly after that. The computed flux history is in excellent agreement with flux histories from full particle and hybrid models used in the original GEM Challenge problem (see Fig. 3.12). From the GEM results it is also clear that the resistive Hall-MHD model also predicts the correct reconnected flux. However, in contrast to resistive Hall-MHD the Two-Fluid model presented here does not have any resistivity. The reconnection initiates due to the demagnetization of the electrons at electron skin depth scales, and thus resistivity is not required to break the field lines as in Hall-MHD. Thus, in the Two-Fluid model the magnetic field-line topology is not tied to the electron fluid as it is the in ideal Hall-MHD.

As the domain is periodic in the Y direction and there are conducting walls on the $x = \pm L_y/2$ the total energy of the system remains constant in time. Figures 3.13 and 3.14 show the history of the electromagnetic and fluid energies of the system. The initial configuration of the system is an unstable equilibrium and via the process of reconnection the magnetic field "relaxes", i.e. the electromagnetic energy stored in the magnetic field is transfered to the fluid energy. The electromagnetic energy decays rapidly after about $t = 10$ and is transfered to the fluid energy. After $t = 25$ the fluid kinetic energy decreases and is transfered to the fluid thermal energy. Even though the fluids are inviscid this conversion occurs due to adiabatic compression of the fluid. Further, the fluid undergoes shock-heating as the shock waves, visible in Figs. 3.16 and 3.17, pass through the fluid.

Fig. 3.15 shows the total energy of the system. The total energy should be conserved as the Two-Fluid system does not have any dissipation and conducting wall boundary conditions are used. However, due to numerical diffusion the total energy reduces slightly. From the figure it is clear that the loss in energy is only about 0.7%,

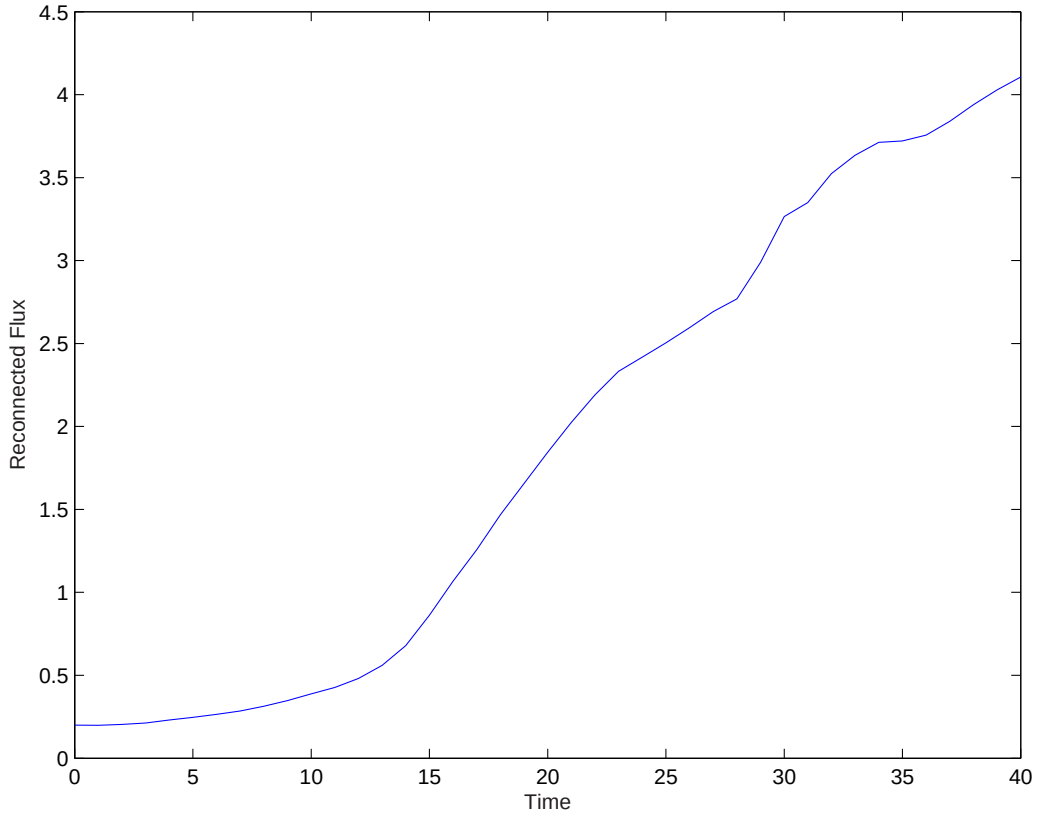

Figure 3.11: Reconnected flux verses time. The reconnected flux increases rapidly after the reconnection occurs at about $t = 10$.

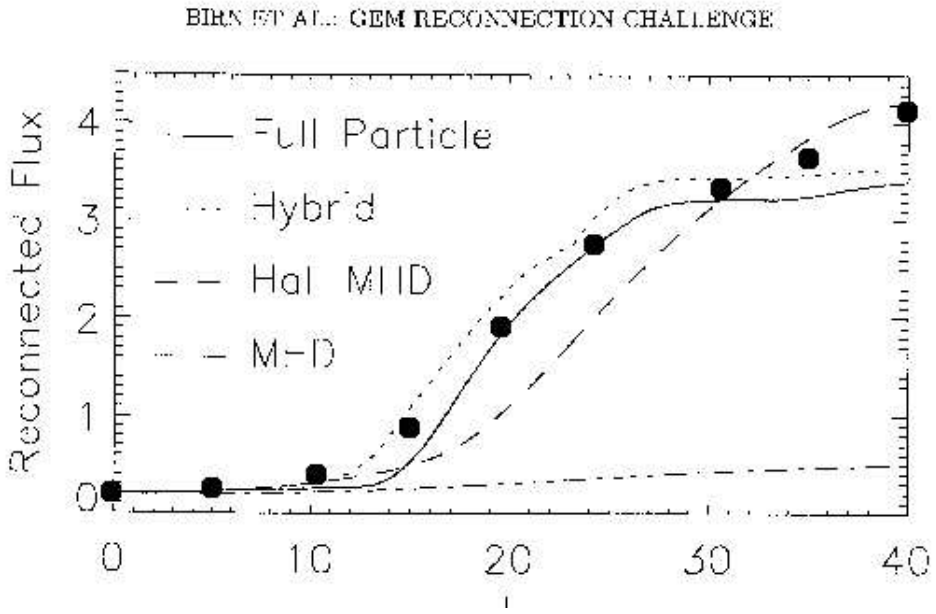

Figure 3.12: Two-Fluid reconnected flux compared to GEM results. Solid dots are results obtained using Two-Fluid model. Two-Fluid results compare well with those obtained by particle and hybrid models.

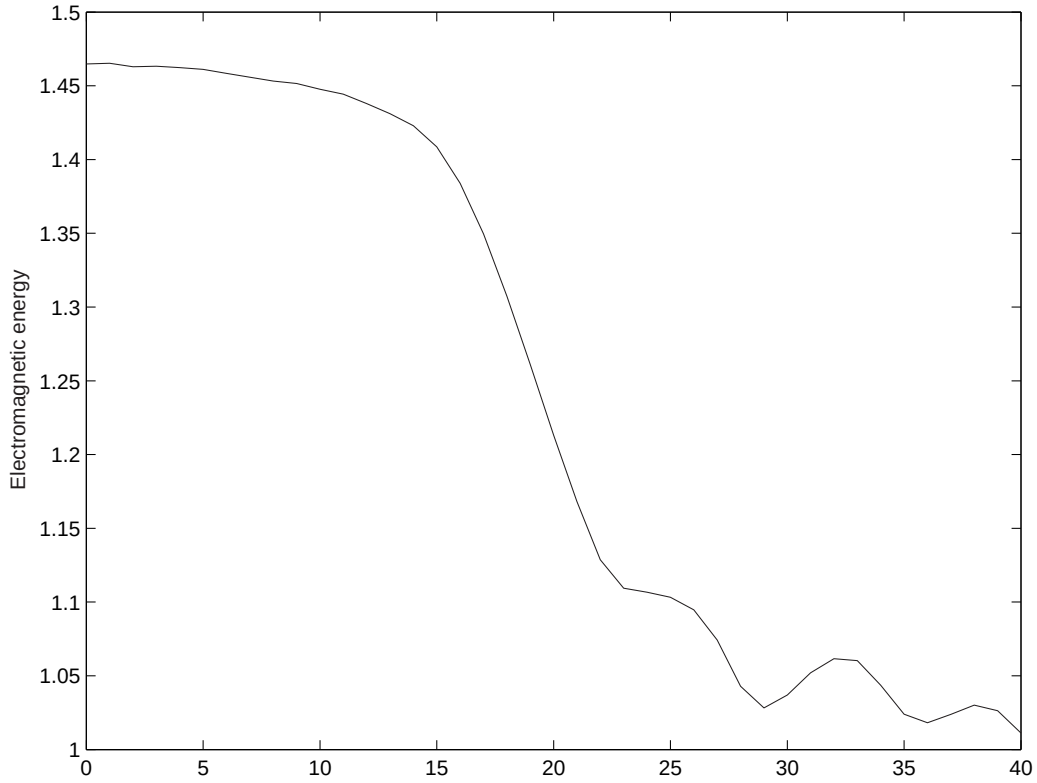

Figure 3.13: Electromagnetic energy as a function of time. After reconnection occurs the electromagnetic energy decays, the released energy being transfered to fluid thermal and kinetic energies.

showing that the scheme used here is conservative even in the presence of complex flow features.

Electron and ion momentum at $t = 25$ and $t = 40$ are shown in the gray-scale plots, Figs. 3.16 and 3.17. At $t = 25$ shocks waves traveling inwards (towards the Y axis) are observed. These shocks are formed due to the interaction of the outward flowing jets (along the X axis). At $t = 40$ complex flow structures are seen in the ion fluid. The shocks at $x \approx \pm 5.5$ are now moving outwards (away from the Y axis). The ion flow is not symmetric and this may be due to grid driven instabilities. The nature of the flow at late times seems to be governed by instabilities driven from the

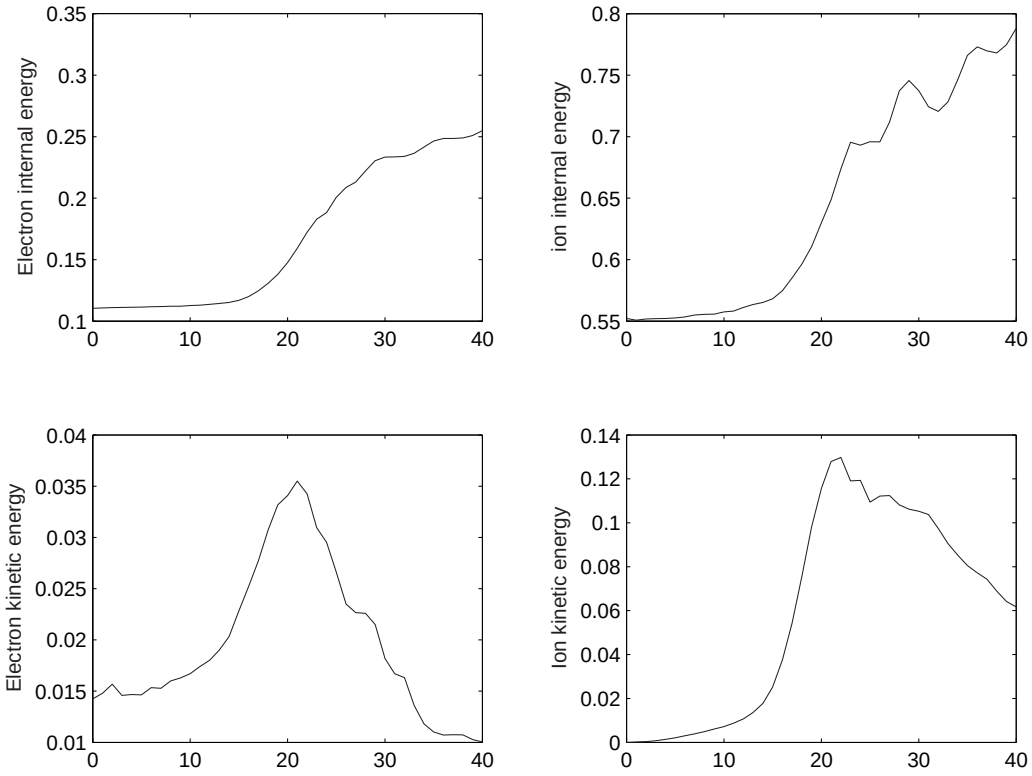

Figure 3.14: Electron thermal energy (top left), ion thermal energy (top right), electron kinetic energy (bottom left) and ion kinetic energy (bottom right). The electromagnetic energy released is transformed into kinetic and thermal energy of the fluids. After about $t = 25$ fluid kinetic energies decay as fluids become turbulent.

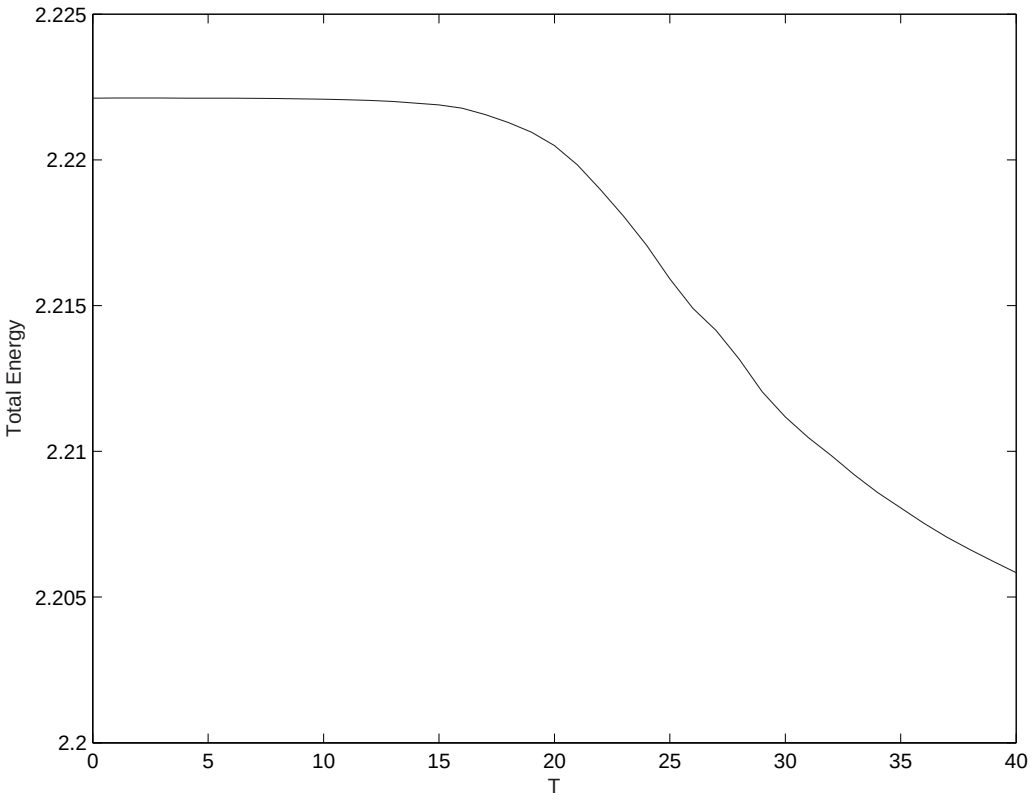

Figure 3.15: Total energy for the GEM magnetic reconnection challenge problem. The total energy should remain conserved, however, is seen to decay slightly due to numerical diffusion. The total loss in energy is 0.7% for the time period considered.

counter streaming fluid jets.

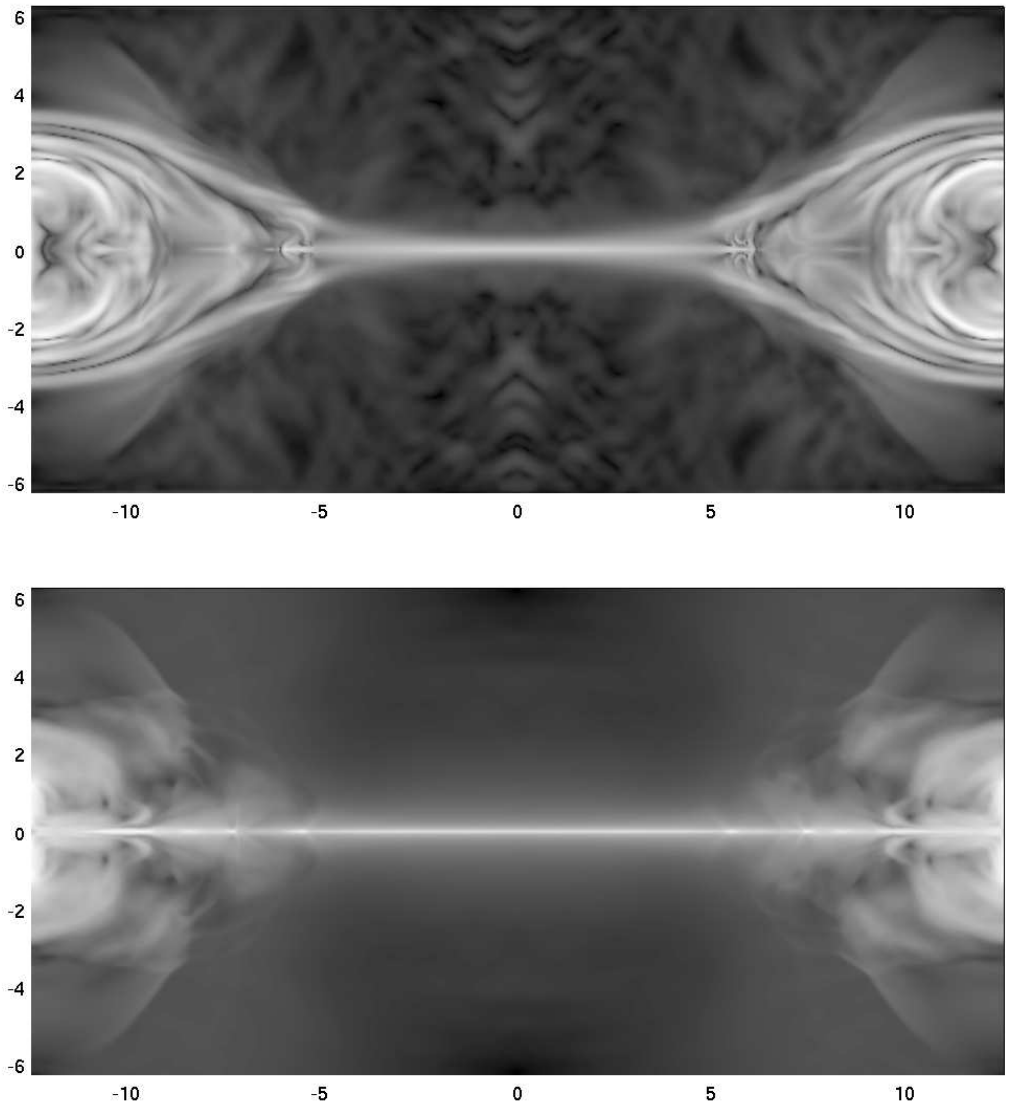

Figure 3.16: Electron momentum (top) and ion momentum (bottom) at $t = 25$. Inward traveling shock waves are visible in both the fluids. Thin jets flowing along the X axis are also visible.

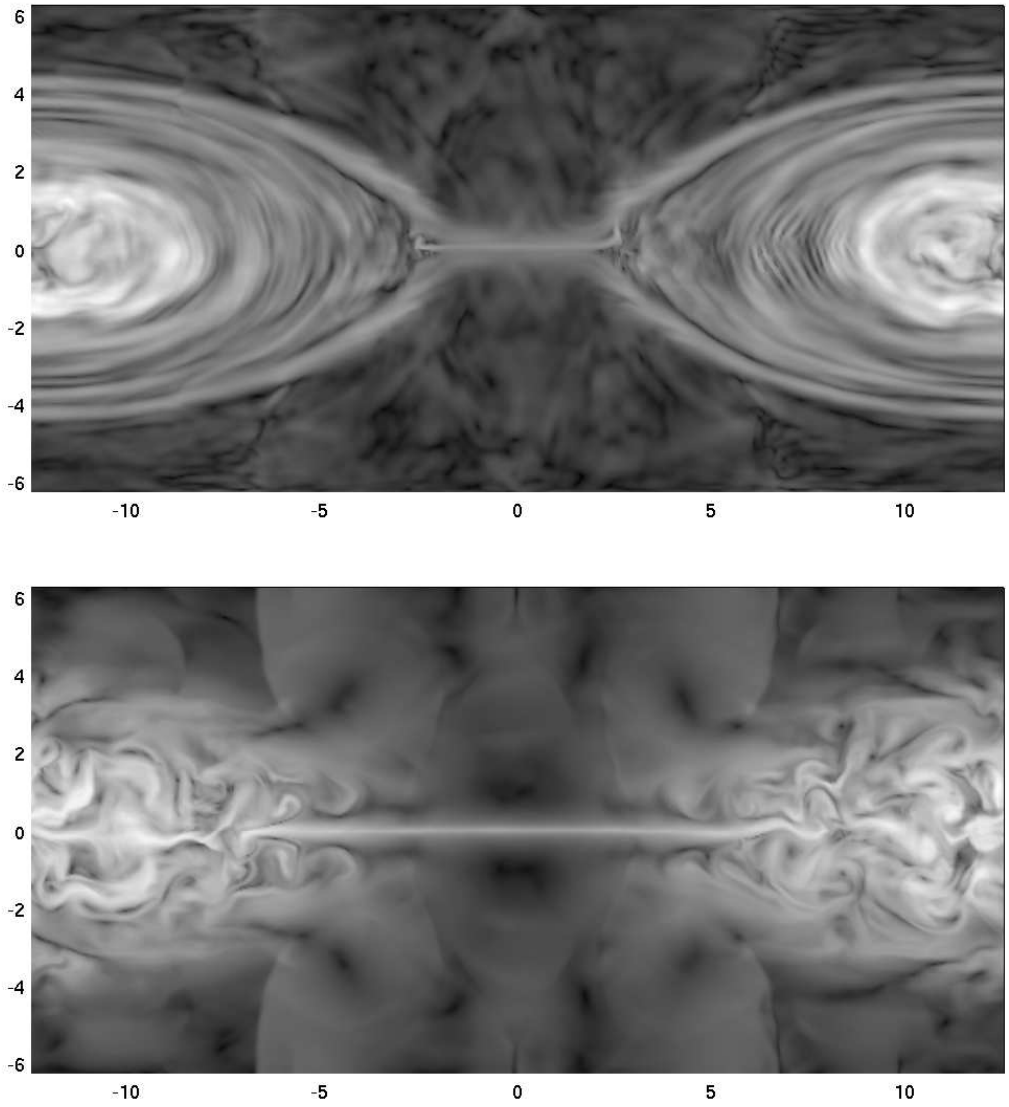

Figure 3.17: Electron momentum (top) and ion momentum (bottom) at $t = 40$. Complex flow features are visible, specially in the ion fluid. Flow structure is thought to develop due to instabilities.

Chapter 4

AXISYMMETRIC TWO-FLUID EQUILIBRIA AND FIELD REVERSED CONFIGURATIONS

4.1 Introduction

Fusion promises to be an efficient mechanism for the generation of clean energy. An objective of fusion research is the application of fusion energy in a manner acceptable to society. This concerns not only its economic benefit, but also safety and environmental issues. A number of fusion devices are currently under investigation and can be classified into two broad classes based on the device geometry. The first, and more rigorously studied and funded, is the class of toroids (donut shaped devices). ITER (`http://www.iter.org/`) is an example of a international collaboration on building a facility to produce fusion power using toroidal devices. The device is expected to produce power by 2015. The other class of fusion devices are the *compact toroids* with cylindrical geometry and are also actively under investigation for use in fusion power reactors.

The Field Reversed Configuration (FRC) and Spheromak[3] belong to the family of compact toroids. These devices do not have any internal material structures ("compact") allowing the plasma to extend to the device axis. The magnetic field topology is that of a closed donut-shaped surface ("toroidal"). Figure 4.1 shows a schematic diagram of an FRC.

Several FRC experiments are currently being carried out at the Redmond Plasma Physics Lab (RPPL) of the University of Washington [1]. For example, the star thruster experiment investigated the formation of FRCs using rotating magnetic fields. The

[1] `http://depts.washington.edu/rppl/`

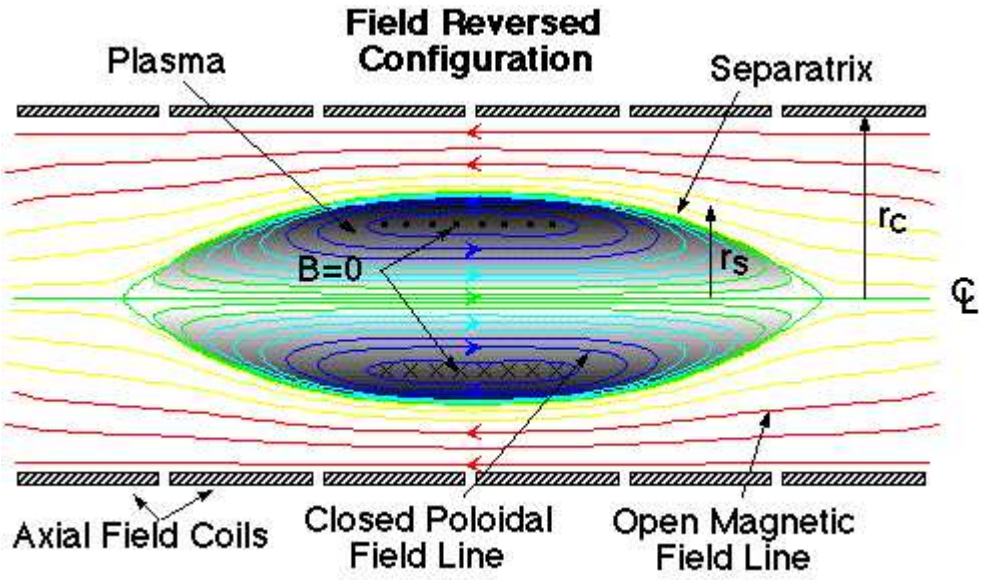

Figure 4.1: Schematic diagram of a Field Reversed Configuration. The device is cylindrical and a $r - z$ plane slice through the axis is shown.

Translation, Confinement and Sustainment (TCS) FRC experiment is being constructed to investigate, among other things, the ability to use Rotating Magnetic Fields (RMF) to both build up and sustain the flux of FRCs that have been formed in Field Reversed Theta Pinches.

It is known that Two–Fluid effects play an important role in FRC physics. Two fluid formalism to study FRC stability[16, 38, 39, 42, 43] has been extensively developed. Relaxation of Two–Fluid equlibria has also been studied[37]. However no detailed numerical studies of FRCs using the Two–Fluid model have been performed before although some results have been obtained using particle simulations[4].

In this chapter a detailed study of Field-Reversed Configuration (FRC) stability and formation is performed. The study is divided into two parts. In the first, FRC stability is studied. The needed theory for computing Two-Fluid equilibia is first developed. Simulations are initialized with various FRC equilibria and perturbed.

The growth rates are calculated and compared with MHD results. It is shown that the FRCs are indeed more stable within the Two-Fluid model than the MHD model. In the second part formation of FRCs is studied. In this set of simulations a cylindrical column of plasma is initialized with a uniform axial magnetic field. The field is reversed at the walls. Via the process of magnetic reconnection FRC formation is observed. Simulations of FRCs in the $r-\theta$ plain are performed showing the LHDI formation. It is shown that the current sheet thickens due to the instability and eventually breaks up into structures which are an ion Larmor radius thick. To understand the mechanism of the LHDI better a simple slab geometry is used to study the instability in a Harris current sheet. In these simulations it is shown that the short-wavelength LHDI is induced even thought the initial perturbation is of long wavelength.

4.2 Single Particle Motion; Canonical Momentum and Vorticity

Before developing the equilibrium equations for axisymmetric configurations it is instructive to look at single particle motion in a electromagnetic field. The Lagrangian describing this motion is

$$\mathcal{L} = \frac{1}{2}m\mathbf{u}^2 + q_s\mathbf{u}\cdot\mathbf{A} - q\varphi \tag{4.1}$$

where $\mathbf{u}$ is the particle velocity, m and q are particle mass and charge, $\mathbf{A}$ is the vector potential and φ is the electric potential. In terms of the potentials the magnetic and electric fields are given by

$$\mathbf{E} = -\boldsymbol{\nabla}\phi + \partial\mathbf{A}/\partial t, \tag{4.2}$$

$$\mathbf{B} = \boldsymbol{\nabla}\times\mathbf{A}. \tag{4.3}$$

From the Lagrangian the canonical mometa is computed as

$$\mathbf{p} = \frac{\partial\mathbf{v}}{\partial\mathcal{L}} = m\mathbf{u} + q\mathbf{A} \tag{4.4}$$

From this it is clear that the canonical momentum for particle motion is not the same as the linear momentum but is modified by the magnetic field vector potential. However, for vanishing particle mass the canonical momentum and the linear momentum coincide.

In cylindrical coordinates $\mathbf{u} = \dot{r}^2 + r^2\dot{\theta} + \dot{z}$, where (r, θ, z) are cylindrical coordinates. Thus for axisymmetric systems the azimuthal component of the canonical momentum, p_θ is conserved. Thus, in canonical momentum space particles move on surfaces of $p_\theta =$ constant. Such surfaces are called as *drift-surfaces* and are important in axisymmetric equilibrium configurations studied below.

4.3 Axisymmetric Two-Fluid Equilibrium

To come...

4.4 LHDI in cylindrical plasma Configurations

Field Reversed Configuration (FRC) is a plasma fusion device where the magnetic field is used to confine the plasma until fusion temperatures are reached and fusion initiates. In this section FRC simulations are performed in the $r - \theta$ plane showing the formation of the Lower-Hybrid Drift Instability (LHDI) in FRCs. The Two-Fluid simulation performed in this section are for elongated FRCs in which $\partial/\partial z \equiv 0$. The initial conditions were computed from the Two-Fluid equilibrium equations obtained by setting $\partial/\partial\theta \equiv 0$, $u_r = 0$, which, for stationary ions, are written as

$$-mn\frac{u_\theta^2}{r} = -\frac{\partial p}{\partial r} - enu_\theta B_z \tag{4.5}$$

$$\frac{\partial B_z}{\partial r} = e\mu_0 mnu_\theta. \tag{4.6}$$

Here u_θ is the electron azimuthal velocity, B_z is the magnetic field in the Z-direction, p is the pressure and $-e$ is the electron charge. For an FRC, from Fig. (4.1) it is clear that the magnetic field $B_z(r)$ changes sign across the domain. A number of "reversed field" magnetic profiles were selected. The electron current needed to support this

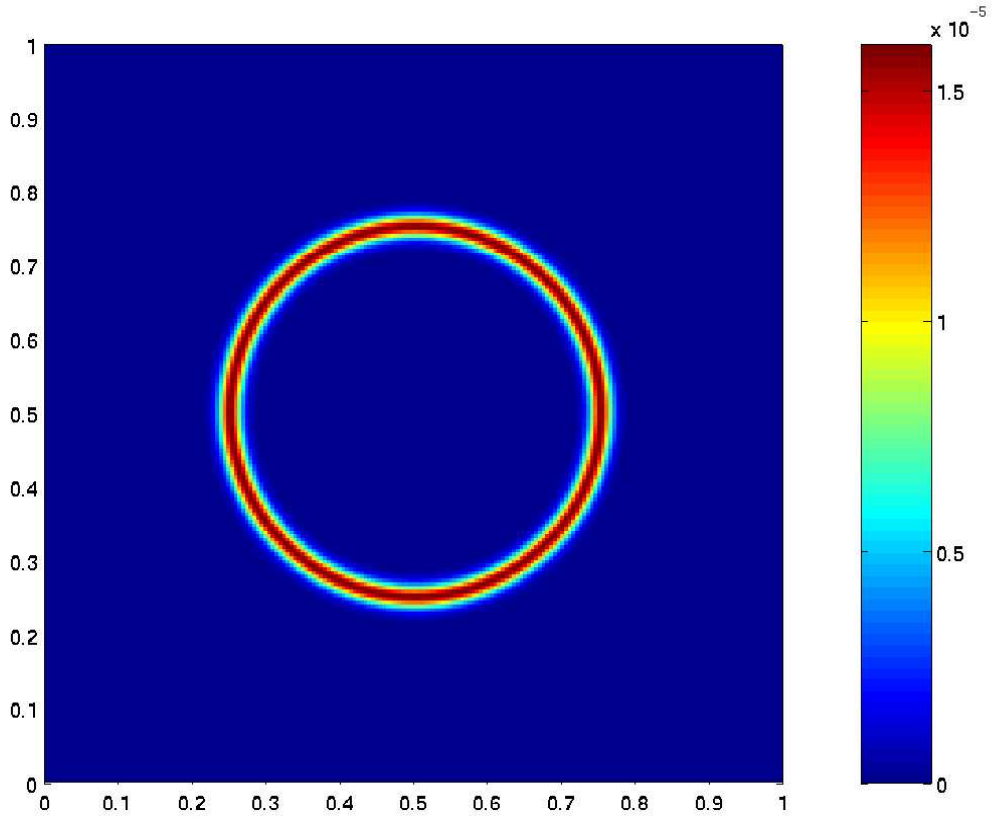

Figure 4.2: Electron momentum in the $r-\theta$ plane for a field reversed pinch. The electrons have an azimuthal velocity which support an out-of-plane magnetic field B_z.

field were computed from Eq. (4.6). Once u_θ was determined the pressure profile was determined from Eq. (4.5). Figure (4.2) shows the total electron momentum for one such magnetic field profile. The various simulation were performed by varing the magnetic field profile so as to control the thickness of the current sheet needed to support the field. An initial $m = 1$ mode perturbation was applied to the electron momentum and the simulation was run to $t = 20$. This initial perturbation corresponds to a long-wavelength (on the order of the current sheet length) perturbation. Time in these simulations was measured in light transit times across the domain.

Figure (4.3) shows the electron momentum at $t = 10$, for the current profile in

Fig. (4.2). It is clear that the current sheet has broken up into smaller structures, each about an ion Lamor radius long. These smaller structures have a much shorter wavelength than the applied perturbation thus showing that the short-wavelength instability is more unstable than the long wavelength one.

Figure (4.4) shows the electron momentum at $t = 10$, for a thinner current profile than in Fig. (4.2). With this current profile the sheet breaks up into finer structures. It is also seen that the sheet has become thicker, which is a typical signature of anomalous resistivity. Figure (4.5) shows the electron momentum at $t = 20$. The current sheet has become thicker and the small scale instability has spread outwards towards the pinch walls.

Figure (4.6) shows the electron momentum at $t = 10$, for thinner current profile. The magnetic field changes very rapidly across the sheet and has an almost shock-like structure. With this current profile the sheet breaks up into finer structures and shows an fine-scale plasma turbulence.

4.5 LHDI in planar plasma Configurations

To understand the mechanism of the LHDI better simulations were also performed in planar current sheet geometry. A Harris current sheet equilibrium was selected. The electron and ion number densities were set to $n_e = n_i = n(x)$ where

$$n(x) = n_0 \mathrm{sech}^2(y/L) \tag{4.7}$$

where L is the half-width of the current sheet. The magnetic field was initialized by

$$\mathbf{B}(y) = \hat{\mathbf{z}} B_0 \tanh(y/L), \tag{4.8}$$

where $\hat{z}$ is a unit vector in the Z-direction. The electron and ion velocities were set to $\mathbf{v}_i = \hat{x} v_i$ and $\mathbf{v}_e = \hat{x} v_e$ where v_i and v_e are constants and $\hat{x}$ is the unit vector in the X-direction. The initial equilibrium values were perturbed using a perturbation with wavelength given by the domain lenght.

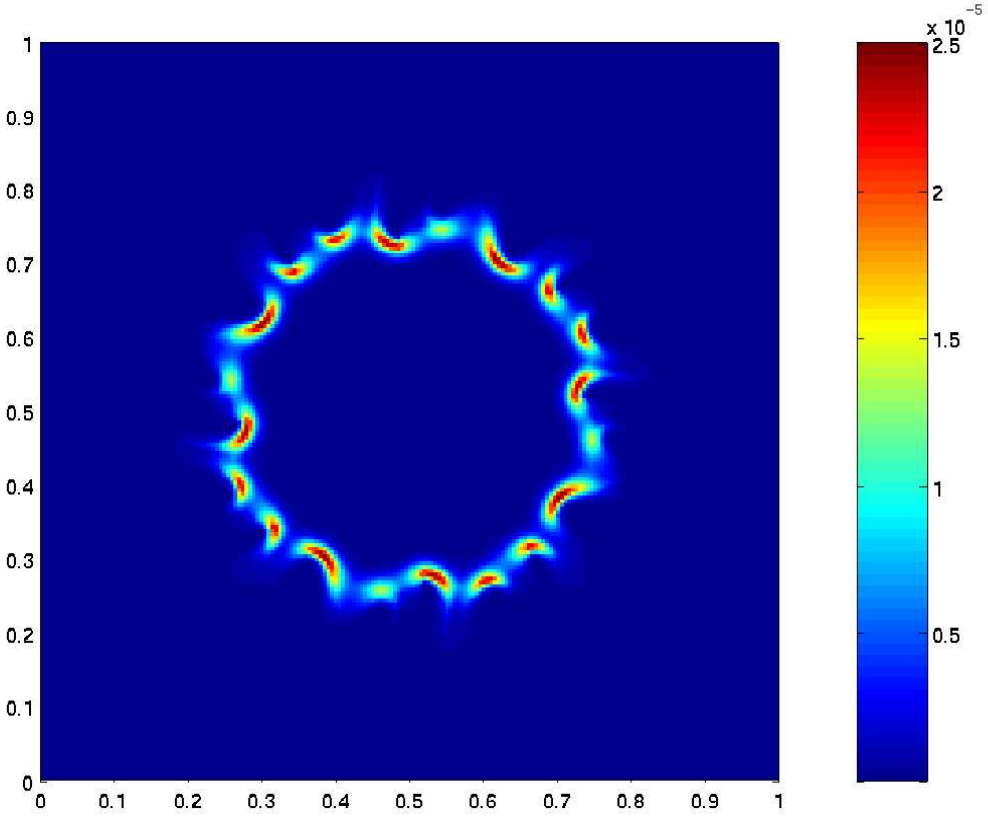

Figure 4.3: Electron momentum in the $r-\theta$ plane for a field reversed pinch at $t = 10$. The current sheet has broken up into smaller structures, each of which is about an ion Lamor radius long.

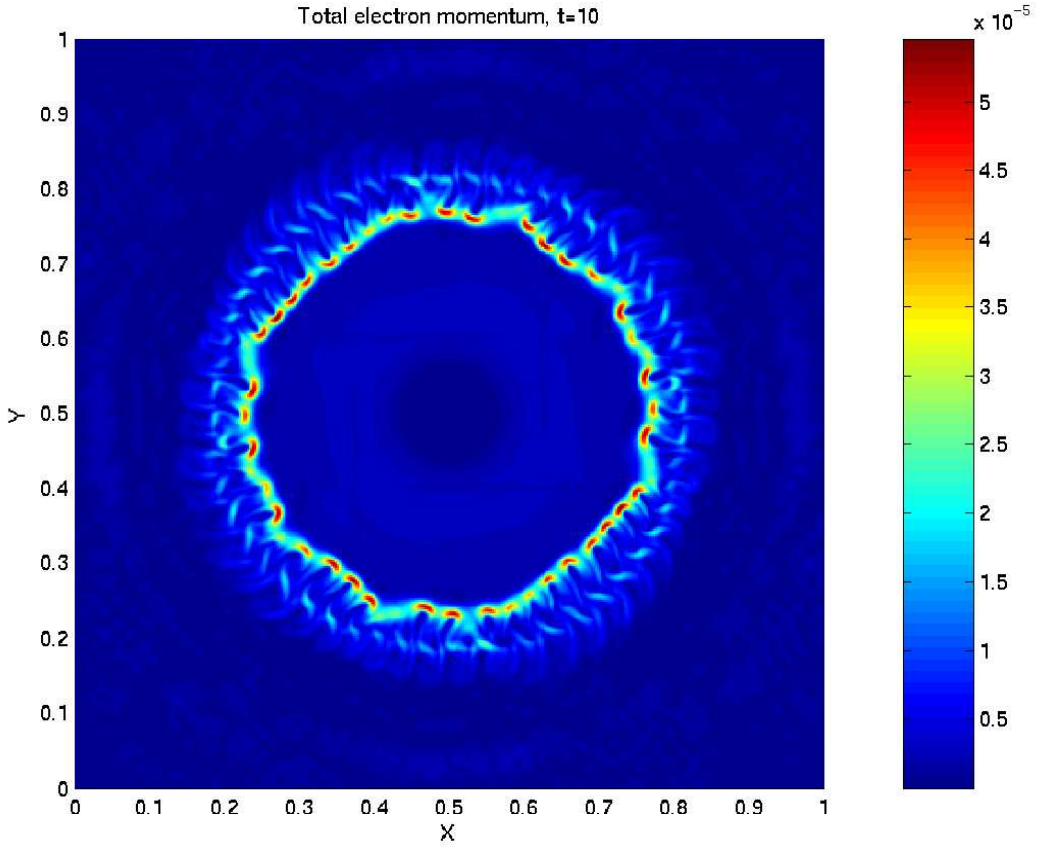

Figure 4.4: Electron momentum in the $r-\theta$ plane for a field reversed pinch at $t = 10$. The current sheet is thinner than in the previous simulations and is seen to break up into larger number of pieces.

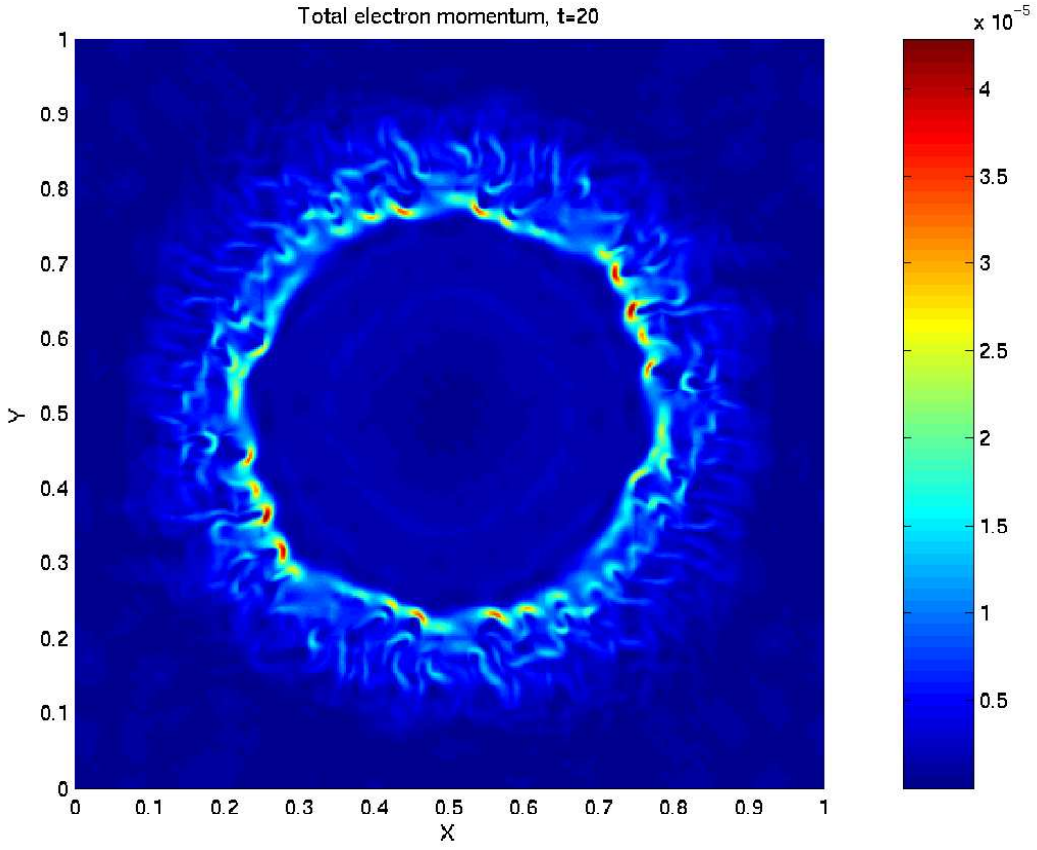

Figure 4.5: Electron momentum in the $r - \theta$ plane for a field reversed pinch at $t = 20$. The current sheet has now completely diffused away, and shows many fine scale features in the electron flow. pieces.

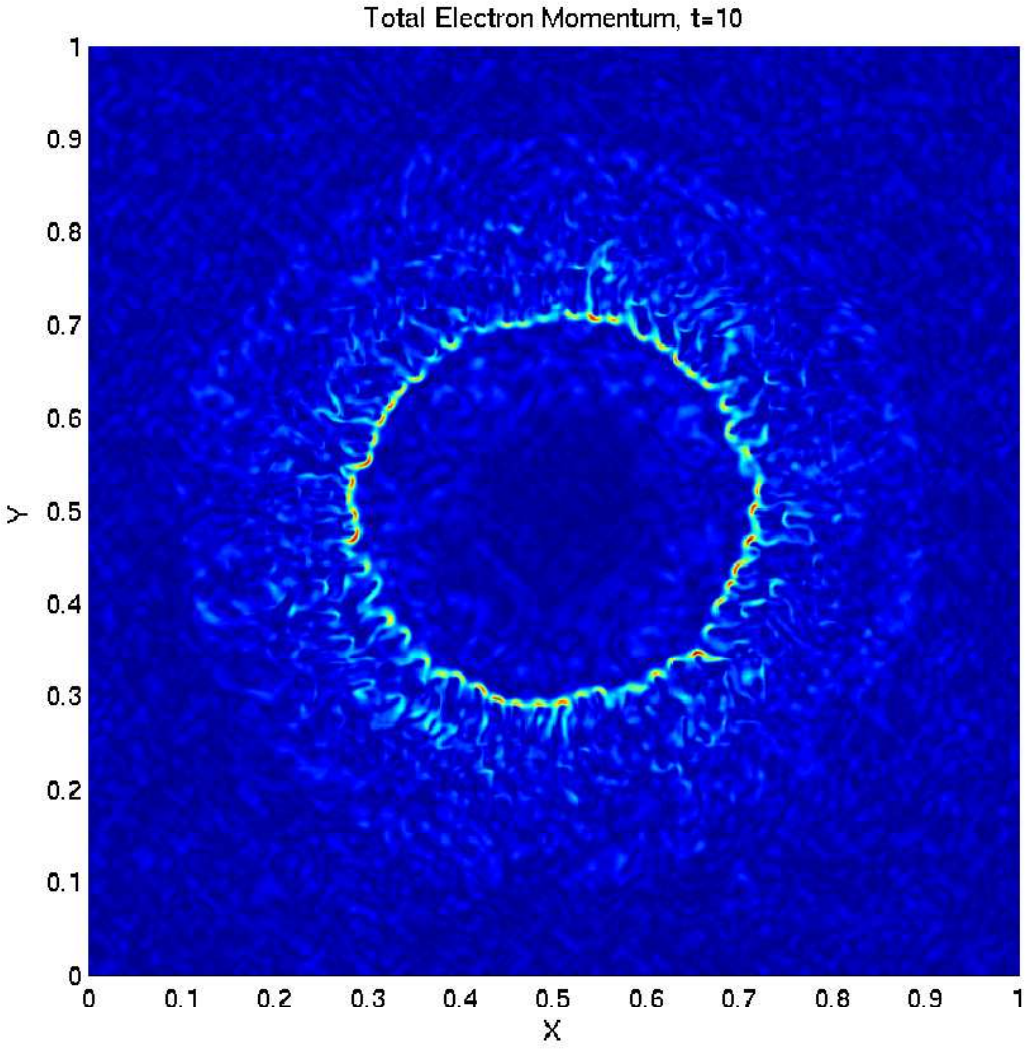

Figure 4.6: Electron momentum in the $r-\theta$ plane for a field reversed pinch at $t = 10$. The magnetic field profile for this simulation is very sharp, almost shock-like. The sheet has broken up into small scale structures and the fluid shows an almost turbulent flow.

The current sheet is neutrally stable to the long wavelength perturbation applied. As the simulation progresses the sheet simply oscillates about its equilibrium position and appears to "slosh" inside the domain. Figure (4.7) shows the electron momentum at $t = 100$. The initial perturbation has kinked the sheet, though the kink does not grow. Figure (4.8) shows the electron density at $t = 200$. It is now seen that small structures are forming at the edge of the current sheet. These structures are each about 1 Lamor radius wide. These structures are a typical signature of the onset of the LHDI which starts at the location where the density gradient is maximum. Figure (4.9) shows the electric fields at the same time ($t = 200$). The structure of the electric fields in this figure is typically seen in hybrid simulations and typically indicates the onset of the LHDI.

After $t = 200$ the LHDI instability grows very rapidly, and the "finger" like structures elongated ultimately breaking up the sheet. Figure () shows the electron density at $t = 250$ just as the sheet is about to break up. Two separate perturbations are clearly seen in this figure. The long-wavelength applied kink-mode perturbation is still clearly visible while the short wavelength LHDI has now almost saturated the flow. This figure dramatically illustrates that the although the sheet is stable to the long-wavelength perturbations it is unstable to the shorter wavelength LHDI.

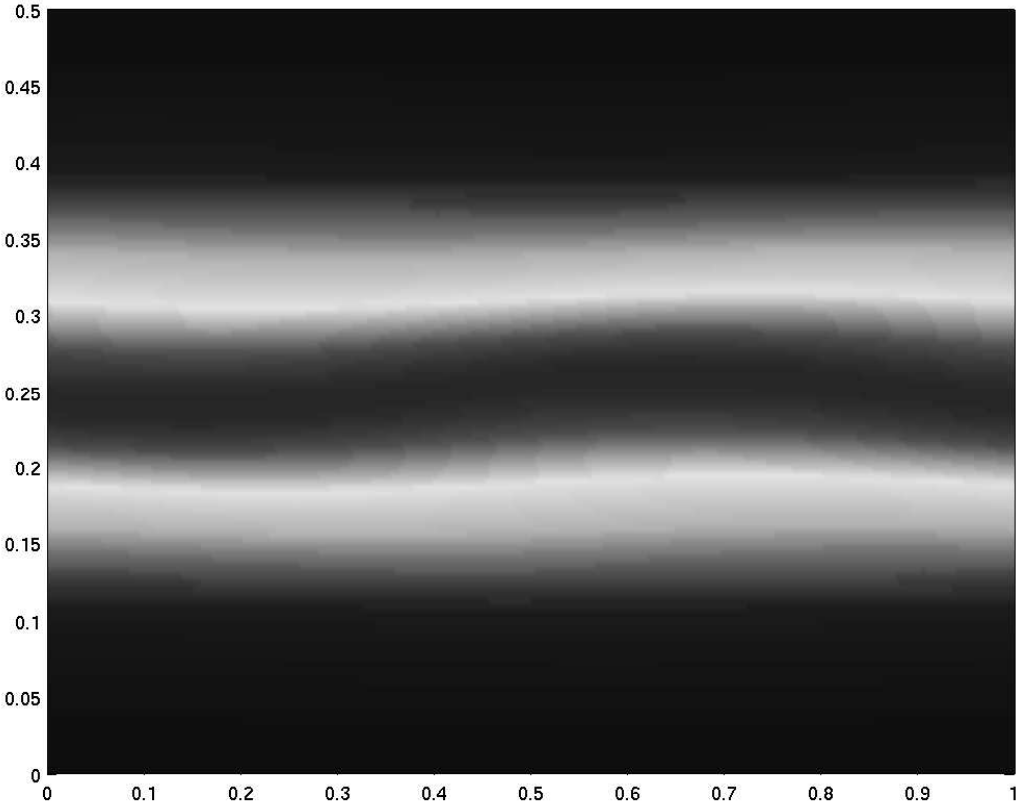

Figure 4.7: Electron Density at t=100 for a Harris current sheet kink mode. The sheet is neutrally stable to the applied initial long-wavelength perturbation and simply oscillates about its initial position.

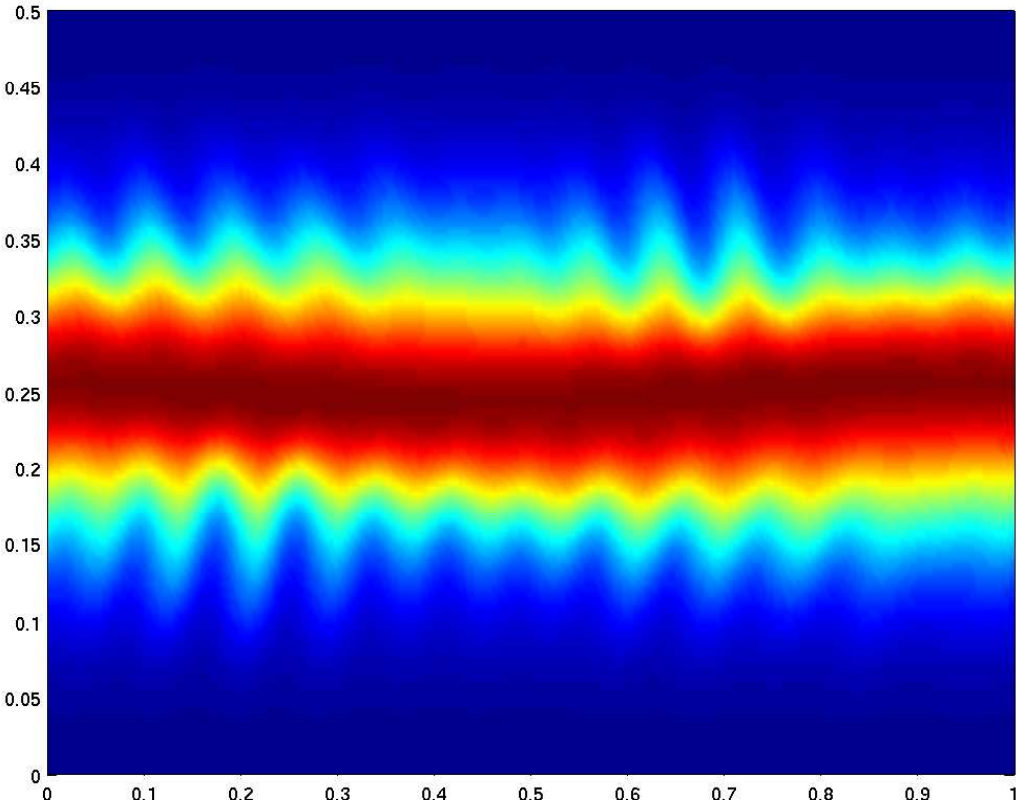

Figure 4.8: Electron Density at t=100 for a Harris current sheet kink mode. The Lower-Hybrid drift instability has just started to form at the edge of the current sheet and is visible as small bumps about a Lamor radius thick. The instability grows rapidly after this point soon breaking up the sheet completely.

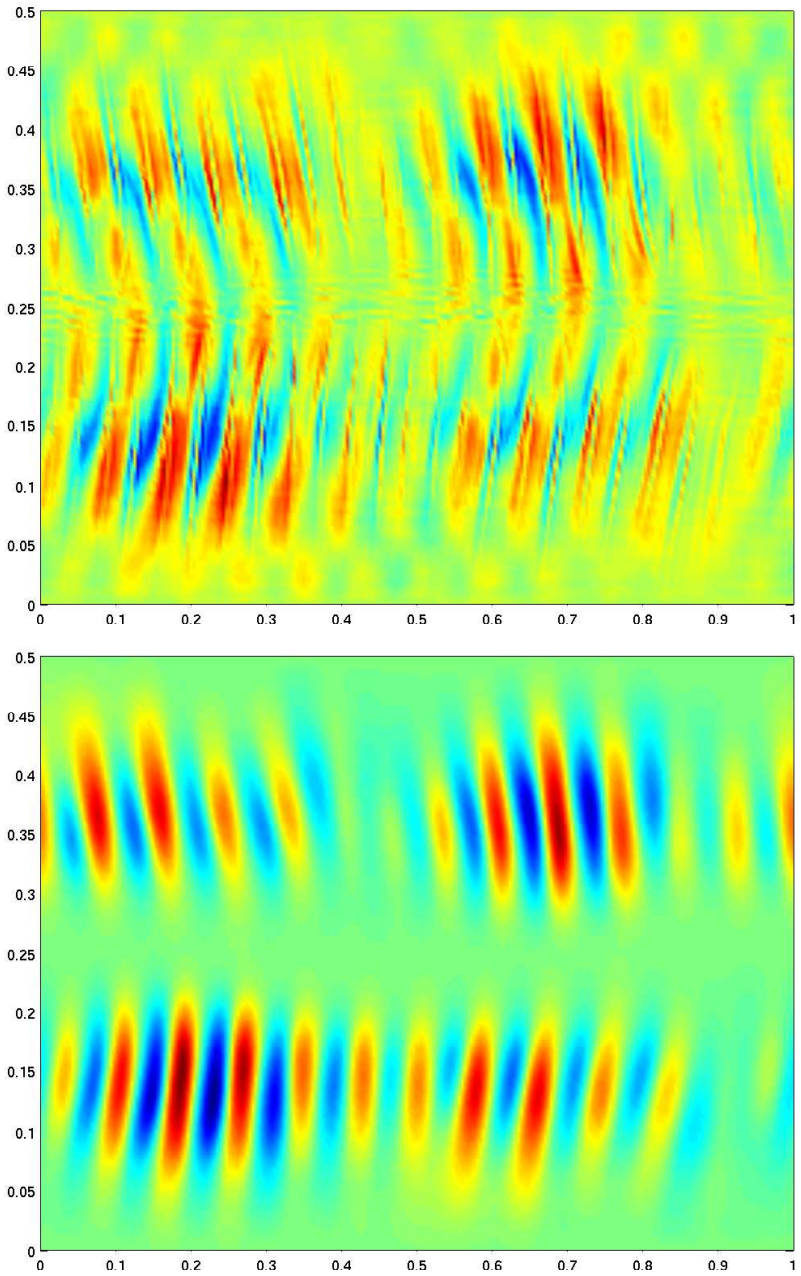

Figure 4.9: Out-of plane electric field E_z (upper panel) and in-plane electric field E_x at t=200. The structure of the electric fields seen is a signature of the LHDI in the sheet.

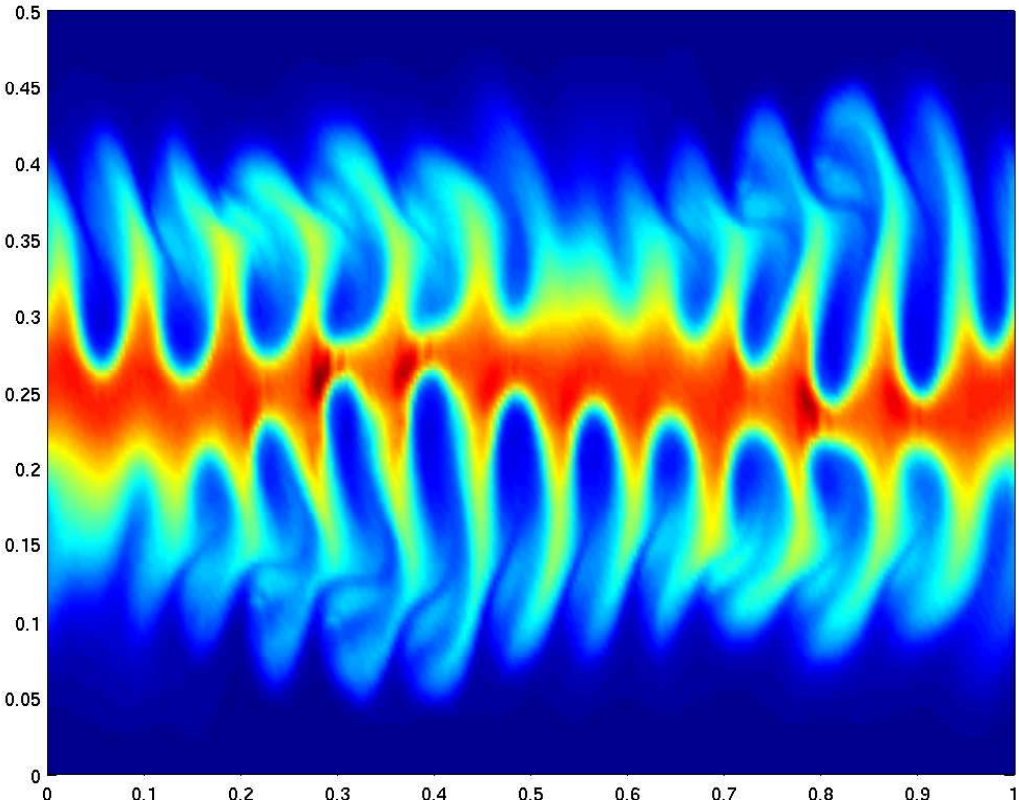

Figure 4.10: Electron Density at t=250 for a Harris current sheet kink mode. The Lower-Hybrid drift has now completely set in and the sheet has broken up into thin structures. A secondary Kelvin Helmholtz instability is also visible as there is a significant velocity shear at the edge of the instability.

Chapter 5
CONCLUSIONS

A high resolution wave propagation scheme for ideal Two-Fluid Plasma equations is developed. The algorithm presented here can be successfully used to in multiple dimensions. The algorithm can also be extended to general quadrilateral geometries easily. An important aspect of this work was to highlight Two-Fluid physics which is not included in the commonly used Magnetohydrodynamics (MHD) and Hall MHD models. The three applications presented here each show the importance of Two-Fluid physics. In the one dimensional Riemann problem it was shown that a smooth transition from neutral ideal fluid shocks to MHD shocks can be obtained. The ion-acoustic soliton propagation showed the importance of charge separation. In fact, the dispersive effects due to charge separation balance the tendency of the fluid to shock and hence lead to soliton propagation. In both MHD as well as Hall MHD ion-acoustic solitons can not be supported as quasi-neutrality ($n_e = n_i$) is assumed. The Geospace Environmental Modeling (GEM) Reconnection Challenge problem showed that the Two-Fluid model can correctly explain fast reconnection observed in collisionless plasmas. In other fluid models of reconnection some mechanism (like resistivity in Hall MHD) needs to be incorporated to initiate the reconnection. Complex flows, possibly turbulent, can be seen late after the reconnection has occurred. The algorithm presented here can also be applied directly to higher–moment fluid approximation to collisionless plasmas. For example, the next two set of collisionless fluid equations contain, for s species plasma, $10s$ and $20s$ fluid equations. These higher–moment equations incorporate anisotropic pressure and heat tensor effects and hence extend the usefulness of fluid plasma models.

Non-ideal effects like resistivity and radiation can also be added to the basic algorithm presented here. In this case the equation system is no longer hyperbolic but has parabolic parts from the non-ideal terms. Although the High-Resolution Wave-Propagation scheme is designed for hyperbolic equations these non-ideal terms can be incorporated as source terms, which now contain second or higher-order derivatives. Such an approach has been discussed by LeVeque[22] for the diffusive Burgers equation. Including non-ideal terms will also effect the results presented here. For example, it is known that gyroviscous stress-tensor can anisotropically heat the ions near the reconnection point during magnetic reconnection. However, this should not change the reconnected flux significantly. The focus of this thesis being the ideal full Two-Fluid model we have ignored all non-ideal effects for the results presented.

A detailed study of Lower-Hybrid Instability (LHDI) in Field-Reversed Configurations (FRCs) is performed. The strong azimuthal electron flow in the FRC causes LHDI, which can be captured if the ion-gyroradius is well resolved. The LHDI is known to be a possible source of anomalous resistivity in many plasma configurations. The study is concluded with a analysis of the LHDI in the simpler Harris current sheet configuration. It is seen that the short wavelength LHDI sets in late but then grows very rapidly, soon destroying the confinement of the plasma.

A primary contribution of this thesis was to develop the first fully nonlinear solver for the full Two-Fluid plasma equations. In the plasma sciences community the importance of Two-Fluid effects has long been recognized, but the community has not yet developed the numerical tools to study such effects. One main reason is the vast variety of physics described by this model, which, moreover, occurs on widely separated time and space scales. Also, the traditional approach in plasma fluid models has been to start with the MHD equations and then add more physics to it. The approach in this thesis was the reverse. The full Two-Fluid equations do not make any assumptions about displacement currents, electron inertia or charge neutrality. This way the basic model is described by familiar ideal fluid equations and Maxwell

equations of electromagnetism. Standard schemes developed for hyperbolic equations can thus be applied to this model, thus creating a tool to solve many fascinating plasma physics problems which were hitherto not available from other plasma fluid models. The magnetic reconnection is one such problem as is the Lower-Hybrid Drift Instability. Both these physically phenomena are difficult to simulate using MHD or Hall MHD without the addition of some artificial ad-hoc resistivity. In the Two-Fluid model, on the other hand, these problems become easy to solve, as shown in the previous chapters. Our ongoing research will focus on applying the Two-Fluid model and its generalization to fusion devices, plasma accelerators and FRC thrusters.

BIBLIOGRAPHY

[1] S. Baboolal. Finite-difference modeling of solitons induced by a density hump in a plasma multi–fluid. *Mathematics and Computers in Simulation*, 55:309–316, 2001.

[2] D. Bale, R. J. LeVeque, S. Mitran, and J. A. Rossmanith. A wave-propagation method for conservation laws and balance laws with spatially varying flux functions. *SIAM Journal of Scientific Computing*, 24:955–978, 2002.

[3] Paul M. Bellan. *Spheromaks*. Imperial College Press, 2000.

[4] Elena V. Belova, Ronald C. Davidson, Hantao Ji, and Masaaki Yamada. Kinetic effect on the stability properties of field-reversed configurations. i. linear stability. *Physics of Plasmas*, 2003.

[5] Joachim Birn and Michael Hesse. Geospace environment modeling (gem) magnetic reconnection challenge: Resistive tearing, anisotropic pressure and hall effects. *Journal of Geophysical Research*, 106(A3):3737, 2001.

[6] M. Brio and C.C. Wu. An upwind differencing scheme for the equations of ideal magnetohydrodynamics. *Journal of Computational Physic*, 75:400–422, 1988.

[7] J. Büchner, C.T. Dunn, and M. Scholer, editors. *Space Plasma Simulations*. Springer, 2003.

[8] F. Califano, T. Cecchi, and C. Chiuderi. Nonlinear kinetic regime if the Weibel instability in an electron–ion plasma. *Physics of Plasmas*, 2002.

[9] F. Califano, F. Pegoraro, and S.V. Bulanov. Spatial structure and time evolution of the Weibel instability in collisionless inhomogeneous plasmas. *Physical Review E*, 1997.

[10] F. Califano, F. Pegoraro, S.V. Bulanov, and A. Mangeney. Kinetic saturation of the Weibel instability in a collisionless plasma. *Physical Review E*, 57(6):7048–7059, 1998.

[11] D.B. Cohn and K.R. McKenzie. Density-step-excited ion-acoustic solitons. *Physical Review Letters*, 30:258–261, 1973.

[12] Ronald C. Davidson. *Methods in Nonlinear Plasma Theory.* Academic Press, 1972.

[13] James J. Duderstadt and William R. Martin. *Transport Theory.* John Wiley and Sons, 1979.

[14] J. Birn et al. Geospace environmental modeling (GEM) magnetic reconnection challenge. *Journal of Geophysical Research*, 106:3715, 2001.

[15] Michael Hesse, Joachim Birn, and Masaha Kuznetsova. Collisionless magnetic reconnection: Electron processes and transport modeling. *Journal of Geophysical Research*, 106(A3):3721, 2001.

[16] A. Ishida, H Momota, and L.C. Steinhauer. Variational formulation for a multifluid flowing plasma with application to internal tilt mode of a field-reversed configuration. *Physics of Fluid*, 31(10):3024–3034, 1988.

[17] Akira Ishimaru. *Electromagnetic Wave Propagation, Radiation and Scattering.* Prentice Hall, 1991.

[18] Bo-Nan Jiang, Jie Wu, and L.A. Povinelli. The origin of spurious solutions in computational electromagnetics. *Journal of Computational Physics*, 125:104–123, 1996.

[19] Andrei G. Kulikoviskii, Nikolai V. Pogorelov, and Andrei Yu. Semenov. *Mathematical Aspects of Numerical Solutions of Hyperbolic Systems.* Chapman and Hall/CRC, 2001.

[20] Masha M. Kuznetsova, Michael Hesse, and Dan Winske. Collisionless reconnection supported by nongyrotropic pressure effects in hybrid and particle simulations. *Journal of Geophysical Research*, 106(A3):3799, 2001.

[21] Jan Olav Langseth and R.J. LeVeque. A wave propagation method for three-dimensional hyperbolic conservation laws. *Journal of Computational Physics*, 165:126–166, 2000.

[22] Randall J. LeVeque. *Finite Volume Methods For Hyperbolic Problems.* Cambridge University Press, 2002.

[23] J. Loverich, A. Hakim, and U. Shumlak. A Discontinous Galerkin Method for Ideal Two-Fluid Plasma Equations. *Journal of Computational Physics (submitted)*, 2005. Submitted.

[24] Z.W. Ma and A. Bhattacharjee. Hall magnetohydrodynamic reconnection: The geospace environment modeling challenge. *Journal of Geophysical Research*, 2001.

[25] J.F. McKenzie and T.B. Doyle. Oblique solitons in a cold magnetized plasma. *Physics of Plasmas*, 2001.

[26] J.F. McKenzie and T.B. Doyle. The properties of fast and slow oblique solitons in a magnetized plasma. *Physics of Plasmas*, 2001.

[27] C.-D Munz, P. Omnes, and R. Schneider. A three-dimensional finite-volume solver for the Maxwell equations with divergence cleaning on unstructured meshes. *Computer Physics Communications*, 2000.

[28] C.-D Munz, P. Omnes, R. Schneider, E. Sonnendrüker, and U. Voß. Divergence correction techniques for Maxwell solvers based n a hyperbolic model. *Journal of Computational Physics*, 161:484–511, 2000.

[29] C.-D Munz and U. Voß. A finite-volume method for the Maxwell equations in the time domain. *SIAM Journal of Scientific Computing*, 22(2):449–475, 2000.

[30] A. Otto. Geospace environment modeling (gem) magnetic reconnection challenge: Mhd and hall mhd - constant and current dependent resistivity models. *Journal of Geophysical Research*, 2001.

[31] F. Pegoraro, S.V. Bulanov, F. Califano, and M. Lotano. Nonlinear development of the Weibel instability and magnetic field generation in a collisionless plasma. *Physica Scripta*, T63:262–265, 1996.

[32] P.L. Prichette. Geospace environment modeling magnetic reconnection challenge: Simulations with a full particle electromagnetic code. *Journal of Geophysical Research*, 106(A3):3783, 2001.

[33] Eric Priest and Terry Forbes. *Magnetic Reconnection*. Cambridge University Press, 2000.

[34] P.L. Roe. Approximate riemann solvers, parameter vectors, and difference schemes. *Journal of Computational Physics*, 43:357–372, 1981.

[35] M.A. Shay, J.F. Drake, B.N. Rogers, and R.E. Denton. Alfvénic collisionless magnetic reconnection and the hall term. *Journal of Geophysical Research*, 2001.

[36] U. Shumlak and J. Loverich. Approximate Riemann Solver for the Two Fluid Plasma Model. *Journal of Computational Physics*, 187:620–638, 2003.

[37] L.C. Steinhauer and A.Ishida. Relaxation of two-species magnetofluid and application to finite-β flowing plasma. *Physics of Plasmas*, 5(7):2609–2622, 1998.

[38] Loren C. Steinhauer. Formalism for multi-fluid equilibria with flow. *Physics of Plasmas*, 6(7):2734–2741, 1999.

[39] Loren C. Steinhauer, Hideaki Yamada, and Akio Ishida. Two-fluid flowing equilibria of compact plasmas. *Physics of Plasmas*, 2001.

[40] E.W. Weibel. Spontaneously growing transverse waves in a plasma due to an anisotropic velocity distribution. *Physical Review Letters*, 2:83, 1959.

[41] L.C. Woods. *Physics of Plasmas*. Wiley-VCH, 2004.

[42] Hideaki Yamada and Takayuki Katano. Stability formalism of a flowing two-fluid plasma. *Physics of Plasmas*, 10(4):1168–1171, 2003.

[43] Hideaki Yamada, Takayuki Katano, and Kazumi Kanai. Equilibrium analysis of a flowing two-fluid plasma. *Physics of Plasmas*, 2002.

Appendix A

THE TEN-MOMENT PLASMA EQUATIONS

The Ten-Moment equations are obtained by taking moments of the Vlasov equations and retaining only the equations for number density, momentum and the pressure tensor. In tensor notation they are listed below.

$$\frac{\partial n}{\partial t} + \frac{\partial}{\partial x_j}(nu_j) = 0 \tag{A.1}$$

$$m\frac{\partial}{\partial t}(nu_i) + \frac{\partial \mathcal{P}_{ij}}{\partial x_j} = nq(E_i + \epsilon_{ijk}u_j B_k) \tag{A.2}$$

$$\frac{\partial \mathcal{P}_{ij}}{\partial t} + \frac{\partial}{\partial x_k}(u_{[i}\mathcal{P}_{jk]} - 2nmu_i u_j u_k) = nqu_{[i}E_{j]} + \frac{q}{m}\epsilon_{[ikl}\mathcal{P}_{kj]}B_l \tag{A.3}$$

In deriving these we have set $Q_{ijk,k} = 0$ in Eq. (1.25). In one dimension, in Cartesian coordinates identifying the subscripts $(1, 2, 3) \equiv (x, y, z)$, these equations can be put into the conservation law form where the conserved variables and fluxes are

$$\mathbf{q} = \begin{pmatrix} \rho \\ \rho u \\ \rho v \\ \rho w \\ \rho u^2 + P_{xx} \\ \rho uv + P_{xy} \\ \rho uw + P_{xz} \\ \rho v^2 + P_{yy} \\ \rho vw + P_{yz} \\ \rho w^2 + P_{zz} \end{pmatrix}, \quad \mathbf{f} = \begin{pmatrix} \rho u \\ \rho u^2 + P_{xx} \\ \rho uv + P_{xy} \\ \rho uw + P_{xz} \\ \rho u^3 + 3uP_{xx} \\ \rho u^2 v + 2uP_{xy} + vP_{xx} \\ \rho u^2 w + 2uP_{xz} + wP_{xx} \\ \rho uv^2 + uP_{yy} + 2vP_{xy} \\ \rho uvw + uP_{yz} + vP_{xz} + wP_{xy} \\ \rho uw^2 + uP_{zz} + 2wP_{xz} \end{pmatrix} \tag{A.4}$$

and sources are

$$\mathbf{s} = \begin{pmatrix} 0 \\ r\rho(E_x + vB_x - wB_y) \\ r\rho(E_y + wB_x - uB_z) \\ r\rho(E_x + uB_y - vB_x) \\ 2r\rho uE_x + 2r(B_z\mathcal{P}_{xy} - B_y\mathcal{P}_{xz}) \\ r\rho(uE_y + vE_x) + r(B_z\mathcal{P}_{yy} - B_y\mathcal{P}_{yz} - B_z\mathcal{P}_{xx} + B_x\mathcal{P}_{xz}) \\ r\rho(uE_z + wE_x) + r(B_z\mathcal{P}_{yz} + B_y\mathcal{P}_{xx} - B_y\mathcal{P}_{zz} - B_x\mathcal{P}_{xy}) \\ 2r\rho vE_y + 2r(B_x\mathcal{P}_{yz} - B_z\mathcal{P}_{xy}) \\ r\rho(vE_z + wE_y) + r(B_y\mathcal{P}_{xy} - B_z\mathcal{P}_{xz} + B_x\mathcal{P}_{zz} - B_x\mathcal{P}_{yy}) \\ 2r\rho wE_z + 2r(B_y\mathcal{P}_{xz} - B_x\mathcal{P}_{yz}) \end{pmatrix}. \tag{A.5}$$

Here $r \equiv q/m$ is the charge to mass ratio of the particle and $\rho \equiv mn$ is the mass density. Note that there is one such set of equations for *each* of the s plasma species. These $10s$ equations, coupled to Maxwell equations of electromagnetism, Equations (1.12)–(1.15) are the Ten-Moment plasma equations.